HYDRATE PHASE EQUILIBRIUM DATA OF CO_2 + H_2O + TETRABUTYL AMMONIUM SALTS (CHLORIDE AND FLUORIDE)

Anneline Basdeo

BSc. Chemical Engineering

University of KwaZulu-Natal

This dissertation (ENNO8RPH1) is submitted for the degree of Master of Science in Engineering (MScEng) in the School of Chemical Engineering at the University of Kwa-Zulu Natal.

Supervisor: Prof. Deresh Ramjugernath
Co-supervisors: Dr. Paramespri Naidoo and Prof. Amir H Mohammadi

January 2014

Declaration

I, Anneline Basdeo, declare that:

(i) The research reported in this dissertation, except where otherwise indicated and is my original work.

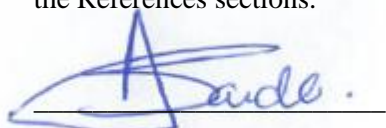(ii) This dissertation has not been submitted for any degree or examination at any university.

(iii) This dissertation does not contain other person's data, pictures, graphs or other information, unless specifically acknowledged as being sourced from other persons.

(iv) This dissertation does not contain other person's writing, unless specifically acknowledged as being sourced from other researchers. Where other written sources have been quoted then:

  a) Their words have been re-written but the general information attributed to them has been referenced;

  b) Where their exact words have been used, their writing has been placed inside quotation marks, and referenced.

(v) Where I have reproduced a publication of which I am an author or co-author I have indicated in detail which part of the publication was actually written by myself alone and have fully referenced such publications:

(vi) This dissertation does not contain text, graphics or tables copied and pasted from the internet, unless specifically acknowledged, and the source are detailed in the dissertation and in the References sections.

_____

A Basdeo (candidate)

As the candidate's supervisor/co-supervisor I agree/ do not agree to the submission of this dissertation.

_____

Prof. D Ramjugernath (supervisor)

_____   _____

Dr. P Naidoo (co-supervisor)   Prof. A.H Mohammadi (co-supervisor)

ABSTRACT

The UNFCC's (United Nations Framework Convention on Climate Change) goal, to stabilize greenhouse gas concentrations through energy technology and prevent anthropogenic interference with the climate system, has led to interest in mitigation strategies such as carbon dioxide capture and storage (CCS). CCS involves the capturing of CO_2, emitted from large industrial sources, before release into the atmosphere and storing it in safe underground rock formations. Gas hydrate or clathrate hydrate crystallization is a promising technology for the capturing of CO_2.

Clathrate hydrates are non-stoichiometric crystalline compounds that consist of a lattice of water molecules that physically encage molecules of another component i.e. CO_2. Clathrate hydrates made of CO_2 gas are formed at high pressures and relatively low temperatures. Previous hydrate phase equilibrium data has been measured for temperature and pressure ranges of (273 - 283) K and (1200 - 4500) kPa. Industrial flue gas exits coal-fired power plants at atmospheric pressure. Hence, the operative costs of compressing such flue gas to the necessary hydrate formation pressure would be significantly high. The pressure at which a clathrate hydrate is formed increases exponentially with temperature. Hence, the lowest possible formation pressure is desired, in order to minimize the flue gas compression costs. High operating pressures can be reduced by use of additives/hydrate promoters which will lower the hydrate formation conditions without affecting the kinetics or the efficiency of CO_2 recovery.

Tetra-n-butyl ammonium chloride (TBAC) and tetra-n-butyl ammonium fluoride (TBAF) are additives that can reduce hydrate formation pressures to feasible industrial conditions, however, there is insufficient phase data available on the systems comprising of (CO_2 + H_2O + TBAC) and (CO_2 + H_2O + TBAF). Due to the current interest in CO_2 capture and storage by gas hydrate crystallization; there is a demand in experimental phase equilibrium data for the relevant CO_2 hydrate systems. In order to design efficient CCS processes, reliable and accurate phase equilibrium data is required.

The present study involved the measurement of hydrate phase equilibrium data for systems CO_2 + H_2O + TBAC and CO_2 + H_2O + TBAF. CO_2 + H_2O + TBAC was measured at a range of (795 -4520) kPa and (281.25- 293.55) K at 4.21 wt%, 10.05 wt% and 30.13 wt% concentrations of TBAC. CO_2 + H_2O + TBAF was measured at a range of (680-2396) kPa and (285.8– 304.3) K at 4.01 wt% and 30.26 wt% concentrations of TBAF. The hydrate phase equilibrium measurements were taken at a maximum pressure of 5 MPa to limit the nominal compression costs and achieve a feasible method to capture CO_2.

The phase equilibria data was measured using an isochoric pressure-search method (isochoric cooling from the vapour-liquid region to the hydrate-vapour-liquid region). Once hydrate formation was confirmed by a sudden drop in pressure (due to gas encapsulation), the system temperature was then increased to dissociate the hydrates. The hydrate-vapour-liquid equilibrium point was recognized as the point of complete decomposition of the hydrate.

A visual high-pressure autoclave, consisting of a 316 stainless steel cylindrical cell ($60cm^3$) and two sapphire windows, was operated to measure the hydrate equilibrium phase data. Pt-100 platinum resistance thermometers and P-10 pressure transducers measured the temperature and pressure conditions respectively during the isochoric pressure-search procedure. The uncertainty of the hydrate equilibrium data point is ±0.3 K and ±1.71 kPa, with a confidence of approximately 95%. This uncertainty consisted of the uncertainty of calibration of the devices, uncertainty of the instruments (specified by the supplier), uncertainty of data repeatability and the uncertainty of the isochoric pressure-search method.

Vapour pressure measurements for carbon dioxide and ethane were performed to verify the pressure and temperature calibrations. The test systems, compromising of CO_2 + H_2O, CO_2 + H_2O + TBAC (4 wt%) and CO_2 + H_2O + TBAF (4 wt%) were measured to validate the accuracy of the experimental apparatus, experimental methodology and ensure the measured hydrate phase equilibrium data were correct and reliable.

An increase in the tetrabutyl ammonium salt concentration resulted in an improved promoting effect of the equilibrium pressure. With reference to a pure CO_2 hydrate, average temperature shifts of approximately 6 K, 9 K and 15 K were noted for 4.21 wt%, 10.05 wt% and 30.13 wt%

concentrations of TBAC. An average temperature increase of 11 K, 16 K and 29 K was observed at 4.01 wt%, 8.27 wt% and 30.26 wt% concentrations of TBAF respectively. A comparison of the effects of TBAC and TBAF validated TBAF to be a stronger promoter for CO_2 hydrate formation.

The hydrate formation rate was observed to have decreased as the hydrate formation region was approached. This phenomenon validated the work of Servio and Englezos(2011), which illustrates that the solubility of CO_2 in water decreases with system temperature, as the system approaches the conditions at which hydrates commence to form. Hydrates formed in the $CO_2 +$ H_2O + TBAC and $CO_2 + H_2O$ + TBAF systems had a slower hydrate formation rate than the $CO_2 + H_2O$ system. Hence, the presence of TBAC and TBAF further reduces CO_2 solubility during hydrate formation.

The modelling approach of Eslamimanesh (2012) was used to model semi-clathrate phase equilibrium conditions of the $CO_2 + H_2O$ + TBAC and $CO_2 + H_2O$ + TBAF systems. The predicted results of the Eslamimanesh (2012) model demonstrated reasonable accuracy at the experimental pressure range. The model was used to predict semi-clathrate phase equilibrium data for each crystal structure of TBAC (i.e. types A, B and C) and TBAF (i.e. types A and B). The predicted results clarified the type of semi-clathrate crystal structure at each experimental condition.

ACKNOWLEDGEMENTS

TABLE OF CONTENTS

LIST OF FIGURES

Chapter 5

Chapter 6

Chapter 7

LIST OF PHOTOGRAPHS

Chapter 5

LIST OF TABLES

Chapter 7

NOMENCLATURE

aa_j, bb_j	Parameters recommended by Munk et al. (1988) for dodecahedral cages	K/MPa
A,B, C	Formation types of either A, B or C semiclathrates	
c, d, e, f, g, i	Adjustable parameters for tetrakaidecahedra and pentakaidecahedra cages	K/MPa
C_j^i	Langmuir constant of cavity i occupied by gas molecule j	
d_m	Density of salt free mixture	kg/m^3
E_m	Dielectric constant of salt-free mixture	
E_N	Dielectric constant of water	
$\hat{f}_i^H$	Fugacity in solution of species i in the hydrate phase	MPa
$\hat{f}_i^L$	Fugacity in solution of species i in the liquid phase at a pressure P	MPa
$\hat{f}_i^V$	Fugacity in solution of species i in the vapour phase at a pressure P	MPa
$f_p{}^L$	Fugacity of the promoter (tetrabutyl ammonium salt)	MPa
$\hat{f}_w^\beta$	Fugacity of water in hypothetical phase β (empty hydrate lattice)	MPa
$\hat{f}_w^H$	Fugacity of water in the hydrate phase	MPa
$\hat{f}_w^L$	Fugacity of water in liquid phase	MPa
H_{g-w}	Henry's constant of gas in water	mol/(L.atm)
I	Ionic strength	mol/m^3
k_i	Binary interaction parameter	J/mol
K	Boltzmann's constant	J/K
m	Molality of aqueous solution	mol/kg
M_m	Molecular weight of salt free solution	kg/mol
M_w	Molecular weight of water	g/mol
N_A	Avogadro's number	mol^{-1}
N_w^β	Number of water molecules in β phase	
P	Equilibrium pressure	MPa

P_c	Critical Pressure	MPa
P^{calc}	Calculated pressure at hydrate dissociation	MPa
P^{exp}	Experimental pressure at hydrate dissociation	MPa
P_p^{sat}	Vapour pressure of promoter	MPa
$P_w^{sat,\beta}$	Vapour pressure of water in empty hydrate lattice	MPa
P_w^{β}	Vapour pressure of the empty hydrate lattice	MPa
$\underline{r}$	Position vector	
r	Distance between guest molecule and water molecule	m
R	Universal gas constant	J/(kg.K)
Rc	Cavity radius	m
T	Equilibrium temperature	K
T_c	Critical temperature	K
v_g^{∞}	Molar volume of gas at infinite dilution	cm³/mol
v_i	Number of hydrate cavities of type i per molecule of water	
V_p^L	Molar volume of hydrate promoter in the aqueous phase	cm³/mol
V_w^{β}	Molar volume of the empty hydrate lattice	cm³/mol
w	Interaction potential between the hydrate cavity and guest molecule	J
w^{gi}	Guest-hydrate interaction energy	J
w^{gg}	Guest-guest interaction energy	J
w_p	Weight fraction of promoter in aqueous solution	
x_i	Mole fraction of component i in the liquid phase at a pressure P	
x_N	Salt-free mole fraction of water	
x_p^L	Mole fraction of the promoter in the aqueous phase	
x_{TBA+}	Moles of TBA⁺cations	mol
x_w	Mass of water	kg
x_w^l	Concentration of water in aqueous phase	mol/m³
z_i	Overall composition of guest i in hydrate phase	
Z	Compressibility factor	

Greek Letters

α_{12}, α_{21}	Adjustable parameter for characteristic of randomness of the mixture	
β	A hypothetical phase representing a metastable empty hydrate lattice	

$\Delta\mu_w^{H\text{-}\beta}$	Difference in chemical potential between water in the hydrate phase and empty lattice	J/mol
$\Delta\mu_w^{L\text{-}\beta}$	Difference in chemical potential between water in the liquid phase and empty lattice	J/mol
γ_i^{EL}	Activity coefficient of the electrolyte solution	
γ_1, γ_2	Activity coefficient of water in the aqueous phase	
γ_w	Activity coefficient of water	
γ_p^L	Activity coefficient of the hydrate promoter in the aqueous phase	
$\mathcal{E}_i$	True liquid mole fraction of component i	
$\mathcal{E}_j$	Mole fraction of salt j	
ρ_p	Density of promoter	
Θ_j^i	Occupancy factor of cavity i by gas molecule j	
Φ_i^{A-P}	Fugacity coefficient of the liquid phase calculated by Aasberg-Peterson et al	
Φ_i^{EOS}	Fugacity coefficient of liquid phasecalculated by an equation of state	
$\hat{\varnothing}_i^L$	Fugacity coefficient in solution of component i in the liquid phase at a pressure P	
$\hat{\varnothing}_i^V$	Fugacity coefficient in solution of component i in the vapour phase at a pressure P	
ω	Accentric factor	
$\underline{\Omega}$	Orientation vector of the guest in the cage	

Superscripts

A-P	Aasberg-Peterson
EL	Electrolyte Solution
EOS	Equation of State
G	Gas
gg	Guest guest
gi	Guest hydrate
H	Hydrate
i	Component
L	Liquid

sat	Saturated
V	Vapour
B	Hypothetical phase

Subscripts

A	Avogadro's number
C	Cavity
i	Component
j	Component
mix	Mixture
p	Promoter in aqueous solution
w	Water

Abbreviations

CCS	Carbon Dioxide Capture and Sequestration
DE	Differential Equation
EOS	Equation of State
H-V-L	Hydrate-Vapour-Liquid
L_w-H-V	Liquid water-Hydrate-Vapour
NRTL	Non Random Two Liquid
OF	Objective Function
TBA^+	Tetrabutyl Ammonium cation
TBAB	Tetrabutyl Ammonium Bromide
TBAC	Tetrabutyl Ammonium Chloride
TBAF	Tetrabutyl Ammonium Fluoride
VLE	Vapour Liquid Equilibrium

CHAPTER ONE

INTRODUCTION

Carbon dioxide (CO_2), in addition to other gases, allows for the transfer of solar radiation through the earth's atmosphere but prohibits the escape of heat. As a result the global surface temperature is increased. Since the Industrial Revolution, the combustion of fossil fuels has led to the release of billions of tons of CO_2 into the atmosphere. According to the International Energy Agency (IEA, 2010), CO_2 emissions in 2050 may rise to twice those of 2007, if no mitigation options are implemented. Since 93% of South Africa's energy generation is derived from coal (Figure 1-1), the future sustainability of energy development in South Africa will require solutions to CO_2 emissions from coal. The concerns of climate change have led to interest in mitigation strategies such as carbon dioxide capture and storage (CCS). Research by the IEA has concluded that in order to stabilize CO_2 concentrations, carbon dioxide capture and storage (CCS) will need to contribute to one-fifth of the total CO_2 reductions by 2050. According to studies by the Clean Air Task Force, innovative technologies in CO_2 capture are necessary in order to meet the growing energy demand while stabilizing CO_2 atmospheric concentrations to safe levels (Fowler, 2008).
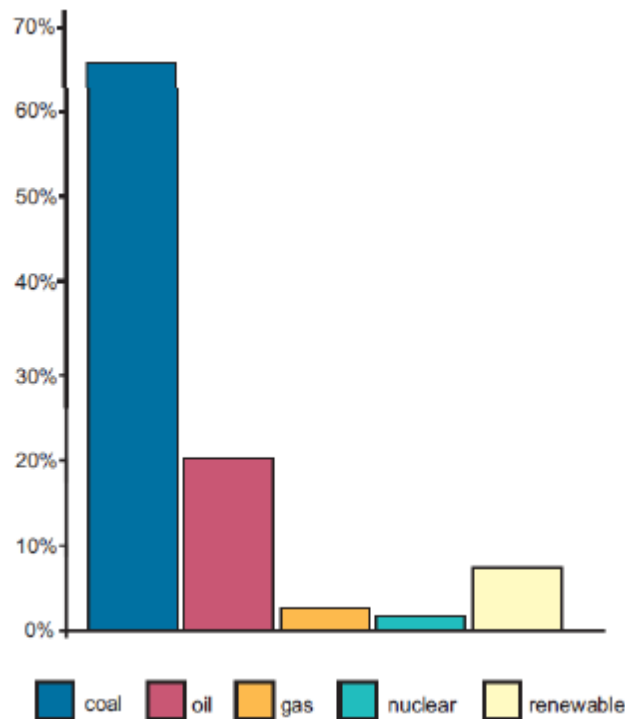
Figure 1-1: Sources of South Africa's electricity generation. (SANERI 2011).

Carbon dioxide capture and storage (CCS) is the process of extracting CO_2 from large sources (such as fossil fuel power stations) and injecting it into porous rock formations deep underground (Linga, 2009). Figure 1-2 illustrates the process of CO_2 capture and storage. CO_2 capture in power stations commonly involves two methods: pre-combustion capture and post-combustion capture.

Pre-combustion capture involves the removal of CO_2 from fossil fuels prior to combustion. The fossil fuel is converted to a gas consisting of predominately H_2 and CO_2, from which CCS processes are applied to separate the gases (Lee et al., 2010a). Post-combustion capture involves the removal of CO_2 from a treated flue gas mixture, consisting of mainly nitrogen (N_2) and CO_2, subsequent to fossil fuel combustion (Linga et al., 2007).

A CCS report by the IPPC (2005) disclosed CO_2 capture and storage to have the potential, when used in combination with other mitigation options, to make critical reductions in greenhouse gas emissions. CCS has the capability to increase the flexibility in achieving greenhouse gas emission reductions and reduce the overall cost of mitigation. Since CCS is currently in commercial use and the process has made net capture efficiencies of 80%-90% in petroleum and petro-chemical industries in the year 2005, CCS is necessary in meeting the United Nations Framework Convention on Climate Change (UNFCCC) goal to stabilize atmospheric greenhouse gas concentrations (IPCC, 2005).
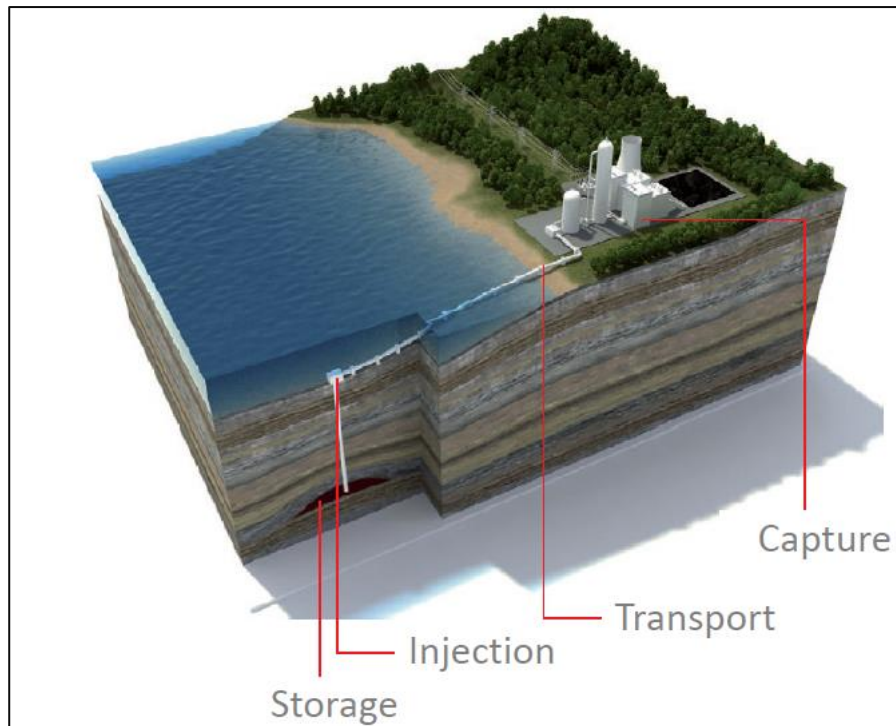
Figure 1-2: Carbon dioxide (CO$_2$) capture and storage (http://www.bellona.org/ccs/, accessed 31 May 2012).

Due to South Africa's coal-based economy, the South African Department of Energy has implemented the research of CCS technologies as a potential tool for CO$_2$ stabilization. The department has aimed to produce a CCS demonstration plant in 2020 and implement the commercial operation of CCS processes in 2025 (Department of Energy, 2011). The South African National Energy Research Institute (SANERI) and the Centre for Carbon Capture and Storage is currently involved in the research of CCS technologies. The project is aimed to capture CO$_2$ from a Sasol plant. The centre for Carbon Capture and Storage has released a carbon storage atlas to identify viable CO$_2$ storage sites once the CCS technologies are commercialised. Such locations include the Karoo and the south Western Cape (SANERI, 2010).

Sasol has recently invested in the CO$_2$ Technology Centre Mongstad (TCM), which aims to demonstrate large scale post-combustion capture. Sasol and the CO2CRC (Cooperative Research Centre for Greenhouse Gas Technologies) have developed a project to investigate the storage of CO$_2$ in gas-depleted reservoirs (Lieberg, 2011). Eskom is currently constructing the Kusile coal-fired power plant in Mpumalanga, where the plant design is aimed to be "CCS

ready". The plant is designed to accommodate future installations of CCS equipment, to capture, transport and permanently store carbon dioxide in a secure location (Bridge, 2011).

Sasol reported that the challenges faced by green-house gas emissions can be successfully overcome through implementing a combination of renewable energy (such as biomass) as well as carbon dioxide capture and storage. CCS forms an integral part of Sasol's long term CO_2 mitigation plans (Lieberg, 2011). A report from the carbon sequestration leadership forum (CSLF) highlighted the need for research and development into a wide-range of innovative CCS technologies in order to lower CCS costs to levels necessary for widespread deployment (CSLF, 2008). New CCS research may be able to improve the efficiency of the current technologies or may enable entirely new approaches. There is persistent interest in the development of cheap, simply and low-energy bearing CCS processes and one of the new methods is through gas hydrate crystallization (Linga et al., 2007).

Gas hydrate crystallization is a promising technology for capturing CO_2. Initially, the research of gas hydrates was purely out of scientific curiosity. In 1934, natural gas hydrates were recognized for plugging natural gas pipelines. This marked the beginning of an intense research effort on the hydrate phase equilibrium data and applications of gas hydrates (Sloan and Koh, 2008).

Gas hydrates are non-stoichiometric crystalline compounds composed of water and gas. The gas molecules (guests) are physically encaged by the lattice of water molecules (host) (Lee et al., 2010a).When gas hydrates are formed from a gas mixture, the hydrate gas composition is different from the gas composition in the original stream. This is due to the hydrate being enriched with one component from the original gas mixture, validating the use of gas hydrate crystallization for CO_2 separation and capture (Lee et al., 2010a).

High pressure conditions are required to produce gas hydrates from CO_2 or N_2. Hence, the operative costs would be significantly high once flue gas (generally close to atmospheric pressure) is compressed in order to satisfy the hydrate formation conditions. The addition of hydrate promoters may lower the hydrate formation conditions without affecting recovery of CO_2, thus alleviating the cost of high pressure conditions.

Tetra-n-butyl ammonium chloride (TBAC) and tetra-n-butyl ammonium fluoride (TBAF) are hydrate promoters that can reduce hydrate formation pressures to feasible industrial conditions, however, there is insufficient phase equilibrium data available on the systems comprising of (CO_2 + H_2O + TBAC) and (CO_2 + H_2O + TBAF) (Li et al., 2010). Due to the current interest in CO_2 capture and storage by gas hydrate crystallization; there is a demand in experimental phase equilibrium data for the relevant CO_2 hydrate systems. In order to design efficient CCS processes, reliable and accurate phase equilibrium data is required. The principle aim of the present study was to investigate the phase behaviour of CO_2 hydrates in the presence of tetra-butyl ammonium salts (TBAC and TBAF). Hydrate phase equilibrium data for the system CO_2 + H_2O + TBAC and CO_2 + H_2O + TBAF were experimentally measured and theoretically modelled at various concentrations of the hydrate promoter. The effect of the promoter concentration on hydrate formation pressures was elucidated in order to establish the role of tetrabutyl ammonium salts as a hydrate promoter.

1.1   Applications of hydrate crystallization

A potential energy source

Several studies show natural gas hydrates as a possible energy source for the future (Oellrich et al., 2004). Such studies centre on methane hydrates, found in sea-floor sediments and artic permafrost, and the energy potential they possess. Although burning the natural gas may liberate CO_2, the amount of CO_2 emitted per unit of energy produced is 60% less than that liberated from burning coal (Congressional research service, 2010). The United States and other countries with territory in the Artic are interested in developing gas hydrates as an energy resource. Current research involves methods of harvesting the methane hydrates through depressurization and thermal simulation. Countries currently involved in national research and development programs into implementing hydrate technology include Japan, India and China (Congressional research service, 2010).

Hydrate separation technology

There are two reasons to validate the use of gas hydrate crystallization as a separation method:

1. Gas hydrate crystals contain only water and their respective hydrate-forming gas.
2. The composition of the hydrate-forming substances in hydrate crystal is of a different composition to that in the original gas stream.

Hence one can separate a gas mixture from an aqueous solution by:

1. Forming a gas hydrate crystal.
2. Separating the hydrate crystal from the concentrate solution.
3. Decomposing the hydrate into water and the concentrated gas.

Gas hydrates may be formed at various conditions that may result in the desired fractionation

Desalination

The use of gas hydrate technology as a possible desalination technology has been investigated by a number of groups with significant efforts starting in the 1940's (Eslamimanesh, 2012). When gas hydrates form, the chemical structure excludes solids and other impurities. Gas hydrate-based technology involves three stages:

1. The creation/formation of the gas hydrate.

2. Washing of the hydrate.

3. Dissociation of the hydrate into gas and water molecules. Hence three process streams are produced: brine, gas and purified water.

Hydrate desalination technology proves advantageous to conventional methods due to its lower energy requirements and use of low cost materials (Petticrew, 2011). Javanmardi and Moshfeghian (2003) estimated the required energy and cost of a hydrate-based desalination process. The research concluded that the proposed process is not economically feasible, due to the high pressure operating conditions. However with the use of a hydrate promoter, the economic costs can be lowered considerably.

Oil and gas industry

Gas hydrates may form from liquid or light hydrocarbons in oil/gas reservoirs, which may result in complexities in oil/gas production due to blockages in pipelines and process facilities (Englezos, 2004). However there are several studies that propose the use of gas hydrate technology to separate oil and gas in reservoir fluids and reduce the usage of convectional oil/gas separators. Dorsett (1989) and Ostergaard et al. (2000) proposed a novel approach to the separation of oil and gas via gas hydrate crystallization. These studies involved the identification of major parameters, construction of an appropriate mass transfer model and simulation of a pilot process.

Carbon dioxide (CO_2) separation

CO_2 separation from flue gas (primarily $CO_2 + N_2$) is the most expensive step in CO_2 capture and sequestration. Hence there is a need for a more energy efficient and environmental friendly CO_2 separation technology (Belandria et al. 2011). Due to the difference in chemical affinity between CO_2 and N_2, hydrate separation will result in a CO_2-rich hydrate phase and a N_2-rich gas phase. The CO_2 hydrate can be decomposed by depressurization or heating and CO_2 can be recovered as a separated gas. High pressure operating conditions are an expensive limitation to CO_2 hydrate separation technology (Duc et al., 2007). Such a limitation may be overcome by the use of hydrate promoters to decrease hydrate formation pressures and increase formation temperatures. However phase equilibrium data of CO_2 systems with environmentally friendly promoters is scarce. Section 1.2 further discusses carbon dioxide separation via gas hydrate technology.

1.2 CO_2 capture via gas hydrate crystallization

CCS involves the capturing of CO_2, emitted from large industrial sources, before its release into the atmosphere and pumping it into stable rock formations underground (Linga, 2009). There are primarily two common methods for capturing CO_2 from point-sources such as power stations: pre-combustion capture and post-combustion capture.

In pre-combustion capture fossil fuel is gasified by heating it in small amounts of oxygen, producing a synthesis gas or 'syngas'. The key components of syngas are carbon monoxide and hydrogen. The carbon monoxide is than reacted with steam to form CO_2 and additional hydrogen (Lee et al., 2010a). The CO_2 is captured and the remaining hydrogen is used as 'clean fuel' in the power plant. It is only possible for Integrated Gasification Combined Cycle (IGCC) plants to apply pre-combustion capture of CO_2. However, only a few such plants exist as it is not yet a well-established technology.

Post-combustion capture involves the separation of CO_2 from the combustion products ($CO_2 + N_2$) before their release into the atmosphere. The CO_2 molar content of the combustion products is approximately 15-20% (Linga et al., 2007).

Post-combustion capture is far advantageous in comparison to pre-combustion capture for the following reasons (Linga, 2009):

- It may be easily incorporated and retrofitted into existing coal-fired power plants without requiring significant change in current coal combustion technology.
- It offers flexibility by allowing the power plant to operate independently to the capture process.
- Pre-combustion capture requires operation IGCC plants only. The commercialization of IGCC to provide coal-fired electricity is slow and not well established.

For the reasons discussed above, this research focuses on gas hydrate crystallization for the separation of CO_2 as a post-combustion capture technology. There are two major alternatives to the investigated separation technology (gas hydrates crystallization): Chemical Absorption and Adsorption. The advantages and disadvantages of such post-combustion capture processes are discussed in Table 1-1.

Table 1-1: Benefits and drawbacks of commonly-used post-combustion capture processes (Belandria, 2012).

CO$_2$ Separation Method	Advantages	Disadvantages
Absorption (chemical solvents)	Well established process. Solvent can be recycled. Can be simply integrated into existing power-plants	High regeneration costs. Existing impurities and by-products may lead to the degradation of the solvent. Solvent can form corrosive solutions with flue gases. Low CO$_2$ loading capacity.
Adsorption (solid sorbents)	Sorbent may be re-used. Commercially available.	Sorbent susceptible to degradation. Adsorption time is not practical. Low degree of CO$_2$ separation. Poor selectivity of sorbents to CO$_2$. Operating costs are higher than absorption process.

Although literature presents solvent absorption as a promising process for CO$_2$ recovery, the regeneration of the solvent makes the absorption process energy intensive (Linga et al. 2008). Chemical absorption and adsorption have proven to be successful in post-combustion capture but still remain with critical problems. The need to reduce cost, process time and energy motivates further research into post-combustion capture. Gas-hydrate crystallization is a new and innovative concept for the post-combustion capture of CO$_2$. The advantages of utilizing gas hydrate crystallization for the separation and capture of CO$_2$ from flue gas include:

- Water is the main substance required to form a CO_2 hydrate crystal. Hence the technology requires a cheap, abundant and green raw material.
- The addition of a hydrate promoter (such as TBAC) can reduce hydrate equilibrium pressures thereby reducing process energy requirements.
- Large amounts of CO_2 hydrates can be transported in slurries from the separation process to underground storage via pipelines or pressurized and chilled vessels.
- The captured CO_2 may not be limited to sequestration but may be utilized in industrial processes (Sabil, 2009).

CCS research has shown that gas hydrate crystallization can be used in power stations to capture CO_2 in the pre-combustion of fuel as well as from the flue gases (post-combustion).When gas hydrates are formed from a gas mixture, the hydrate gas composition is different from the gas composition in the original stream. This is due to the hydrate being enriched with one component from the original gas mixture, validating the use of gas hydrate crystallization for CO_2 separation and capture (Lee et al., 2010).

CO_2 capture via gas hydrate crystallization involves the use of van der Waals interactions between water molecules to form a hydrate cage and encapsulate gas molecules. CO_2 gas is dissolved in liquid water at typically low temperatures and high pressures to form hydrates encaging CO_2 gas. Industrial flue gas consists of primarily $CO_2 + N_2$, however the hydrate-vapour-liquid phase equilibrium conditions of CO_2 are considerably lower as compared to N_2 (Figure 1-3). Based on the significant difference in the equilibrium conditions required to form a CO_2 hydrate as compared to a N_2 hydrate, it is expected for CO_2 to enter the hydrate phase and separate from N_2.
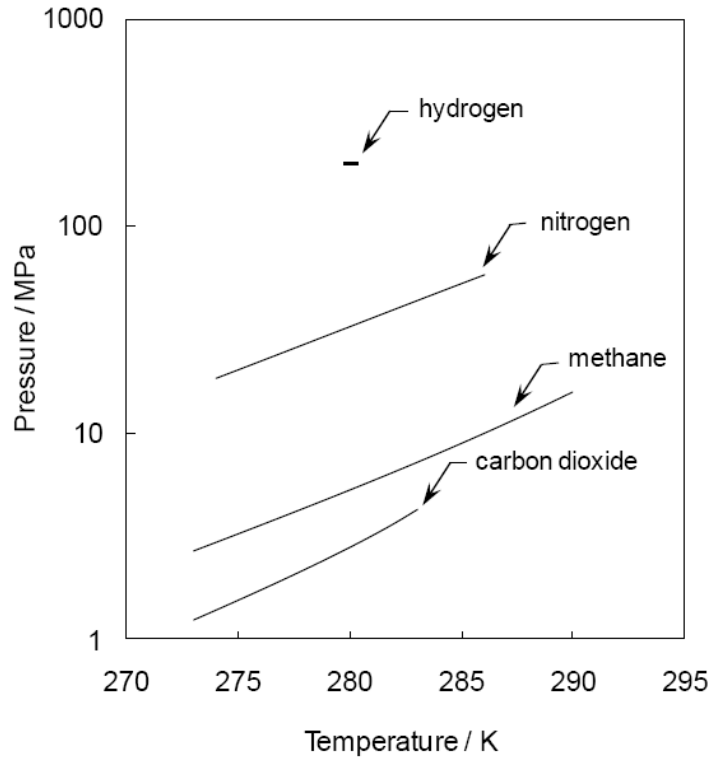
Figure 1-3: Carbon dioxide hydrate phase equilibrium conditions as compares to nitrogen, methane and hydrogen. The carbon dioxide, nitrogen and methane hydrate data has been predicted by HWHYD model (HWHYD, 2000). The hydrogen hydrate equilibrium data was reported by Mao and Mao (2004).

Research into CO_2 capture via gas hydrate crystallization is not considerably extensive however there is evidence of a noticeable progress of such studies. Table 1-2 provides a summary of previous CO_2 capture research via gas hydrate crystallization. Linga et al. (2007) developed a three-stage hybrid process for both pre-combustion and post-combustion capture of CO_2. The process involved a two-stage gas hydrate process, followed by a membrane separation. The design implemented a CO_2 recycle stream from the membrane process to the second-stage gas hydrate process to increase the final purity of CO_2 gas. The main disadvantage of the above process is the high operating pressures of gas hydrate process, especially in the first-stage of gas hydrate separation. Linga et al. (2007) suggested the use of an additive to reduce hydrate forming conditions.

Table 1-2: Previous experimental studies on post and pre-combustion capture of CO₂ via gas hydrate.

Author	CCS process	Research
Duc et al. (2007)	Post-combustion	Designed a 6-stage hydrate process for the post-combustion capture of CO_2.
Linga et al. (2007)	Post and Pre-combustion	Developed a hybrid process based on gas hydrate crystallization and membrane separation. This was designed for both the post and pre-combustion capture of CO_2.
Linga et al. (2008)	Post and Pre-combustion	Developed a large scale apparatus that can operate at different gas/water contact modes.
Fan et al. (2009)	Post-combustion	Measured phase equilibria data for up to 7.31 MPa.
Bouchema et al. (2009)	Post-combustion	Developed a computer programme (GasHyDyn) to predict thermodynamic equilibrium conditions of $CO_2 + N_2$ hydrates.
Belandria et al. (2011a)	Post-combustion	Measured phase equilibria data for pressures up to 17.68 MPa.
Belandria et al. (2011b)	Pre-combustion	Measured phase equilibria data for pressures up to 9 MPa.
Herri et al. (2011)	Post-combustion	Measured phase equilibria data for pressures up to 10.57 MPa.

CHAPTER TWO

LITERATURE REVIEW

2.1   Clathrates and Semi-clathrate Hydrates

Clathrate hydrates or gas hydrates were discovered in 1810 by Sir Humphrey Davy, who observed that a dissolved chlorine gas in water freezes at a faster rate than pure water (Sloan and Koh, 2008). Common natural gas hydrates include methane, ethane and carbon dioxide.

Clathrates are types of inclusion compounds which consist of generally two molecular species that arrange themselves in such a manner that one of the species (host) physically encapsulates the other (guest). Inclusion compounds are classified based on the geometrical arrangement between host and guest molecules. This consists of three arrangements (cage, canal and layer). Clathrates are inclusion compounds where the host molecule entraps the guest molecules in a cage-like structure. Clathrates that contain water molecules as the host species are termed clathrate hydrates or gas hydrates (Englezos, 1993).

Gas hydrates are non-stiochiometric crystalline compounds that are formed under low temperatures and generally high pressures. The cage-like structure of water is formed through hydrogen bonding. The hydrogen bond causes the water molecules to align in regular orientations. The presence of gas molecules or volatile liquids allows the aligned molecules to stabilize, resulting in a solid structure. The water molecules are the host molecules and the gas molecules or volatile liquids are referred to as the guest molecules. It is assumed that the stabilization of the guest molecule is due to van der Waals forces; however no bond is formed between the guest molecule and host molecule (Carroll, 2003).
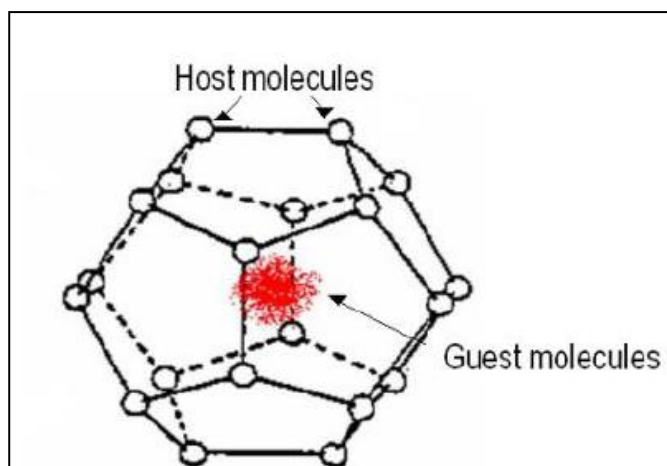
Figure 2-1: Water molecules (host) enclosing gas molecules (guest) in a cage-like structure to form a simple gas hydrate structure (Englezos, 1993)

The significant findings in gas hydrates can be classified into three landmark phases. The first period exists between discovery of gas hydrates in 1810 until 1934. This period includes the gas hydrates as a scientific interest in which gas, dissolved in water, was transformed into a solid. The second period exists from 1934 until 1960. In 1934, Hammerschmidt determined that gas hydrates were blocking natural gas pipelines which lead to the interest in hydrate inhibitors (such as methanol) to hinder the formation of natural gas hydrates in transportation lines. The third period exists between the mid-1960's until the present. This period includes the research into the existence of hydrates in deep oceans, permafrost regions and extra-terrestrial environments such as Mars.

Comprehensive research into gas-forming hydrates later followed with the discovery of salt-forming hydrates. In the 1940's, Fowler et al. (1940) discovered that tetra-alkyl ammonium salts could form hydrates. Further investigations by Feil et al. (1961) and Beurskens et al. (1963) revealed that the structures of these hydrates were similar to gas hydrates however, the charged centres of the cation and anion replaced water molecules at some lattice sites and the alkyl chains occupied larger cages of the structures. The breaking of the water lattice by salt ions lead to the term "semi-clathrate hydrates" or "semi-clathrates" (Hughes and Marsh, 2011).Semi-clathrates contain halide ions which displace the water molecules in the hydrate cage-like framework, forming hydrogen bonds together with the water molecules which entrap the guest molecule (Li et al., 2010b). Semi-clathrates share similar physical and structural properties to true gas hydrates.

2.2   Hydrate Structure

The hydrate consists of hydrogen-bonded water molecules that form a cage-like structure containing cavities. The diameter of these cavities range from 780 to 920 pm (picometre) in size (Englezos, 1993).

Literature states that hydrates can exist typically in three distinct structures: Structure I, Structure II and Structure H. Structure I and structure II are different-sized cubic shapes whilst structure H is hexagonal shaped (Sloan et al., 2008).

Structure I consists of two types of cavities:

    a) A cavity with 12 pentagonal faces called a pentagonal dodecahedron (5^{12}).

    b) A larger cavity with 12 pentagonal and 2 hexagonal faces ($5^{12}6^{2}$) called a tetrakaidecahedron.

Structure II consists of two types of cavities:

    a) A cavity with 12 pentagonal faces called a pentagonal dodecahedron (5^{12}).

    b) A larger cavity with 12 pentagonal and 4 hexagonal faces ($5^{12}6^{4}$) called a hexakaidecahedron.

Structure H consists of three types of cavities:

    a) A cavity with 12 pentagonal faces called a pentagonal dodecahedron (5^{12}).

    b) A cavity with 3 square, 6 pentagonal and 3 hexagonal faces ($4^{3}5^{6}6^{3}$).

    c) A larger cavity with 12 pentagonal and 8 hexagonal faces ($5^{12}6^{8}$).

Figures 2-2 and 2-3 below, demonstrates the shapes of all hydrate cavities. According to Sloan et al. (2008), CO_2 plays a guest molecule to hydrate structure I. Common guest molecules to structure II hydrates include N_2, O_2 and H_2. Methyl butane and polymethylbutanes are guest molecules to structure H.
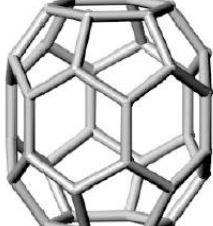
	Small	Medium	Large
Structure I	5^{12}		$5^{12}6^2$
Structure II	5^{12}		$5^{12}6^4$
Structure H	5^{12}	$4^3 5^6 6^3$	$5^{12}6^8$

Figure 2-2: Hydrate structures I, II and H are composed of the polyhedral cavities shown above (Sloan et al., 2008). The cavity with 12 pentagonal faces is common to all three structures.
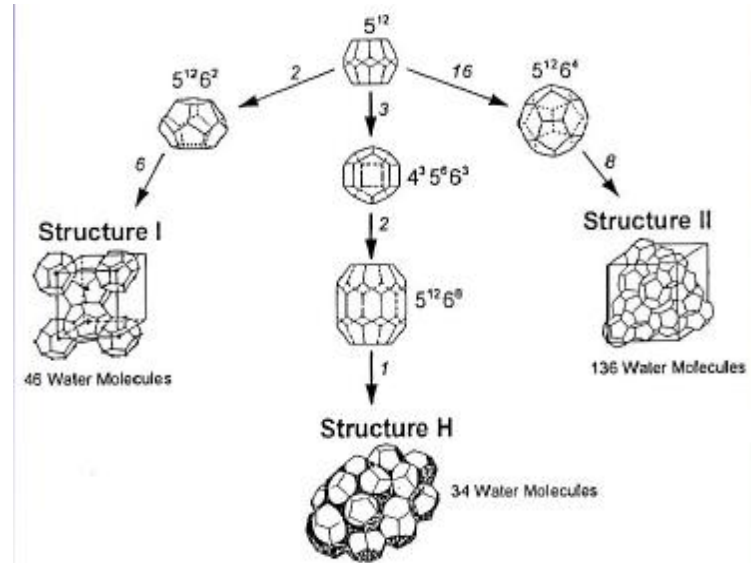
Figure 2.3: Polyhedral cavities that lead to the formation of Structure I, II and H. Structure I consists of 2 5^{12} cavities and 6 $5^{12}6^{2}$ cavities. Structure II consists of 16 5^{12} cavities and 8 $5^{12}6^{4}$ cavities. Structure H consists of 3 5^{12} cavities, 2 $4^{3}5^{6}6^{3}$ cavities and 1 $5^{12}6^{8}$ (Sloan, 2003)

2.3   Phase Diagrams

Phase diagrams are imperative in order to understand the pressure, temperature and composition bounds of hydrate formation. A brief description of hydrate phase diagrams for a single-component and two-component system is provided to gain fundamental insight into hydrate phase equilibrium.

Gas hydrate crystallization is a physical process; whereby no chemical reaction is observed for all species involved (Beltran, 2012). If no reactions occur, the Gibbs phase rule is given by:

$$F = 2 + N - \pi \qquad (2.1)$$

F - degree of freedom

N - number of components

π - number of phases

The degree of freedom of a system (F) is the number of intensive variables (non-dependent of the size of the system) that must be specified for a system in equilibrium before the remaining intensive variables can be calculated.

The observation of the unary system of H_2O is important for the interpretation of clathrate hydrate phase behaviour since H_2O is always present in hydrate systems. Three phases that can occur in a unary system of H_2O include:

1. Ice (I)
2. Liquid water (L_w)
3. Water Vapour (V)

Table 2-1 provides an overview of examples of applying Gibb's phase rule to the unary system of H_2O. The equilibrium curves of I-V, I-L_w and L_w-V intersect at the triple point I-L_w-V, where the three phases of H_2O stably coexist. Figure 2-1 provides a schematic diagram of the triple point of a H_2O unary system.

Table 2-1: Application of Gibbs phase rule to the unary system of H_2O (Heuvel, 2004).

π	N	F	Phase	Representation on P-T plane
1	1	2	L_w	region, surface
2	1	1	I-L_w	curve
3	1	0	I-L_w-V	point
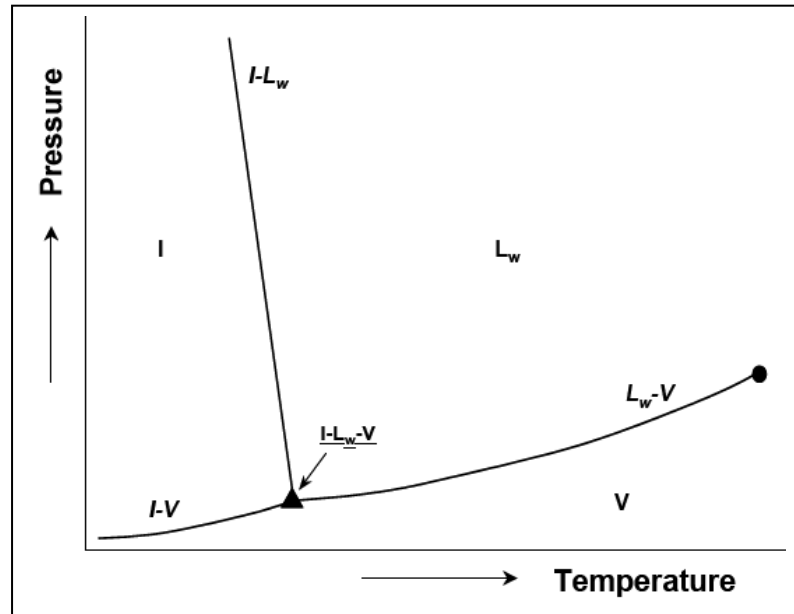
Figure 2-4: Typical phase diagram of pure water (H₂O) (Heuvel, 2004).

In a binary hydrate system, the number of coexisting phases increases. Such phases include:

1. Ice (I)
2. Liquid water (L_w)
3. Hydrate phase (H)
4. Liquefied gas (L_g)
5. Vapour (V)

It is generally assumed that the vapour phase of a gas hydrate system predominantly consists of the hydrate-forming gas and any water vapour present is at a negligible amount. The liquid phase composition will depend on the solubility between the hydrate-forming gas and water. In certain regions of pressure, temperature or overall composition, immiscibility between L_w and L_g may occur (Heuvel, 2004). Table 2-2 provides an overview of examples of applying Gibb's phase rule to a binary hydrate system.

Table 2-2: Application of Gibbs phase rule to the binary system of H_2O (Heuvel, 2004).

π	N	F	Phase	Representation on P-T plane
2	2	2	L_w + V or H + L or H + I	region, surface
3	2	1	H - L_w - V or H - L_w-L_g or H - I -V or H - I - L_w or H - V-L_g or I - L_w - V	curve
3	2	0	H – I - L_w - V or H - L_w - L_g - V	point

In a pure water (H_2O) unary system, three two-phase curves intersect to form a triple point. In a hydrate binary system consisting of H_2O and a single hydrate-forming gas, four three phase curves intersect to form a quadruple point, where the four phases stably coexist. There are two such quadruple points i.e H – I - L_w - V and H - L_w - L_g - V. Figure 2-5 provides a schematic representation of a phase diagram for a binary system and the resulting quadruple points. The H - V - L_w equilibrium line is the most conventionally measured phase and exists between Q_1 and Q_2.
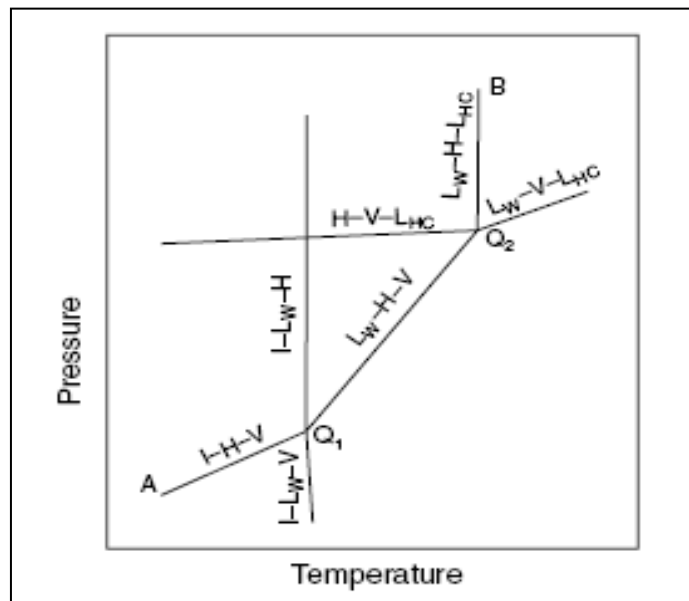
Figure 2-5: Typical phase diagram of a hydrocarbon (HC) and water (H_2O) (Sloan and Koh, 2008). Q_1 and Q_2 are the lower and upper quadruple points respectively.

2.4 The use of additives as thermodynamic promoters

Industrial flue gas exits coal-fired power plants at atmospheric pressure. Hence the operative costs of compressing such flue gas to the necessary hydrate formation pressure would be significantly high. Since the hydrate formation pressure increases with temperature the lowest possible pressure is desired, to minimize compression costs. High operating pressures can be reduced by use of additives/hydrate promoters that will lower the hydrate formation conditions without affecting the efficiency of CO_2 recovery.

The selection of an appropriate hydrate promoter is dependent on the corresponding field of application. Intermediate sized hydrocarbons such as cyclopentane, benzene and cyclohexane have been identified to be successful hydrate promoters. Such intermediate sized hydrocarbons are known as heavy hydrate formers (HHF). HHF's are known to have a low solubility in water and may be considered to promote hydrates in processes that require a clean water phase such as water desalination (SECOHYA, 2007).

Water-soluble hydrate promoters are desirable for oil and gas separation applications, since the promoters help to boost the conversion of gas into hydrates at low formation pressures. Various organic compounds belong to the group of water-soluble hydrate promoters. Examples of such promoters include acetone and tetrahydrofuran (THF). Table 2-3 provides a summary of all experimental studies which utilise promoters to lower gas hydrate formation pressures. Several investigations have highlighted THF as a promising additive to reduce CO_2 hydrate formation pressures and time. Linga et al. (2008) presented a medium pressure gas hydrate formation process for pre-combustion CO_2 capture with the use of THF as a hydrate promoter. Liu et al. (2008) observed that a mixture of THF and sodium dodecyl sulphate (SDS) can promote the CO_2 hydrate formation rate considerably. Research by Lee et al. (2010a) concluded that THF can reduce the hydrate-forming pressure and time of CO_2 hydrates significantly.

However separation processes involving a THF promoter requires significantly low temperatures (0.6°C) (Li et al., 2009). Once the gas hydrate is heated and decomposed, the guest component (CO_2) will be released. THF is volatile and may be released with CO_2 upon decomposition (Tohidi, 2006). THF is a possible human carcinogen and is highly flammable;

hence further separation will be required to produce a clean CO_2 stream. Acetone and sodium dodecyl (SDS) have been studied extensively as successful gas hydrate promoters, however these promoters are expensive, toxic and volatile raw materials (Mo et al., 2004; Liu et al., 2008; Lang et al., 2010; Changyu et al., 2011).

An effective promoter is required to be non-volatile, non-toxic and environmentally friendly whilst improving hydrate formation conditions. Tetra-n-butyl ammonium salts are non-volatile, environmentally friendly compounds that combine with water to form semi-clathrates (Fan et al, 2009). Semi-clathrates can be applied to gas storage and separation processes since it allows for the storage of small gas molecules within its empty cages at temperatures and pressures relatively close to atmospheric. (Lee et al., 2010b).

Semi-clathrate hydrates formed from tetra-n-butyl ammonium salts (i.e. TBAC and TBAF) are stable under atmospheric pressure and room temperature. Three crystal structures of TBAC have been reported: TBAC.24H_2O, TBAC.30H_2O and TBAC.32H_2O. The equilibrium temperature of such hydrates at atmospheric pressure is (288.2, 288.3 and 287.95) K respectively (Makino et al., 2010). TBAF semi-clathrates form two crystal structures: TBAF.28.6H_2O and TBAF.32.2H_2O. Pure CO_2 hydrate equilibrium occurs at pressures distinguishably higher than atmospheric and temperatures below ice point. Considering the significantly mild equilibrium conditions (pressure and temperature conditions close atmospheric) of TBAC semi-clathrates, tetra-n-butyl ammonium salts have the capability to encapsulate CO_2 gas molecules and form semi-clathrates at significantly lower pressures and higher temperatures than pure CO_2 hydrates, hence validating the use of semi-clathrate formation as an economical CCS process.

As described at the beginning of Chapter 2, gas hydrates generated from tetrabutyl ammonium salt solution are known as semi-clathrates. Tetrabutyl ammonium semi-clathrates consist of halide anions that are bounded to water molecules through hydrogen bonds and attach to the host framework. Figure 2-6 provides a schematic diagram of a tetrabutyl ammonium bromide hydrate. In contrast to conventional gas hydrates, the tetrabutyl ammonium salt both physically bonds with the water structure in addition to occupying the larger cavities. However tetrabutyl ammonium semi-clathrates are capable of trapping considerable volumes of gas in the small available cavities but at substantially lower pressures than gas hydrates (Maniko et al. 2010).

The small available cavities provide the appropriate size for entrapping small gas molecules such as CO_2.
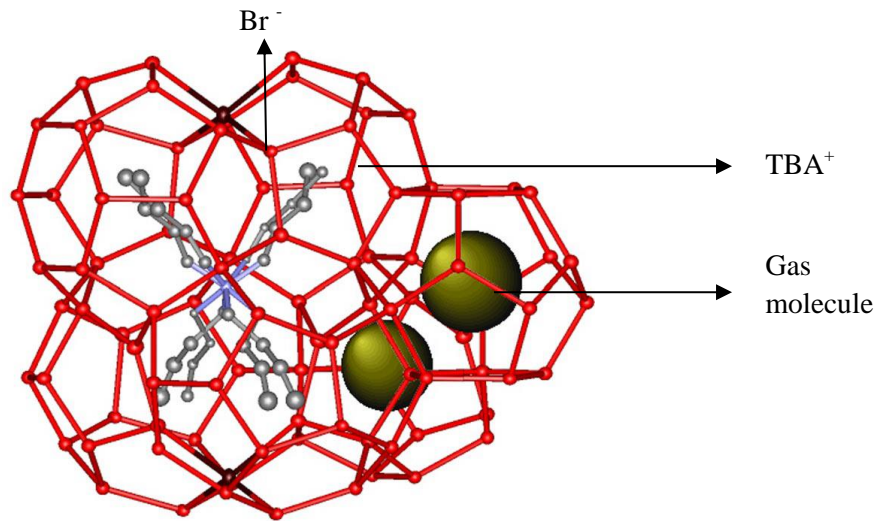
Figure 2-6: Structure of tetrabutyl ammonium bromide (TBAB) semi-clathrate hydrate. The tetrabutyl ammonium cation (TBA$^+$) is located within the large hydrate cavities and bromide anions (Br$^-$) form part of the hydrate cage (Shimada et al. 2005).

Li et al. (2010) measured phase equilibrium data of CO_2 in the presence of tetra-n-butyl ammonium (chloride and fluoride) for a pressure range of 0.4-0.37 MPa. The hydrate phase equilibrium data of $CO_2 + TBAC + H_2O$ and $CO_2 + TBAF + H_2O$ were lower than that of $CO_2 + H_2O$ at the same temperature (Refer to Figure 2-8 and Figure 2-9).
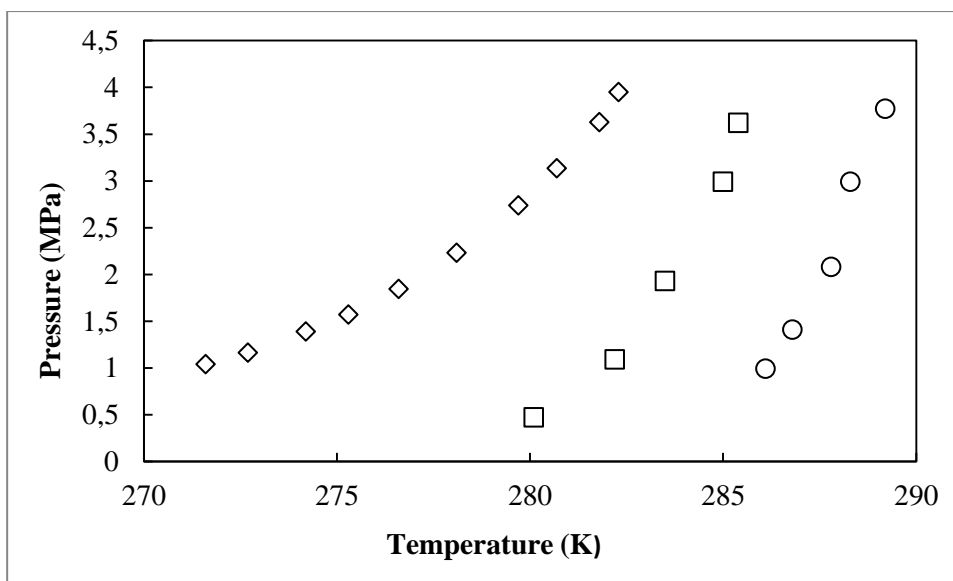
Figure 2-7: Phase equilibrium conditions for the CO_2 + H_2O + TBAC systems. ◇ , 0 wt% TBAC; □, 4.34 wt% TBAC; ○, 8.75 wt% TBAC (Li et al., 2010).
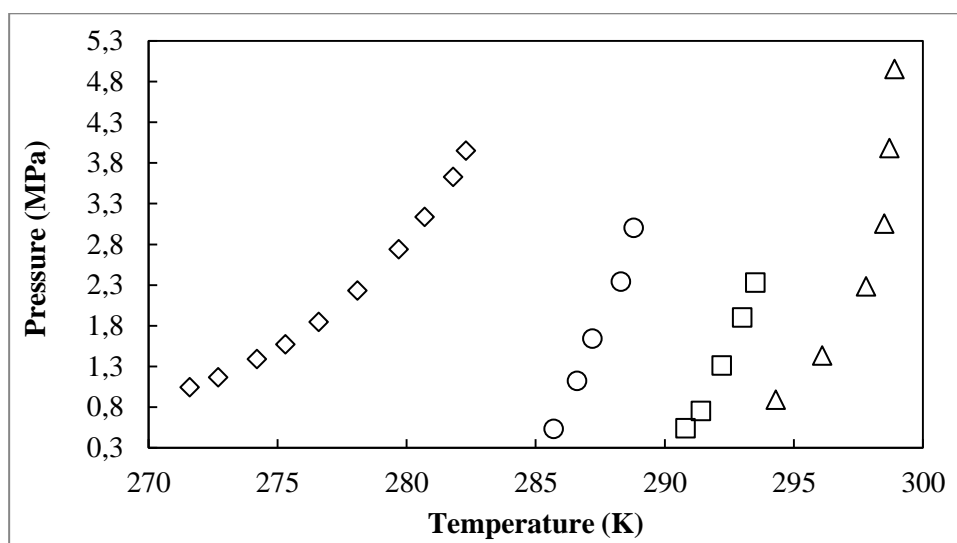
Figure 2-8: Phase equilibrium conditions for the CO_2 + H_2O +TBAF systems. ◇ 0 wt% TBAF; ○, 5 wt% TBAF, Li et al. (2010); □, 10 wt% TBAF, Li et al. (2010); △, 15 wt% TBAF, Mohammadi et al. (2013).

Table 2-3: Previous experimental studies illustrating the effects of promoters on hydrate formation. **Previous promoters include tetrabutylammonium fluoride and bromide (TBAF and TBAB), sodium dodecyl sulphate (SDS) and tetrahydrofuran (THF).**

Author	Additive(s)	Research
Mo et al. (2004)	Acetone	Increased the gas hydrate storage ability of various gas hydrates with acetone.
Tohidi et al. (2006)	TBAB	Reduced hydrate formation pressures of hydrogen hydrates with use of TBAB solutions.
Duc et al. (2007)	TBAB	Reduced the formation pressures of simple hydrates (CO_2 or N_2) and mixed hydrates ($CO_2 + N_2$)
Chapoy et al. (2007)	TBAB, TBAF	Measured phase equilibria data of $TBAF + H_2 + H_2O$ and $TBAB + H_2 + H_2O$ at pressure up to 100MPa.
Linga et al. (2008)	THF	Designed a medium pressure hydrate process for the pre-combustion capture of CO_2 with the addition of small amounts of THF.
Lin et al. (2008)	TBAB	Reduced the formation pressure of CO_2 hydrates by 74% and 87% at 283 K and 279 K respectively.
Liu et al. (2008)	THF, SDS	Promoted the hydrate formation rate of CO_2 hydrates considerably by the addition of a mixture of THF and SDS.
Fan et al. (2009)	TBAB, TBAF	Demonstrated that TBAF can accelerate hydrate formation faster than TBAB.
Li et al. (2009)	TBAB	Shortened induction time as well as reduced formation pressure of $CO_2 + N_2$ hydrates with the addition of 5 wt% TBAB.
Lee et al. (2010)	TBAB	Shortened induction time as well as reduced formation pressure of $CO_2 + N_2$ hydrates within the addition of 5 wt% TBAB.
Maekawa et al. (2011)	Acetone	Measured phase equilibria data of acetone $+ CO_2 + H_2O$ at pressure up to 3.98 MPa.
Gholinezhad et al. (2011)	TBAB	Captured CO_2 from $CO_2 + H_2$ gas mixture via gas hydrate crystallization with the addition of 5 wt% TBAB. The hydrate equilibrium pressures were reduced significantly as compared to a non-additive system. The addition of TBAB did not compromise the CO_2 recovery.

Mohammadi et al. (2013)	TBAF	Measured phase equilibria data of $CO_2 + H_2O + TBAF$, methane $+ H_2O + TBAF$ and $N_2 + H_2O + TBAF$ for (2-15) wt% TBAF.
Xu and Lang (2014)	Tert-butylamine	Measured phase equilibria data of $CO_2 + H_2O +$ tert-butylamine and $N_2 + H_2O +$ tertbutylamine for a pressure range of (2.27-13.70) MPa.
Chen et al. (2014)	TBAB	Demonstrated that TBAB decreased hydrate formation pressures of SO_2 hydrates and helps the dissolution of SO_2 in the aqueous solution.
Lin et al. (2013)	TBAB	Experimental and modelling study on the CO_2 solubility in TBAB solution and the density of CO_2-saturated TBAB solution, for purpose of hydrate-based thermodynamic data.

Fan et al. (2009) captured CO_2 from a simulated flue gas consisting of CO_2 (0.166 mole fraction) + N_2 via semi-clathrate hydrates. The additives used to create the semi-clathrate structure were TBAB and TBAF. The calculated hydrate formation rate constant of TBAB was five times larger in magnitude than that of TBAF at constant feed pressure, resulting in TBAF being a much more effective hydrate promoter than TBAC.

Lin et al. (2008) investigated the effects of tetra-n-butyl ammonium bromide (TBAB) concentrations on the hydrate-forming pressure of CO_2 hydrates. It was concluded that the addition of TBAB can reduce hydrate-forming pressures by 80%. Li et al. (2010) investigated the effects of tetra-*n*-butyl ammonium halides (bromide, chloride and fluoride) on CO_2 hydrate formation and concluded that tetra-*n*-butyl ammonium fluoride (TBAF) produced the lowest CO_2 hydrate equilibrium pressure. Gholinezhad et al. (2011) successfully captured CO_2 via gas hydrate crystallization and proclaimed TBAF to be a suitable additive to improve the operating conditions significantly.

Table 2-4 provides a summary of all experimental studies on CO_2 semi-clathrates. Previous research has proven TBAB to an effective promoter of CO_2 hydrate crystallization; however (as described in Table 2-4) tetra-n-butyl ammonium fluoride (TBAF) and tetra-n-butyl ammonium chloride (TBAC) have not been studied extensively.

Table 2-4 Phase equilibria data on CO_2 semi-clathrates.

Author	System	Additive and Concentration (wt %)	P Range (kPa)	T Range (K)	No. of Data Points
Duc et al. (2007)	CO_2	TBAB: 5, 10, 40, 65	273 - 3320	279.30-290.90	4
Lin et al. (2008)	CO_2	TBAB: 4.43, 7.02, 9.01	344 - 2274	279.40 - 288.09	7
Li et al. (2010)	CO_2	TBAB: 5,10	400 - 3420	280.20 - 288.8	6
Li et al. (2010)	CO_2	TBAC: 4.34 – 8.72	470- 3620	280.10 - 289.2	6
Li et al. (2010)	CO_2	TBAF: 4.08 – 8.26	530– 3000	285.70 - 293.50	6
Meysel et al. (2011)	CO_2 (0.75 mole fraction) + N_2	TBAB: 0.05, 0.1, 0.2	1964 - 3761	284.05 - 290.02	4
Meysel et al. (2011)	CO_2 (0.5 mole fraction) + N_2	TBAB: 0.05, 0.1, 0.2	1965 - 5728	282.27 - 290.39	4
Meysel et al. (2011)	CO_2 (0.2 mole fraction) + N_2	TBAB: 0.05, 0.1, 0.2	2976- 5901	281.75 - 288.88	4
Mohammadi et al. (2012)	CO_2 (0.151 mole fraction) + N_2	TBAB: 5, 15, 30	1570 - 1621	277.10– 293.2	4
Mohammadi et al. (2012)	CO_2 (0.399 mole fraction) + N_2	TBAB: 5, 15, 30	1120 –6170	277.10 – 290.6	4
Mohammadi et al. (2013)	CO_2	TBAF: 2, 5, 15	890-4980	287.8-294.3	6
Xu and Lang (2014)	CO_2	Tert-butylamine	2270-13790	273.5-283.3	5

2.5   Effects of promoters on the hydrate formation rate

Research on hydrate studies has illustrated that the equilibrium pressure and temperatures are intensely affected by the introduction of hydrate promoters such as tetrabutyl ammonium salts (Refer to section 2.4). However such promoters may result in a decrease of the rate of hydrate formation. It is important to identify the parameters that affect the rate hydrate formation in order to appropriately monitor the effects of promoters.

Hydrate formation is a three-stage sequence:
1. Dissolution: The passing of the gas from the vapour phase to the aqueous liquid phase.
2. Nucleation: The diffusion of the gas from aqueous phase to the hydrate-liquid interface. The time occupied for the diffusion process is referred as induction time.
3. The reaction of the gas with the aqueous phase, initiating gas hydrate crystallization and further crystal growth (Brown et al., 2010).

The rate of hydrate formation is the time required for the completion of the three-stage process. Hydrate formation may require 6 hours to 2 weeks for completion depending on the system species. Hydrate promoters may stimulate the thermodynamic and kinetic processes of hydrate formation (Brown et al, 2010). The main parameter affecting such processes is gas solubility.

The hydrate nucleation process entails the formation and growth of the hydrate nuclei to a critical size. The growing clusters of gas and water molecules act as precursors to hydrate nuclei formation. Once growing hydrate nuclei attain critical radius, the nuclei are stable and the continued growth of the hydrate is enabled. Nuclei smaller than the critical radius are re-dissolved into the liquid medium (Brown et al., 2010). Nuclei growth occurs under conditions of sufficient gas presence in the structured water environment. Hence the nucleation process and induction time is dependent of gas solubility and supersaturation. Figure 2-9 illustrates the conventional relationship between supersaturation and induction time. Supersaturation is the driving force of gas hydrate formation. As supersaturation decreases, the induction time increases until it reaches a critical point. Once supersaturation has reached the critical point, hydrate formation does not occur (Sabil, 2009).
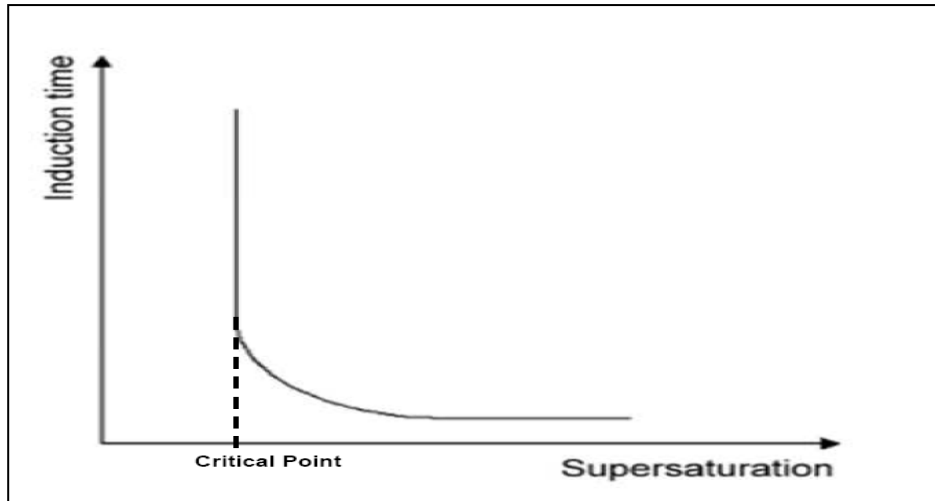
Figure 2-9: Schematic representation of relationship between induction and supersaturation (Sabil, 2009).

Supersaturation of the structured water environment is dependent on the gas solubility and the rate of gas dissolution. Solutions, consisting of a high concentrate tetrabutyl ammonium salt, are substantially viscous solutions and may lead to a reduction in gas solubility. Hydrate formation occurs through constant cooling up to temperatures of 273.65 K. During the cooling process, the tetrabutyl ammonium salt solutions increase in viscosity. Thus the gas solubility and the hydrate formation rate decreases with the progression of the hydrate formation process.

.

.

CHAPTER THREE

MODELLING OF PHASE BEHAVIOUR FOR HYDRATE-VAPOUR-LIQUID EQUILIBRIA

In order to design efficient CCS processes, reliable and accurate phase equilibrium data is required. Such data can be obtained through dependable experimental measurements achieved from acceptable and innovative experimental procedures, techniques and apparatus. However it is time-consuming, costly and impractical to measure phase equilibrium data of every possible combination of components, hence accurate mathematical calculations for the prediction of hydrate phase equilibria data is necessary (Bouchemoua, 2009). This chapter briefly addresses various thermodynamic models for the prediction of hydrate phase equilibrium data and elucidates the available thermodynamic models for the prediction of semi-clathrate hydrates.

Hydrate-Vapour-Liquid (H-V-L) Equilibria

Phase equilibrium is the most frequently investigated subject pertaining to gas hydrates. A solid gas hydrate may exist in equilibrium with gas and aqueous solution of the promoter. This is known as hydrate-vapour-liquid equilibrium. Figure 3-1 below illustrates a H-V-L equilibrium curve for the methane + water system. Hydrates can only form at a lower temperature and higher pressure than the equilibrium curve (Mork, 2002). The distance from the hydrate-forming conditions and equilibrium conditions is the driving force for hydrate formation. Hence the more the system deviates from the equilibrium curve, the higher the gas-hydrate formation rate (Beltran et al., 2012).
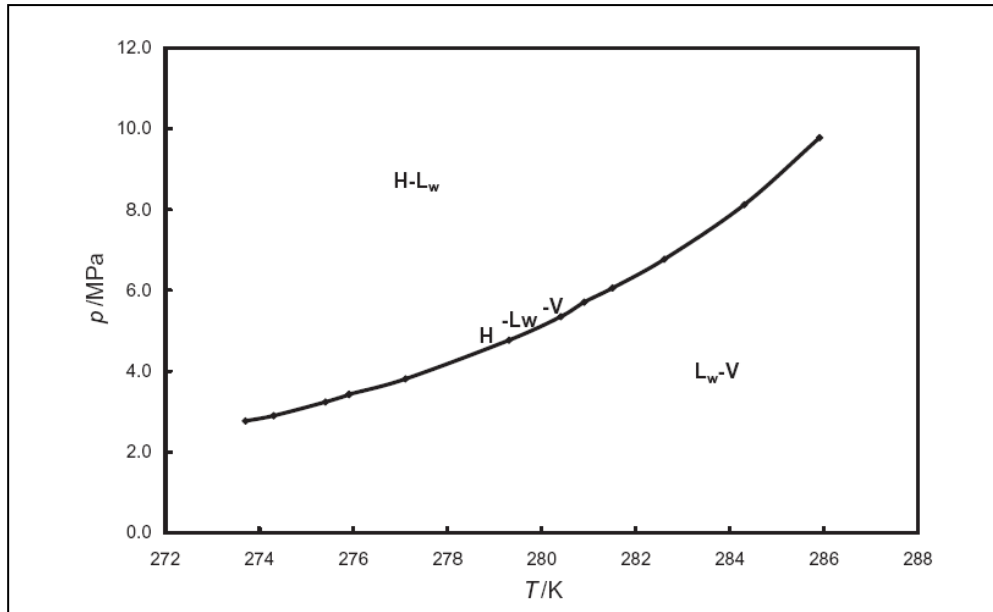
Figure 3-1: Phase equilibrium curve for a methane + water system (Beltran et al., 2012).

When a three-phase equilibrium is present for a two-component system, the system is monovariant by the Gibbs phase rule. Thus, by specifying the temperature, the total vapour pressure may be obtained. A three-component system, consisting of TBAC + gas + H_2O, may obtain the total vapour pressure by specifying temperature and the TBAC composition (Coa, 2002).

3.1   Review of hydrate phase equilibrium models

Simple hydrate estimation techniques

Estimation techniques are computationally non-demanding methods used for the rough prediction of pure gas hydrates. Such techniques are useful for the prediction of approximate hydrate phase equilibrium of pure CO_2 hydrates.

Kamath (1984) proposed an exponential correlation for the estimation of liquid water-hydrate-vapour (L_w-H-V) and ice-hydrate-vapour (I-H-V) equilibrium of simple gas hydrates including CO_2, nitrogen, methane and ethane. The correlation has been established to be accurate within the specified temperature limits and cannot be used to predict phase equilibrium data beyond the quadruple points Q_1 and Q_2 (Sloan and Koh, 2008).

$$P = exp\left(a + \frac{b}{T}\right) \tag{3.1}$$

P - equilibrium pressure (kPa)

T - equilibrium temperature (K)

a,b - gas-dependent hydrate equilibrium parameters valid within a temperature range presented in Table 3-1.

Table 3-1: Hydrate formation parameters for the prediction of simple natural gas hydrates using the correlation of Kamath (1984).

Component	Type	T range (°C)	a	b
Methane	L_W–H–V	0 to 25	38.980	−8533.80
Methane	I–H–V	−25 to 0	14.717	−1886.79
Ethane	L_W–H–V	0 to 14	44.273	−10424.25
Ethane	I–H–V	−25 to 0	17.511	−3104.54
Propane	L_W–H–V	0 to 5	67.130	−16921.84
Propane	I–H–V	−25 to 0	17.156	−3269.65
Isobutane	L_W–H–V	0 to 1.5	61.740	−15571.43
Isobutane	I–H–V	−25 to 0	18.950	−3887.32
Carbon dioxide	L_W–H–V	0 to 11	44.580	−10246.28
Carbon dioxide	I–H–V	−25 to 0	18.594	−3161.41
Nitrogen	L_W–H–V	0 to 25	37.808	−7688.63
Nitrogen	I–H–V	−25 to 0	15.129	−1504.28
Hydrogen sulfide	L_W–H–V	0 to 25	34.828	−8266.10
Hydrogen sulfide	I–H–V	−25 to 0	16.560	−3270.41

The simplest method for the estimation of hydrate equilibrium data is the gas gravity method. Gas gravity stands for the ratio of molecular weight of the hydrate-forming gas to that of air. The gas gravity is calculated and the hydrate equilibrium pressure is determined at a given temperature on the chart (Refer to Figure 3-2).   The gas gravity estimation is uncomplicated but should be considered as approximate. This method is often used as a rough estimation in the petroleum industry (Sloan and Koh, 2008).
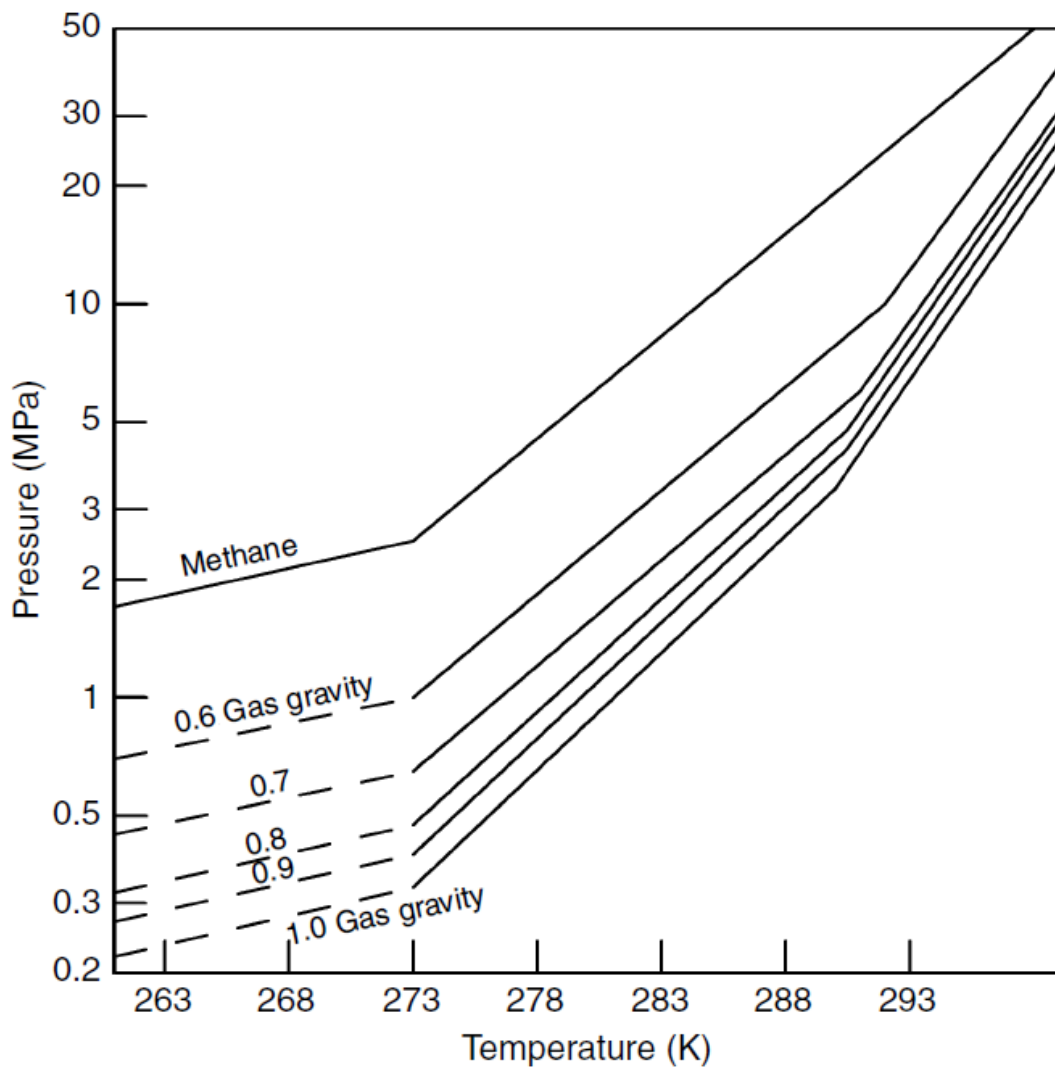
Figure 3-2: The gas gravity chart for prediction of L_w-H-V equilibrium (Sloan and Koh, 2008).

Statistical thermodynamic approach

Estimation techniques utilize macroscopic thermodynamic properties to provide a rough estimate of simple gas hydrates. Statistical thermodynamic models provide rigorous hydrate equilibrium predictions with use of macroscopic thermodynamic properties in addition to molecular crystal structure properties (Sloan and Koh, 2008). Hydrate phase equilibrium curves may be accurately predicted by means of statistical thermodynamic models. The first model for calculating hydrate equilibrium data was that of van der Waals and Platteeuw (1959). Most thermodynamic hydrate models proposed to date originate from the van der Waals and Platteeuw model (1959). The main drawback of the model is that it does not account for multiple guest molecules. This was later corrected by Parrish and Prausnitz(1972) (Klauda and Sandler, 2000). Only two statistic thermodynamic models (Parichaud, 2011 and Eslamimanesh, 2012) have been proposed for the prediction thermodynamic equilibrium of semi-clathrates. Both statistical models are based on the fundamental modelling of van der Waals and Platteuw (1959), Parrish and Prausnitz (1972) and Klauda and Sandler (2000). A review on the development of semi-clathrate models is presented below.

3.2 Thermodynamic Phase Equilibrium

Multiple phases at the same temperature and pressure are in equilibrium when the chemical potential of each species is the same in all phases (Smith et al., 2005). Statistical thermodynamic modelling of the H-V-L equilibria is based on the equality of the chemical potential (μ_i) between the hydrate phase, liquid phase and vapour phase. For a H-V-L system in equilibrium, the chemical potential can be expressed as:

$$\mu_i^H = \mu_i^L = \mu_i^G \tag{3.2}$$

Chemical potential can be expressed in terms of fugacity to produce a general phase criterion, whereby a species is in equilibrium when each phase has the same temperature, pressure and fugacity (Smith et al., 2005):

$$\hat{f}_{H_2O}^H = \hat{f}_{H_2O}^V = \hat{f}_{H_2O}^L \tag{3.3}$$

$\hat{f}_i^H$ - fugacity in solution of species i in the hydrate phase

$\hat{f}_i^L$ - fugacity in solution of species i in the liquid phase

$\hat{f}_i^V$ - fugacity in solution of species i in the vapour phase

At hydrate-vapour-liquid (H-V-L) equilibrium, it can be assumed that the H_2O content in the vapour phase is negligible:

$$\hat{f}_{H_2O}^V = \hat{f}_{H_2O}^L \tag{3.4}$$

Since the promoters utilized in this study are tetrabutyl ammonium salts (ionic liquids), it is assumed that a negligible concentration of promoter is present in the vapour phase. The phases and species that exist at hydrate-vapour-liquid equilibrium are recapitulated in Table 3-2.

Table 3-2: Existing phases at H-V-L equilibrium.

Hydrate Phase	Vapour Phase	Liquid Phase
CO_2	CO_2	CO_2
H_2O	-	H_2O
Promoter (TBAC/F)	-	Promoter (TBAC/F)

Thermodynamic Model of the Vapour Phase

The fugacity in solution of the vapour phase can be expressed as (Smith et al., 2005):

$$\hat{f}_i^V = y_i \hat{\phi}_i^V P \tag{3.5}$$

$\hat{f}_i^V$ - fugacity in solution of component i in the vapour phase at a pressure P.

y_i - mole fraction of component i in the vapour phase at a pressure P.

$\hat{\partial}_i^V$ - fugacity coefficient in solution of component i in the vapour phase at a pressure P. $\hat{\partial}_i^v$ can be determined by an equation of state (EOS). An appropriate EOS is presented further in this chapter.

Thermodynamic Model for the Liquid Phase

The fugacity in solution of the liquid phase can be expressed as (Smit el al., 2005):

$$\hat{f}_i^L = x_i \hat{\partial}_i^L P \qquad (3.6)$$

$\hat{f}_i^L$ - fugacity in solution of component i in the liquid phase at a pressure P.

x_i - mole fraction of component i in the liquid phase at a pressure P.

$\hat{\partial}_i^L$ - fugacity coefficient in solution of component i in the liquid phase at a pressure P.

In an aqueous phase without the presence of electrolytes, the fugacity coefficient in solution is calculated by an equation of state. If electrolytes are present, a correction factor is adopted to account for the electrostatic interactions (Englezos., 1992). A model presented by Aasberg-Peterson et al. (1992) may be used to account for:

a) CO_2-H_2O interactions

b) H_2O-electrolyte interactions

c) CO_2-electrolyte interactions

The fugacity coefficient is initially calculated on a salt-free basis, which is then corrected with the Debye-Hückel electrostatic term ($\gamma_i^{l,EL}$). This term is dependent on the electrostatic concentration in the liquid phase, hence:

$$\ln\Phi_i^L = \ln\Phi_i^{L,A-P} = \ln\Phi_i^{L.EOS} + \ln\gamma_i^{L,EL} \qquad (3.7)$$

Φ_i^{A-P} - fugacity coefficient of the liquid phase, calculated by Aasberg-Peterson et al. (1991).

Φ_i^{EOS} - fugacity coefficient of liquid phase, calculated by an equation of state, discussed in the forthcoming section.

γ_i^{EL} - activity coefficient of the electrolyte solution.

Mole fractions used in equation (3.6) are on a salt-free basis and are defined as:

$$x_i = \frac{\varepsilon_i}{(1-\sum_j \varepsilon_j)} \tag{3.8}$$

ε_i - true liquid mole fraction of component i

ε_j - mole fraction of salt j

The activity coefficient of the electrolyte solution is defined as:

$$\ln\gamma_i^{l,EL} = \frac{2A\rho_{is}M_m F\ (BI^{0.5})}{B^3} \tag{3.9}$$

ρ_{is} - the interaction coefficient between the dissolved salt and non-electrolyte component.

M_m - molecular weight of salt free solution.

A, B and F = parameters of equation (3.9).

$$A = 1.327757 \times 10^5 \frac{d_m^{0.5}}{(E_m T)^{0.5}} \tag{3.10}$$

$$B = 6.359696 \times \frac{d_m^{0.5}}{(E_m T)^{0.5}} \tag{3.11}$$

$$E_m = x_N E_N \tag{3.12}$$

$$F\ (BI^{0.5}) = 1 + (BI^{0.5}) - \frac{1}{1 + (BI^{0.5})} - 2\ln(1+BI^{0.5}) \tag{3.13}$$

d_m - density of salt free mixture

E_m - dielectric constant of salt-free mixture

x_N - salt-free mole fraction of water

E_N - dielectric constant of water

I - ionic strength

In the presence of the tetrabutyl ammonium salt promoters, a weak electrolyte interaction may be assumed ($\ln\gamma_i^{L,EL} = 0$), hence:

$$\Phi_i^L = \Phi_i^{L.EOS} \qquad (3.14)$$

The liquid phase fugacity may also be expressed in terms of the activity coefficient and saturated pressure.

$$\hat{f}_i^L = x_i\gamma_i P \qquad (3.15)$$

γ_i - activity coefficient of component i. An appropriate activity coefficient model is discussed in the forthcoming section.

Modelling of the vapour liquid equilibrium (VLE) data

There are two common methods for the correlation of VLE data:

1. The direct method or phi-phi method.
2. The combined method or gamma-phi method.

The combined method utilises an equation of state and an activity coefficient model to describe the vapour non-idealities and liquid non-idealities respectively. The direct method describes both the liquid and vapour non-idealities with the use of an equation of state (Raal and Müllbauer, 1998).

Direct method (phi/phi method)

Combing equations (3.5) and (3.6) gives:

$$y_i\hat{\varnothing}_i^V P = x_i\hat{\varnothing}_i^L P \tag{3.16}$$

The combined method provides an accurate representation of VLE systems at critical and supercritical pressures. Figure 3-3 illustrates an iteration scheme for an isothermal bubble-pressure calculation.

Combined method(Gamma/phi method)

Equating equation (3.5) and equation (3.15) gives:

$$y_i\hat{\varnothing}_i^V P = x_i\gamma_i P_i^{sat} \tag{3.17}$$

The direct method is applicable to system having low to moderate pressures (Raal and Mühlbauer, 1990). Figure 3-4 illustrates an iteration scheme for a bubble-pressure calculation.
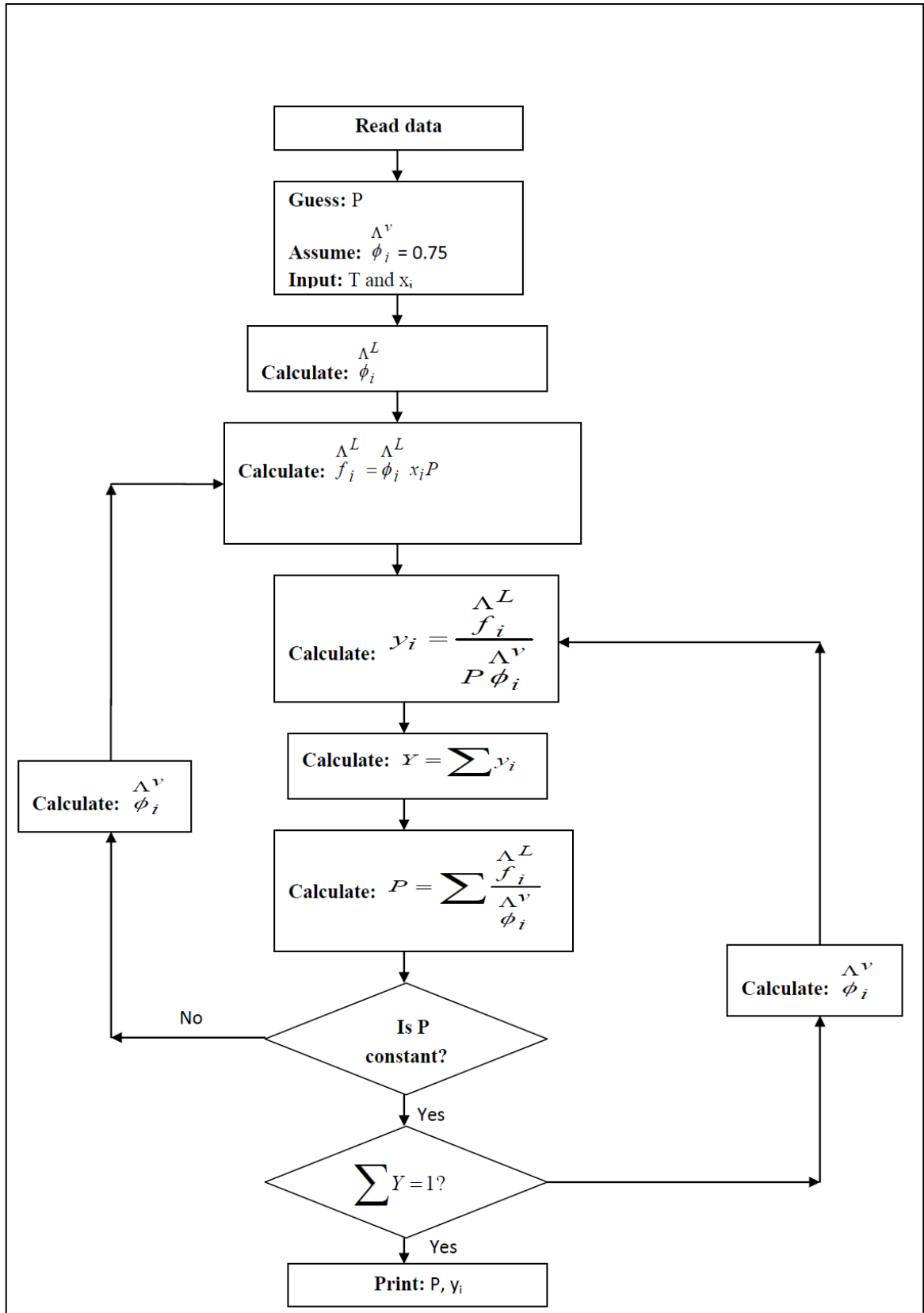
Figure 3-3: Flow diagram for the phi-phi method of calculation of isothermal bubble-pressure (Prausnitz and Chueh, 1968).

Read data

Guess: P
Assume: $\phi_i^v = 1$
Input: T and x_i

Calculate: $f_i^{0\ (Po)}$, $\gamma_i^{(Po)}$, $\bar{V}_i^L$

Calculate:
$$\overset{\Lambda}{f_i^L} = \gamma_i^{(Po)} x_i f_i^0 \exp\left[\frac{P\bar{V}_i^L}{RT}\right]$$

Calculate: $y_i = \dfrac{\overset{\Lambda}{f_i^L}}{P\overset{\Lambda}{\phi_i^v}}$

Calculate: $Y = \sum y_i$

Calculate: $P = \sum \dfrac{\overset{\Lambda}{f_i^L}}{\overset{\Lambda}{\phi_i^v}}$

Calculate: $\overset{\Lambda}{\phi_i^v}$

Is P constant?

No

Yes

Calculate: $\overset{\Lambda}{\phi_i^v}$

$\sum Y = 1$?

Yes

Print: P, y_i
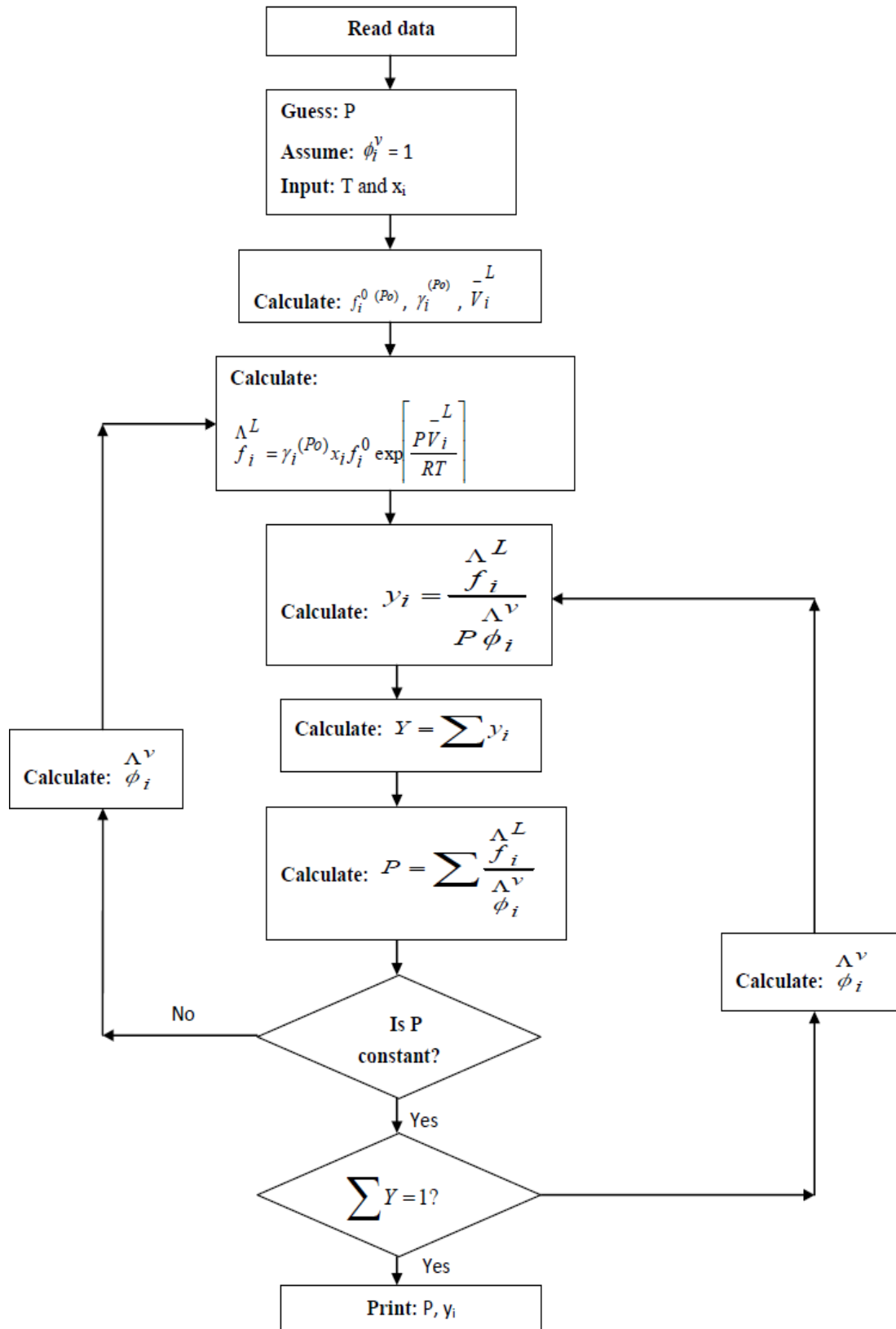
Figure 3-4: Flow diagram for the gamma-phi method of calculation of isothermal bubble-pressure (Prausnitz and Chueh, 1968).

Equations of State (EOS)

The fugacity coefficient of both the vapour and liquid phases may be described by the use of an equation of state. A reliable EOS is required to accurately calculate the fugacity coefficients. The selection of an appropriate equation is difficult since there are hundreds of equations of state published in literature to date. The cubic equations of state are the simplest and most widely used EOS.

Most equations of state are categorized as one of three classes:

1. Empirical
2. Theoretical
3. Semi-empirical (semi-theoretical)

Empirical equations are obtained by fitting experimental data to a multi-parameter function. The disadvantage of such an equation is that it requires large amounts of experimental data and cannot be extended to mixtures. Theoretical equations of state are applicable to a wider range of systems obeying the given intermolecular potential model. Semi-empirical equations are derived from a theoretically-based functional form of EOS, consist of only a few adjustable parameters to represent the experimental data and are the most practical. The EOS by Peng and Robinson (1976) is an example of a semi-theoretical EOS.

Zhang (2006) modelled the vapour and liquid phases of hydrocarbon hydrates with the use of a modified version of the Peng-Robinson equation of state, which was reported to provide accurate predictions of VLE for pure species and mixtures. The Peng and Robinson (1976) EOS was developed to improve the accuracy of the Soave-Redlick Kwong (1972) EOS predictions. The advantage of such a model is that it can easily correlate the phase behaviour of pure component and multi-component systems and requires little input information. The disadvantage of the Peng-Robinson EOS is that it does not provide accurate predictions of highly polar molecules, hydrogen-bonded compounds and electrolytes (Stryjek and Vera, 1986).

The Peng-Robinson equation of state has been used frequently in hydrate phase equilibrium research since it can easily correlate behaviour of pure and multi-component systems. The equation of state requires a few adjustable parameters thus the computer regression time is moderately short. For further details on the advantages and disadvantages of the Peng-Robinson equation of state compared to other EOSs, the reader is referred to Coquelet (2003).

The expression for fugacity coefficient in the vapour phase is given by the Peng-Robinson equation of state (Peng and Robinson, 1976):

$$\ln\hat\varnothing_i = \frac{b_i}{b_m}(Z-1) - \ln(Z-B) - \frac{A}{2\sqrt{2}B}\left(\frac{2\sum_k y_k a_{i,k}}{a_m} - \frac{b_i}{b_m}\right)\ln\left(\frac{Z+(1+\sqrt{2})B}{Z+(1-\sqrt{2})B}\right) \qquad (3.18)$$

$$a_i = \left(0.45724\frac{R^2T^2}{P_c}\right)\alpha_i \qquad (3.19)$$

$$b_i = (0.07780)\frac{RT_c}{P_c}) \qquad (3.20)$$

$$\alpha_i = \left[1 + \frac{k_i}{(1-\sqrt{T/T_{c_i}})}\right]^2 \qquad (3.21)$$

$$k_i = 0.37464 + 1.54226\omega_i - 0.26992\omega_i{}^2 \qquad (3.22)$$

$$A = \frac{a_m P}{R^2T^2} \qquad (3.23)$$

$$B = \frac{b_m P}{RT} \qquad (3.24)$$

Z - compressibility factor.

a_i - constant related to the intermolecular attraction force of molecules.

b_i - constant that accounts for the molecular size of the molecule.

k_i - the binary interaction parameter, unique to each binary system. This parameter is obtained through the regression of VLE data.

ω - acentric factor

For a two-component mixture, the largest root of equation (3.4.8) corresponds to the compressibility factor (Z) of the vapour phase:

$$Z^3 - (1 - B)Z + \{A - 3(B)^2\}Z - \{AB - (B)^3\} = 0 \qquad (3.25)$$

a_m and b_m are obtained from van der Waals classical mixing rules:

$$a_m = \sum_i \sum_j x_i x_j a_{ij} \qquad (3.26)$$

$$b_m = \sum_i x_i \, b_i \qquad (3.27)$$

$$a_{ij} = \sqrt{a_i a_j} \, (1 - \delta_{ij}) \qquad (3.28)$$

Activity coefficient model

The Non Random Two Liquid (NRTL) model proposed by Renon and Prausnitz (1968) is applicable to a wide variety of mixtures for calculation of the activity coefficient of highly non-ideal solutions. The model is readily generalized to multi-component systems. The NRTL model can be used to calculate the activity coefficient of water in the aqueous phase. For further details on the advantages and disadvantages of the NRTL model compared to other activity coefficient models, the reader is referred to Walas (1985).

$$ln\gamma_1 = x_2{}^2 \left[\tau_{21}\left(\frac{G_{21}}{x_1 + G_{21}x_2}\right)^2 + \frac{\tau_{12} \, G_{12}}{(G_{12} \, x_1 + x_2)^2} \right] \qquad (3.29)$$

$$ln\gamma_2 = x_1{}^2 \left[\tau_{12}\left(\frac{G_{12}}{x_2 + G_{12}x_2}\right)^2 + \frac{\tau_{21} \, G_{21}}{(G_{21} \, x_2 + x_1)^2} \right] \qquad (3.30)$$

$$G_{12} = \exp(-\alpha_{12}\tau_{12}) \qquad (3.31)$$

$$G_{21} = \exp(-\alpha_{21}\tau_{21}) \qquad (3.32)$$

$$\tau_{12} = \frac{A_{12}}{RT} \qquad (3.33)$$

$$\tau_{21} = \frac{A_{21}}{RT} \qquad (3.34)$$

A_{12} - adjustable energy parameter for interaction between species 1 (H_2O) and species 2 (CO_2)

A_{21} - adjustable energy parameter for interaction between species 2 (CO_2) and species 1 (H_2O)

$\alpha_{12,}\alpha_{21}$ - adjustable parameter for characteristic of randomness of the mixture.

Walas (1985) estimated $\alpha_{12} = \alpha_{21} = 0.3$ for non-aqueous mixtures.

3.3 Thermodynamic Model for the Hydrate Phase

Literature on hydrate phase equilibrium illustrates two common categories of hydrate phase equilibrium models i.e. equality of chemical potentials and equality of fugacities. Most methods for the calculation of hydrate phase equilibrium are based on the van der Waals and Platteeuw (1959) model with certain generalizing assumptions. The fugacity-based equilibrium models were developed as simplifications of the van der Waals and Platteuw (1959) and Parrish and Prausnitz (1972) models, which are based on the equality of chemical potentials.

The Van der Waals and Platteeuw model (1959)

The first statistical model capable of predicting hydrate phase equilibrium data was developed by van der Waals and Platteeuw (1959).The model is based on the equality of the chemical potential of the hydrate phase and liquid phase. The gaseous species encapsulated in the hydrate lattice is treated as a gas adsorbed onto a solid, where the hydrate cages are adsorption sites.

The model was based on following assumptions (Sloan and Koh, 2008):

1. Each cavity may contain a maximum of one guest molecule.
2. All hydrate cavities are considered spherically shaped.
3. Guest-guest molecule interaction is neglected. Guest molecules interact with the nearest water molecules only.
4. The guest molecules do not deform the cavities.
5. The ideal gas partition function is applicable to guest molecules.

The van der Waals and Platteuw model is based on the equality of chemical potential of water between the hydrate phase (H) and the co-existing liquid water phase (L) (Holder et al. 1980). The assumption of negligible water in the vapour phase is held:

$$\Delta\mu_w{}^{H\text{-}\beta} = \Delta\mu_w{}^{L\text{-}\beta} \tag{3.35}$$

β - a hypothetical phase representing a metastable empty hydrate lattice. This lattice is thermodynamically unstable since hydrates require guest molecules to stabilize the crystal lattice (Klauda and Sandler, 2003).

$\Delta\mu_w{}^{H\text{-}\beta}$ - difference in chemical potential between water in the hydrate phase and empty lattice.

$\Delta\mu_w{}^{L\text{-}\beta}$ - difference in chemical potential between water in the liquid phase and empty lattice.

$\Delta\mu_w{}^{L\text{-}\beta}$ is calculated using classical thermodynamics, the Gibbs-Duhem equation and $\Delta\mu_w{}^{H\text{-}\beta}$ is calculated using statistical thermodynamics:

$$\Delta\mu_w{}^{H\text{-}\beta} = RT \sum_i v_i \ln(1 - \theta_j^i) \tag{3.36}$$

v_i - number of hydrate cavities of type i per molecule of water.

θ_j^i - occupancy factor of cavity i by gas molecule j.

R - universal gas constant

The occupancy factor (θ_j^i) is described by a model based on Langmuir adsorption. The model is based on the following assumptions:

1. The guest molecule is encaged at discrete cavities of the lattice.
2. The encapsulation energy is independent of the presence of other encaged molecules.
3. Each cavity may contain a maximum of one molecule.
4. Gas encapsulation occurs by the collision of gas molecules with empty cavities.
5. The hydrate dissociation rate depends on the amount of guest molecules.

Hence:

$$\theta_j^i = \frac{C_j^i P}{1 + \sum C_j^i P} \tag{3.37}$$

C_j^i - Langmuir constant of cavity i occupied by gas molecule j

Van der Waals and Platteeuw derived an equation for the Langmuir constant (C_j^i) based on the Lennard-Jones-Devonshire cell theory:

$$C_j^i = \frac{4\pi}{kT} \int_0^{Rc} (\frac{-w(r)}{kT}) r^2 dr \qquad (3.38)$$

k -Boltzmann's constant = 1.38×10^{-23} J/K.

R_c - cavity radius

w - interaction potential between the hydrate cavity and guest molecule.

r - distance between guest molecule and water molecule.

Hence the function $w(r)$ is the spherically symmetric cell potential in the cavity and depends on the intermolecular potential function chosen for describing the encaged gas-water interaction.

Parrish and Prausnitz (1972) model

The Parrish and Prausnitz (1972) model is a modification of the van der Waals and Platteeuw (1959) model. The model consists of three distinct differences from the original van der Waals and Platteeuw (1959):

Parrish and Prausnitz (1972) extended the model to multi-component hydrate systems:

$$\Delta\mu_w^{\text{H-}\beta} = RT\sum_i v_i \ln(1 - \sum_j \theta_j^i) \qquad (3.39)$$

The occupancy factor (θ_j^i) was described in terms of fugacity and not partial pressures. This modification

    a) allowed the model to account for non-idealities in the gas phase

    b) extended the model to higher pressures.

$$\theta_j^i = \frac{C_j^i f_j}{1 + \sum_j C_j^i f_j} \qquad (3.40)$$

To avoid a time-consuming integration of the interaction potential, Parrish and Prausnitz (1972) proposed a simplified expression for the Langmuir constant:

$$C_j^i = \frac{A_j^i}{T}\exp\left(\frac{B_j^i}{T}\right) \tag{3.41}$$

A and B are constants provided by Munck et al. (1988) as provided in Table 3-3.

Table 3-3: N_2 and CO_2 parameters required for the calculation of Langmuir constant (260 K – 300 K) (Munk et al., 1988).

Guest	Structure	Small Cavity		Large Cavity	
		A	B	A	B
CO_2	I	2.474×10^{-4}	3.41×10^{3}	4.246×10^{-2}	2.813×10^{3}
	II	8.45×10^{-5}	3.615×10^{3}	8.51×10^{-1}	2.025×10^{3}
N_2	I	1.617×10^{-3}	2.905×10^{3}	6.078×10^{-3}	2.431×10^{3}
	II	1.742×10^{-4}	3.082×10^{3}	1.8×10^{-2}	1.728×10^{3}

The Klauda and Sandler (2003) model

Klauda and Sandler (2003) developed a model, based on the equality of fugacities, to predict phase equilibria data based on modifications from that of van der Waals and Platteeuw (1959). The assumptions include:

1. Guest molecules distort the hydrate cavity.
2. Guest molecules do not interact with the nearest water molecules only. Guest-H_2O interaction extends beyond the first shell of water molecules.
3. Guest-guest interaction is accounted for.

The distortion of the hydrate lattice by guest molecules is accounted for by the guest-dependent vapour pressure of the hydrate and Langmuir constant. The Langmuir constant also accounts for interaction between guest-hydrate interactions as well as guest-guest interactions.

The fugacity of water in the hydrate phase is expressed as:

$$\hat{f}_w^H = \hat{f}_w^\beta \exp(\frac{-\Delta\mu_w^{H-\beta}}{RT}) \tag{3.42}$$

$\hat{f}_w^\beta$ - fugacity of water in hypothetical phase β (empty hydrate lattice), calculated from equation (3.43).

$\Delta\mu_w^{H-\beta}$ - calculated from the van der Waals and Platteeuw model, equation (3.36)

Fugacity of water in the empty lattice is expressed as:

$$\hat{f}_w^\beta = P_w^{sat,\beta} \Phi_w^\beta \exp(\frac{V_w^\beta(P-P_w^{sat,\beta})}{RT}) \tag{3.43}$$

V_w^β - molar volume of the empty hydrate lattice.

$P_w^{sat,\beta}$ - vapour pressure of water in empty hydrate lattice, calculated by equation (3.57).

Since the vapour pressure of the water phase is low, $\Phi_w^\beta = 1$, and equation (3.43) becomes:

$$\hat{f}_w^\beta = P_w^{sat,\beta} \exp(\frac{V_w^\beta(P-P_w^{sat,\beta})}{RT}) \tag{3.44}$$

Model parameters

The crystal lattice size or the molar volume of the empty hydrate (β) is dependent on the guest molecule type and system temperature; however there is limited data on the temperature dependence of the molar volume for the specific guest molecule (CO_2) therefore it is assumed that the molar volume is independent of guest molecule and expressed as:

$$V_w^{\beta,I} = (11.835 + 2.217 \times 10^{-5}T + 2.242 \times 10^{-6}T^2)\frac{10^{-30}N_A}{N_w^\beta} -$$

$$8.006 \times 10^{-9}P + 5.448 \times 10^{-12}P^2 \tag{3.55}$$

$$V_w^{\beta,II} = (17.315 + 2.249 \times 10^{-4}T + 2.013 \times 10^{-6}T^2 + 1.009 \times 10^{-9}T^3)\frac{10^{-30}N_A}{N_w^\beta} -$$

$$8.006 \times 10^{-9}P + 5.448 \times 10^{-12}P^2 \qquad (3.56)$$

N_A - Avogadro's number

N_w^β - number of water molecules in β phase.

The vapour pressure function proposed by Klauda and Sandler (2003) is far superior to the Antoine's equation and most other vapour pressure functions due to its accuracy in extrapolation. The following equation was proposed for the vapour pressure of the empty gas hydrate (β):

$$\ln P_w^{sat,\beta} = A_{mix}^\beta \ln(T) + \frac{B_{mix}^\beta}{T} + C^\beta + D_{mix}^\beta T \qquad (3.57)$$

A_{mix}^β, B_{mix}^β and D_{mix}^β are calculated by the proposed mixing rule:

$$X_{mix}^\beta = \sum_{i=1}^{\substack{number of \\ guest molecules}} z_i X_i \qquad (3.58)$$

z_i - overall composition of guest i in hydrate phase.

X_i - vapour pressure constant of component i.

A_{mix}^β, B_{mix}^β and D_{mix}^β are fit to gas hydrate equilibrium data. C^β was assumed independent of the guest molecule.

Klauda and Sandler (2003) developed a more rigorous calculation of the Langmuir constant than that proposed by van der Waals and Platteeuw (1959):

$$C_j^i = \frac{1}{RT} \int \int \exp[-\frac{w^{gi}(\underline{r},\Omega) + w^{gg}(\underline{r},\Omega)}{kT} d\underline{r}d\underline{\Omega} \qquad (3.59)$$

$\underline{r}$ - position vector

$\underline{\Omega}$ - orientation vector of the guest in the cage

w^{gi} - guest-hydrate interaction energy

w^{gg} - guest-guest interaction energy

The model of Eslamimanesh (2012)

Eslamimanesh (2012) presented the only fugacity-based thermodynamic model for the prediction of semi-clathrates in the presence of tetrabutyl ammonium salt. The model accounts for the presence of tetrabutyl ammonium bromide (TBAB) in the aqueous solution and the semi-clathrate crystal structure. This research project involved the adaption of the Eslamimanesh (2012) model to account for the presence of tetrabutyl ammonium salts, TBAC and TBAF.

Hydrate phase

This fugacity based hydrate model has two modifications to the Klauda and Sandler (2003) model:

1. Modification of the Langmuir constants. The Langmuir constants correlation includes a correction factor to account for disorders in structures resulting from the presence of the tetrabutyl ammonium salt.
2. The vapour pressure of the empty hydrate lattice is calculated using the method of Dharmawardhana et al. (1980); to account for the presence of the tetrabutyl ammonium ion (Cl- and F⁻) bonded to the hydrate cage.

$\Delta\mu_w^{H-\beta}$ is calculated with a modified van der Waals and Platteeuw (1959) model:

$$\frac{\Delta\mu_w^{H-\beta}}{RT} = \sum_i v_i \ln(1 - \frac{C_j^i \hat{f}_j}{1 + \sum_j C_j^i \hat{f}_j}) = \sum_i v_i \ln(\frac{1}{1 + \sum_j C_j^i \hat{f}_j}) = \sum_i \ln(1 + \sum_j C_j^i \hat{f}_j)^{-v_i} \quad (3.60)$$

Hence replacing equations (3.42) and (3.44) in equation (3.60), the fugacity of water in the hydrate phase becomes:

$$\hat{f}_w^H = P_w^\beta \exp\left(\frac{v_w^\beta (P - P_w^\beta)}{RT}\right) \sum_i \left(1 + \sum_j C_j^i \hat{f}_j\right)^{-v_i} \tag{3.61}$$

P_w^β - vapour pressure of the empty hydrate lattice.

Liquid phase

To account for the presence of the tetrabutyl ammonium salt, the concentration of water in the aqueous phase is determined by applying the following correlation:

$$x_w^l = \frac{1}{1 + 0.001 \times 2 \times m \times M_w} - x_g^l \tag{3.62}$$

m - molality of aqueous solution (mol.kg^{-1})

M_w - molecular weight of water (g.mol^{-1})

x_g^l - solubility of hydrate-forming gas (g) in the liquid phase.

The molality is defined as the moles of tetrabutyl ammonium salt per kg mass of water:

$$m = \frac{18.0153 x_{TBA+}}{1000 x_w} \tag{3.6.3}$$

x_{TBA+} is the moles of TBA$^+$ cations

x_w is the mass of water (kg)

The solubility of the hydrate-forming gas in the liquid phase is calculated using the Krichevsky and Kasarnovsky (1935) equation:

$$x_g^l = \frac{f_g^V}{H_{g-w} \exp\left(\frac{v_g^\infty}{RT}(P - P_w^{sat})\right)} \tag{3.64}$$

H_{g-w} is Henry's constant of gas in water.

v_g^∞ - molar volume of gas at infinite dilution.

f_g^V can be calculated using the Peng-Robinson EOS discussed previously.

The fugacity of the promoter (tetrabutyl ammonium salt) in the liquid phase (f_p^L) is expressed as:

$$\hat{f}_p^L = x_p^L \gamma_p^L P_p^{sat} \exp\left(\frac{V_p^L(P - P_p^{sat})}{RT} \right) \tag{3.65}$$

x_p^L - mole fraction of the promoter in the aqueous phase

γ_p^L - activity coefficient of the hydrate promoter in the aqueous phase.

V_p^L - molar volume of hydrate promoter in the aqueous phase.

P_p^{sat} -vapour pressure of promoter.

Tetrabutyl ammonium salts are non-volatile ionic liquids. Hence $P_p^{sat} = 0$.

Since tetrabutyl ammonium salt, dissolved gas and water are present in the liquid phase, the fugacity of water in the liquid phase is expressed as:

$$\hat{f}_w^L = x_w^L \gamma_w P_w^{sat} \exp\left(\frac{V_w^L(P - P_w^{sat})}{RT} \right) \tag{3.66}$$

x_w^L - mole fraction of water in the aqueous phase

γ_w -activity coefficient of water

V_w^L - molar volume of liquid water

Crystallographic data of tetrabutyl ammonium salts similar to that of TBAC and TBAF describe the TBA$^+$ cation occupying tetrakaidecahedra and pentakaidecahedra cages (2 large cages) and the hydrate-forming gas occupying a dodecahedral (small) cage.

TBAC semi-clathrates form three crystal structures (Type A, B and C) (Maniko et al. 2010). TBAF semi-clathrates form two crystal structures (Type A and B) (Lee at el, 2010b). Each crystal structure contains a specified number of water molecules (hydrate number) and a specified number of available cavities depending on the type of crystal structure formed (Type A, B or C).

Substitution of equations (3.60) to (3.66) into equation (3.4) produces the following equation at H-V-L equilibrium:

$$\left[\frac{P_w^\beta \exp(\frac{v_w^\beta \left(P - P_w^\beta\right)}{RT})}{x_w^L \gamma_w^L P_w^\beta \exp(\frac{v_w^l \left(P - P_w^\beta\right)}{RT})}\right] \times ln\left[(1 + C_g^{small} f_g^V)^{-v_{small\,A,B,C}} \times (1 + C_g^{large} f_p^L)^{-v_{large1\,A,B,C}} \times \right.$$

$$\left. (1 + C_g^{large} f_p^L)^{-v_{large2\,A,B,C}}\right] = 1 \qquad (3.67)$$

v_{small} - number of small cavities

v_{large1}, v_{large2} -number of large cavities

A,B, C - formation types of either A, B or C semiclathrates.

Model Parameters

Assumptions

Vapour pressure of empty hydrate (β)

It is assumed that an increase in tetra-butyl ammonium salt concentration results in an increase in vapour pressure. This is due to the halides (Cl⁻ or F⁻) forming bonds together with the water molecules which result in the elongation of the hydrogen bonds that form the hydrate framework. Hence the vapour pressure of the empty hydrate lattice is calculated using the method of Dharawardhana et al. (1980):

$$P_w^\beta = 0.1 \exp\left(17.440 - \frac{6003.9}{T} + h + w_p\right) \tag{3.68}$$

h - adjustable parameter

w_p - weight fraction of promoter in aqueous solution.

Hydrate cavities

TBAC and TBAF form three and two types of crystal structures respectively. Table 3-4 presents the crystal structures of TBAC and TBAF. The hydrate number is the number of water molecules per molecule of tetrabutyl ammonium salt. The hydrate number is specific to each structure type. Eslamimanesh (2012) calculated the number of cavities (v_{small}, v_{large1}, v_{large2}) in a tetrabutyl ammonium salt semi-clathrate using the hydrate number of the structure (Refer to equation 3.69 and 3.70). The number of cavities per water molecule in a unit semi-clathrate is summarized in Table 3-5 and Table 3-6.

Table 3-4: Crystal structures of TBAC and TBAF (Maniko et al., 2010).

	Type A	Type B	Type C
TBAC	TBAC.24H$_2$O	TBAC.30H$_2$O	TBAC.32H$_2$O
TBAF	TBAF.28.6H$_2$O	TBAF.32.3H$_2$O	

The number of cages per for each structure type per water molecule in a unit hydrate cell is specified as follows:

$$v_{small} = \frac{4}{2 \times hydrate\ number} \tag{3.69}$$

$$v_{large} = \frac{6}{2 \times hydrate\ number} \tag{3.70}$$

Table 3-5: Number of cavities of per water molecules in a unit TBAC semi-clathrate.

	Type A	Type B	Type C
v_{small}	1/12	1/15	1/16
v_{large1}	1/8	1/10	3/32
v_{large2}	1/8	1/10	3/32

Table 3-6: Number of cavities of per water molecules in a unit TBAF semi-clathrate.

	Type A	Type B
v_{small}	3/43	6/97
v_{large1}	2/19	4/43
v_{large2}	2/19	4/43

Langmuir constants

The calculation of Langmuir constants proposed by Parrish and Prausnitz (1972) was modified to account for a semi-clathrate lattice. The equation proposed accounts for:

1. Disorders in the structures of cavities formed by Cl⁻ and F⁻ bonds to water molecules.
2. Interactions between large molecules of TBAC/TBAF with each other.

For dodecahedral cages:

$$C_j^{small} = \frac{aa_j}{T} \exp\left(\frac{bb_j}{T}\right) \tag{3.71}$$

For tetrakaidecahedra cages:

$$C_j^{large_1} = \frac{c}{T} \exp\left(\frac{d}{T}\right)(1 + e \times w_p) \tag{3.72}$$

For semi-clathrate pentakaidechedra cages:

$$C_j^{large_2} = \frac{f}{T} \exp\left(\frac{g}{T}\right)(1 + i \times w_p) \tag{3.73}$$

aa_j and bb_j = parameters recommended by Munk et al. (1988) for dodecahedral cages (Refer to Table 3-7).

c, d, e, f, g and i = adjustable parameters for tetrakaidecahedra and pentakaidecahedra cages.

Table 3-7: Parameters of Langmuir constants for a dodecahedral cage (Munk et al. 1988).

Hydrate-forming gas	aa	bb
	K.MPa⁻¹	K.MPa⁻¹
CO_2	0.0011978	2860.50

Henry's constant

The Henry's constant equation of Krichevsky and Kasarnovsky (1935) can be used to calculate the solubility of the hydrate forming gas in water (refer to equation 3.64):

$$H_{g-w} = (10^{\ A\ +\ B(T)^{-1}+\ C \times \log(T)+\ D \times T}) \times 0.1 \qquad (3.74)$$

Table 3.-8: Parameters A to D for calculation of Henry's constant (Equation 3.74).

Solute	A	B	C	D
		K	K^{-1}	K^{-1}
CO$_2$	21.622	-1499.800	-5.650	0.000206

Activity coefficient of hydrate promoter

Eslamimanesh (2012) presented the following equation for the calculation of the activity coefficient of tetrabutyl ammonium bromide (TBAB). Since thermodynamic data of TBAC and TBAF is limited, the equation may be adapted to calculate activity coefficients of TBAF and TBAF:

$$\gamma_p = -0.5057{w_p}^3 + 1.1603w_p^2 - 1.3689w_p + 0.7655 \qquad (3.75)$$

Density of hydrate promoter

The density of the hydrate promoter (TBAC/TBAF) was assumed to be analogous to the density of TBAB. The density (ρ) of the promoter (and consequently the molar volume (V_p^L)) was calculated using the TBAB density correlation recommended by Belandria (2012):

$$\rho_p = \rho_w + o_1(100w_p) + o_2(100w_p)^2 + o_3(100w_p)^3 \qquad (3.76)$$

$$o_i = q_i + r_i(T) + s_i(T)^2 \tag{3.77}$$

ρ_p = density of promoter in g/cm^3

T = temperature of liquid in K

q_i, r_i and s_i = three sets of parameters recommended by Belandria 2012 and reported are in Table 3-9.

Table 3-9: Density parameters recommended by Belandria (2012).

Constant	Value	Constant	Value	Constant	Value
q_1	-1.707 $\times 10^{-8}$	r_1	5.693 $\times 10^{-6}$	s_1	4.549 $\times 10^{-4}$
q_2	4.570 $\times 10^{-9}$	r_2	-3.099 $\times 10^{-6}$	s_2	5.304 $\times 10^{-4}$
q_3	0	r_3	4.088 $\times 10^{-8}$	s_3	-7.091 $\times 10^{-6}$

Molar volume of water

The molar volume of water (cm^3/mol) was estimated by a correlation recommended by Eslamimanesh (2012):

$$V_w^L = 5.459 / (0.30542^{\left(1+\left(1-\frac{T}{647.13}\right)\right)^{0.081}}) \tag{3.78}$$

Peng-Robinson

The critical properties and accentric factor required for the Peng-Robinson Equation of State (discussed in section 3.4) is presented in Table 3-10:

<div align="center">

Table 3-10: Critical properties and acentric factor.

</div>

Compound	Pc/MPa	T_c/K	ω
H_2O	22.064	647.13	0.3443
CO_2	7.377	304.13	0.2239

Regressed parameters

In order to optimize parameters in equation (3.68), (3.72) and (3.73), the differential evolution (DE) optimization strategy is used. The DE optimization algorithm is considered to be highly efficient in the prediction of thermodynamic model parameters. The most probable optimal parameter is obtained from the minimization of the following objective function (OF):

$$OF = \frac{100}{n} \sum_i^n \frac{|P^{exp} - P^{calc}|}{P^{exp}} \tag{3.81}$$

n - number of data points used in the optimization procedure.

i - i^{th} experimental dissociation point.

P^{exp} - experimental pressure at hydrate dissociation.

P^{calc} - calculated pressure at hydrate dissociation.

DE optimization is on a random search method and may result in negative parameters. Hence the objective function exists with the following constraints:

$$(Z - \beta) > 0 \tag{3.82}$$

$$\left(\frac{Z-(1-\sqrt{2})\beta}{Z+(1+\sqrt{2})\beta}\right) > 0 \tag{3.83}$$

Where:

$$\beta = \frac{bP}{RT} \tag{3.84}$$

Z = compressibility factor.

β = repulsive parameter of EOS.

CHAPTER FOUR
EXPERIMENTAL REVIEW

Hydrate phase equilibrium measurements require suitable equipment and techniques for moderate to high pressures. There are two main techniques for the measurement of hydrate equilibrium data i.e. visual detection and non-visual detection of hydrate formation and disappearance. The non-visual technique is the most frequently applied method by hydrate researchers. Visual detection may only be applied at temperature and pressure conditions significantly above the ice point in order to avoid confusion of ice crystal formation (Schroeter et al., 1983). There are three fundamental experimental approaches to measurement of hydrate-vapour-liquid equilibrium data in a static apparatus i.e. isothermal method, isobaric method and isochoric method. High pressure phase equilibrium measurements are difficult and protracted; hence an apparatus that can rapidly and accurately measure pressure and temperature is required. A summary of the static apparatus used for hydrate-vapour-liquid equilibrium measurements is described in this chapter. Each type has its advantages and drawbacks. The high pressure autoclave has been used in this study. The apparatus allows for visual and non-visual confirmation of gas hydrate formation and is simple to operate. A stirring mechanism is used to reduce the time of hydrate formation.

This chapter reviews the appropriate equipment designs and experimental techniques required for measurement of hydrate-vapour-liquid equilibrium data at high pressures.

4.1 Equipment Review

The experimental apparatus for the measurement of hydrate-vapour-liquid equilibrium underwent significant transformation from the nineteenth century to present. Most apparatus and experimental methods are based on either visual or non-visual hydrate detection. Visual detection methods involves the direct observation of hydrate-vapour-liquid equilibrium, however non-visual detection is the most common and accurate method of determining hydrate-vapour-liquid equilibrium (Sloan and Koh, 2008).

The characteristic features of most visual and non-visual H-V-L apparatus are the following:

1. The equilibrium cell contains a sight glass to visually validate the formation and disappearance of the hydrate.
2. The equilibrium cell is positioned in a thermostat bath. Thermocouples are located on the inside of the equilibrium cell to measure the thermal lag between the cell and thermostat bath.
3. The cell pressure is measured with Bourdon tube gauges or transducers.
4. The apparatus contains an agitation mechanism. This is done by means of either cell rotation, cell rocking, bubbling gas through cell contents or ultrasonic agitation. It is necessary to have agitation in the hydrate cell for three reasons:
   - To provide surface renewal at the gas-liquid interface.
   - To prevent water occlusion.
   - To initiate hydrate formation and prevent metastability (Sloan and Koh, 2008)

Hydrate equilibrium research commonly incorporates a non-visual apparatus and static techniques in measuring hydrate-vapour-liquid equilibrium measurements for the most accurate and precision in results.

The static technique is one of the classical procedures for measuring H-V-L equilibrium data, especially at high pressures (Oellrich, 2004). If any phase is in circulation, then this is known as a dynamic method, otherwise the method is static (Raal and Mülhlbauer (1994).Static methods are preferred over dynamic methods for the measurement of hydrate phase equilibria data.

Static analytical methods are used since it provides a truer representation of the equilibrium state and allows for accurate phase data in comparison to synthetic methods (Raal and Mülhbauer, 1994). The main advantages of static devices include:

- The simplicity of experimental procedures and experimental set-up.
- The device may be applied over a wide temperature and pressure range.
- The device is suitable for single and multi-component systems.
- Allows for easy modifications of total compositions and quantities of fluid samples.

- A small amount of material is needed ranging from 0.01 mg to a few mg (Tshibangu, 2010).
- Phase behaviour may be observed at high pressures.

This section contains a synopsis of current apparatus which have been used in literature to measure hydrate phase equilibrium. The Quartz crystal microbalance, Cailletet, Rocking cell and the high pressure auto clave cell are discussed. The high pressure autoclave cell with sapphire windows was used in this study for hydrate measurements. It is simple to operate, easily available and the observation of hydrate formation and dissociation are possible.

Types of static apparatus

Rocking Equilibrium Apparatus

Most static apparatus are based on equipment utilized by Deaton and Frost (1937) shown in Figure 4-1. The apparatus consists of a high pressure cell (typically 300 cm^3) and a sight-glass for visual observations. The high pressure cell is filled with the desired amount of water and the hydrate-forming gas may enter the cell from above the liquid water or flow through the liquid water. The cell is located in a thermostat bath. Thermocouples are positioned inside the equilibrium cell to measure the thermal lag between the cell and the thermostat bath.

The cell is rocked on a horizontal pivot through the thermostat bath to provide cell. The rate at which the cell is rocked determines the rate of mixing. Cell agitation for hydrate formation is necessary as it provides surface renewal and lack of proper agitation may lead to long nucleation periods due to metastability. However rocking of the equilibrium cell to provide agitation is unnecessarily cumbersome and may cause mechanical deterioration (Sloan and Koh, 2008).

Hydrate phase equilibrium data was obtained through visual confirmation of hydrate formation and disappearance, which is subject to a high degree of uncertainty.
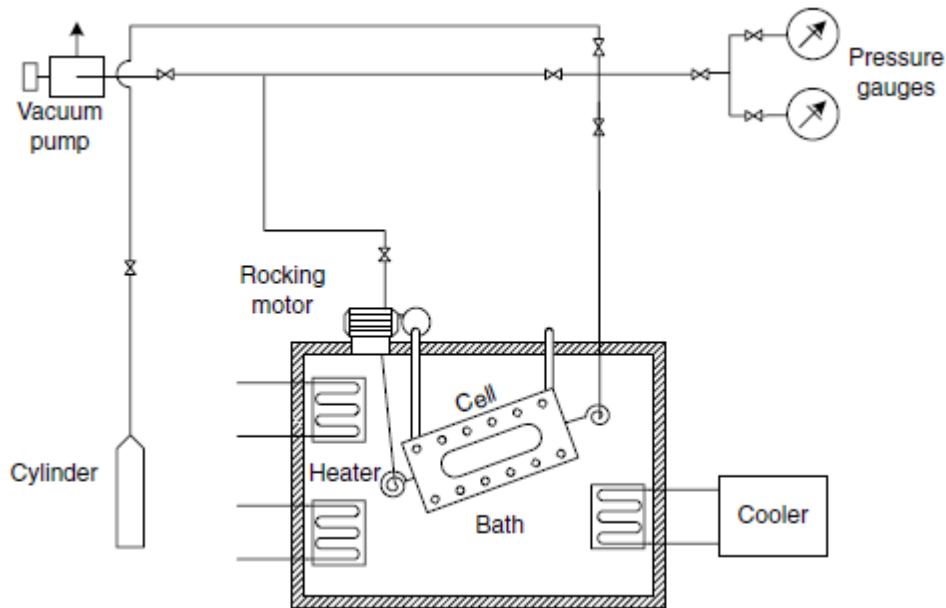
Figure 4-1: Schematic of the rocking hydrate equilibrium cell of Deaton and Frost (1937) (extracted from Sloan and Koh, 2008).

Quartz Crystal Microbalance

Recent developments in equipment design include a Quartz Crystal Microbalance (QCM) (Mohammadi et al., 2003). The apparatus consist of a quartz disk sandwiched between two electrodes. An electric current passes through the electrodes, causing the quartz crystal to oscillate at a certain resonant frequency. The frequency at which the crystal oscillates is a function of mass. Hence any change in mass will result in a change of frequency. Once the hydrates formed adhere to the surface of the quartz crystal, the hydrate formation is detected by a change in resonance frequency. Since the QCM is sensitive to very minute changes in mass, smaller samples and shorter experimental times are required for hydrate formation and hydrate phase equilibrium. A thermocouple and pressure transducer is used to measure the system temperature and pressure respectively. For viable phase measurements, the QCM apparatus requires hydrates to attach to the quartz crystal, which may not occur in all cases (Sloan and Koh, 2008).
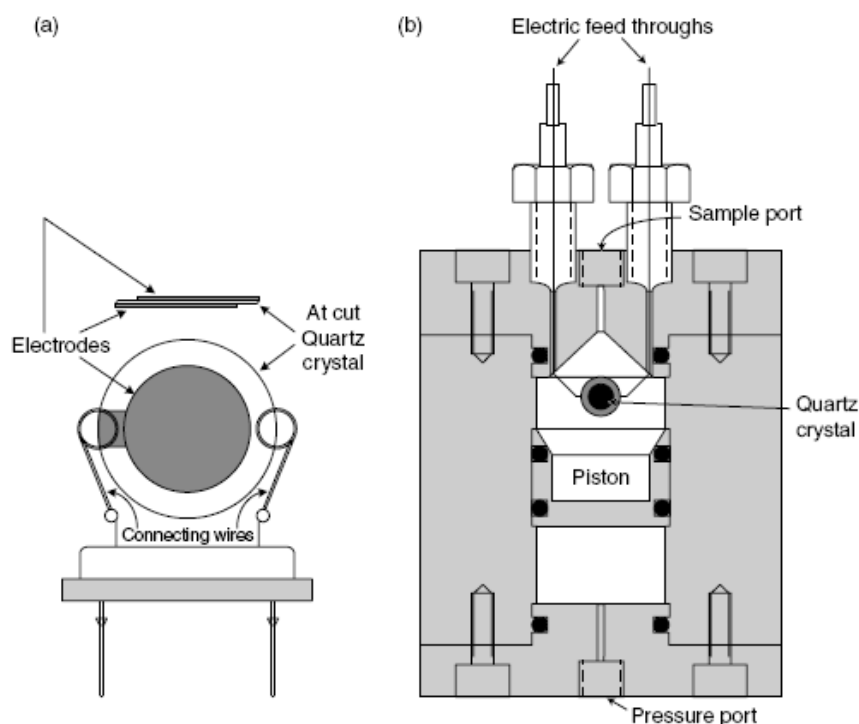
Figure 4-2: a) Quartz crystal microbalance (QCM). b) QCM mounted into a high pressure cell (Sloan and Koh (2008).

Cailletet

Sabil (2009) used a Cailletet apparatus for the measurement of H-L-V equilibria measurements. The overall schematic of the Cailletet apparatus is depicted in Figure 4-3. A sample of fixed composition is placed in the top of the Cailletet tube. The tube is then sealed by a mercury column which also acts as a part of the pressure transferring medium. Hydraulic oil is pressed into the system to generate pressure. A liquid thermostat jacket surrounding the Cailletet tube is used to keep the sample temperature constant. A pressure gauge and a platinum resistance thermometer are used to measure the system pressure and temperature respectively. The sample is cooled by the liquid jacket until hydrate formation is visually observed. The H-V-L equilibrium point is taken once the system pressure is constant and hydrate disappearance is detected. Agitation of tube contents is provided by the movement of a stainless steel ball and two moving magnets driven by an electric motor.

The formation of plugs or agglomerated hydrates may occur in the apparatus if sub-cooling is not kept to minimum and mercury used is toxic. Hydrate phase equilibrium data is obtained through visual observation of hydrate formation and disappearance, which is subject to a high degree of uncertainty. The Cailletet is constructed primarily of glass; which is not suitable for high pressures (pressure limitations are typically up to 13.8 MPa).
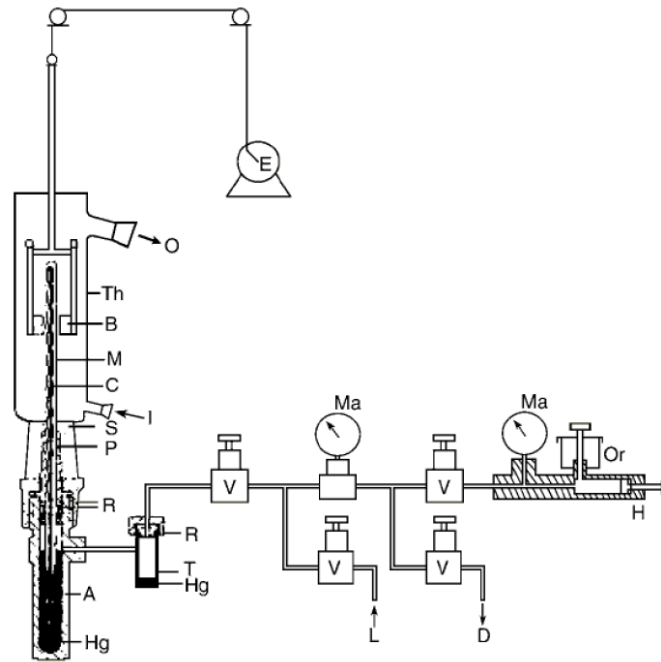
Figure 4-3: Schematic representation of Cailletet apparatus (extracted from Raeissi, 2004).

A-autoclave, B-magnets, C-Cailletet tube, D-drain, E-stirring motor, H-hydraulic pump, Hg- mercury, I-inlet tube, L-connection with dead-weight pressure gauge, M-sample of mercury, Ma-manometer, O-outlet thermostat liquid, Or-oil reservoir, P-closing plug, R-O' rings, S-silicone rubber stopper, T-mercury trap, Th-glass thermostat, V-valve

High Pressure autoclave (visual and non-visual)

The high pressure autoclave apparatus consists of a high-pressure cell (crystallizer) enclosed in a liquid bath for temperature control. The type of liquid used is dependent on the temperature range for experimentation. The crystallizer may contain a sight glass for visual confirmation of

hydrate formation and dissociation. Robinson (1993) recommended the use of sapphire glass for high pressure systems up to 20 MPa. Magnetic stirrers are placed within the cell to enhance mixing at the gas-liquid interface. A supply vessel is present to supply gas into the reactor. Temperature probes are present within the cell interior or cell wall. The temperature probe placed on the upper half of the cell measures the fluid phase, whilst the temperature probe on the lower half of the cell measures the bulk phase, since hydrate formation occurs on the bottom half of the cell. High pressure transducers monitor the system pressure.

Various authors have modified the high pressure autoclave cell, depending on the experimental method and conditions. Lee et al. (2010a) incorporated a baffle arrangement in the crystallizer in order to prevent vortex formation and to enhance mixing of the crystallizer contents. Duc et al. (2007) and Herri et al. (2007) replaced magnetic stirrers with vertical blade turbine impellers.

The high-pressure autoclave is simple to construct and operate such that it is the preferred apparatus for the measurement of high pressure H-V-L equilibria data. Table 4-1 summarises previous H-V-L high pressure autoclaves used to measure H-V-L equilibria data.

Table 4-1: A review of high pressure autoclaves used to measure of H-V-L equilibria data.

Author	Cell volume (cm^3)	P limitations (MPa)	Visual/Non-Visual
Zhang et al. (2004)	23.6	<20	Non-visual
Liu et al. (2008)	680	<20	Non-visual
Li et al. (2009)	1000	<20	Visual
Fan et al. (2009)	1000	<20	Visual
Chapoy et al. (2011)	300	< 69	Non-visual
Duc et al. (2011)	363	<10	Visual
Gholinezhad et al. (2011)	527	<10	Visual
Herri et al. (2011)	2000	<10	Visual
Meysel et al. (2011)	131	<27	Non-visual

4.2 Review of the Experimental Method

There are three fundamental experimental approaches to measure hydrate-vapour-liquid equilibrium data in a static apparatus i.e. the isothermal method, isobaric method and isochoric method. The isochoric method is most frequently adopted technique of hydrate-vapour-liquid equilibrium measurements. Unlike the isobaric and isothermal methodologies, the isochoric method requires no visual observation thus reducing the uncertainty of the equilibrium result. The isochoric technique is the method of choice for this research project.

The isothermal method:

In this constant temperature operation, the gas-liquid system is initially set at a pressure above the H-V-L equilibrium line. Gas molecules are encapsulated; forming hydrates which result in a decrease in pressure until the equilibrium line is reached. As the hydrates form, the system temperature increases. The increase in temperature is due to fluid (gas and water) molecules releasing translational energy as they are crystalizing. However this energy is transferred to the surrounding bath via convection.

Once hydrate formation is complete, the system pressure is gradually lowered to decompose the hydrates. The visual disappearance of the last hydrate crystal is interpreted as the equilibrium point. This technique involves a trial and error methodology and is time-consuming (Oellrich, 2004).

The isobaric method:

During hydrate formation, the system pressure is kept constant by the addition of gas into the cell. The system temperature is gradually decreased until hydrate formation occurs. Initial hydrate formation results in a considerable decrease in pressure. As a result, there is a significant increase in gas injected into the equilibrium cell.

Upon completion of hydrate formation, the system temperature is gradually increased to decompose gas hydrates. During heating, the system pressure is constantly maintained by the withdrawal of fluid from the equilibrium cell. Heating occurs until the visual disappearance of the last hydrate crystal, which is interpreted as the equilibrium point (Oellrich, 2004).

The isochoric method:

In contrast to the previous two techniques, this procedure requires no visual observation and as a result is a more accurate method. The isochoric method can be entirely automated to be performed overnight. Hence, in this present study, the isochoric procedure was been adopted to measure phase equilibria data of CO_2 semi-clathrates.

Figure 4-4 displays a representative pressure-temperature trace for the formation and dissociation of gas hydrates under isochoric conditions. A water-containing vessel is pressurized with gas (Point A). The temperature of the cell is then decreased, resulting in a decrease in pressure (Point A to B). The pressure reduction is due to gas contraction and an increase in gas solubility during isochoric cooling. The duration from point A to point B is known as the induction time i.e. the time elapsed until hydrates are macroscopically formed. At point B, a rapid decrease in pressure is observed, indicating gas encapsulation and hydrate formation. Point B to C is known as the hydrate growth period, where gas molecules are concentrated within hydrate cages. It is important to note that hydrate gas molecules are more closely packed than in the vapour phase (Sloan et al., 2008).

Once the hydrates are formed, the cell temperature is increased (at point C) to bring about hydrate dissociation. A rapid pressure increase (due to thermal gas expansion) indicates the commencement of hydrate dissociation. Point D is the hydrate dissociation point and indicates hydrate equilibrium. At this point the gas hydrates are completely decomposed (Sloan and Koh, 2008). If a sight glass is present, complete hydrate decomposition may be visually confirmed.

Previous hydrate research has concluded that the hydrate formation process is stochastic and therefore unpredictable. Hence the conditions at the point of hydrate formation cannot represent hydrate phase equilibrium. The hydrate formation conditions are not reproducible since these conditions are apparatus-dependent (e.g. the rate of hydrate formation is strongly dependent on the degree of agitation). Hydrate formation results in the relaxation of the metastable pressure. However the slow heating for hydrate dissociation does not result in metastability. Hence the end point of hydrate dissociation is more reproducible than point of hydrate formation. The hydrate dissociation point is used as a measurement of equilibrium in the isochoric pressure

search method since it has greater reproducibility than the hydrate formation point (Sloan and Koh, 2008).
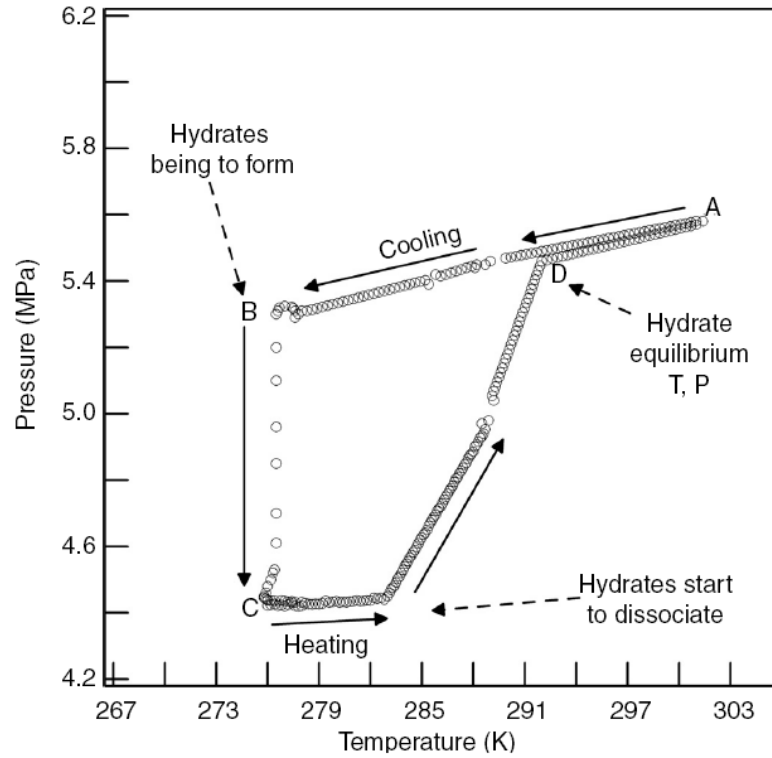
Figure 4-4: Typical pressure-temperature diagram for formation and dissociation of hydrates via isochoric pressure-search method. A-B: hydrate induction period, B-C: catastrophic growth period, D – complete hydrate dissociation (Sloan and Koh, 2008)

CHAPTER FIVE
EQUIPMENT DESCRIPTION

A static analytical apparatus was chosen for the measurement of accurate H-V-L equilibrium data. The equipment was commissioned by Tshibangu (2010) for the measurement of high pressure vapour-liquid equilibrium data of fluorochemical systems. Figure 5-1 provides a schematic diagram of the equipment layout. The apparatus consists of the following principle features:

1. A constant volume and visual equilibrium cell.
2. A withdrawal method of the liquid and vapour phases.
3. A method of agitation of cell contents.
4. Maintenance of cell temperature with a liquid bath.
5. Devices for pressure and temperature measurement.
6. A vacuum pump for degassing of the liquid phase.

Review of a high pressure experimental apparatus

The apparatus used in this study, consists of a high-pressure cell (crystallizer), enclosed in an ethylene-glycol solution bath for temperature control. Due to the low freezing point of the liquid, ethylene-glycol solution provides an ideal medium for the thermostat bath. Agitation of the cell contents is provided by a magnetic stirrer. This promotes contact between phases, enhancing conversion of water into a hydrate and shortening the hydrate formation time. The magnetic stirrer is placed within the cell to enhance mixing at the gas-liquid interface. Two platinum (Pt-100) temperature resistors are present within the cell interior to monitor the temperature of the bulk and fluid phase. The temperature probe placed in the upper flange of the cell measures the bulk phase (hydrate phase), whilst the temperature probe in the bottom flange of the cell measures the fluid phase. Pt-100 resistors provide satisfactory accuracy for a temperature range of 73.15 K to 1123.15 K (Tshibangu, 2010). WIKA P-10 pressure transducers measured the cell pressure. The accuracy of the pressure transducer is ±1.44 kPa. Since visual observation is the only direct method to confirm hydrate formation and dissociation, a sight glass is required.

A standard vacuum pump was used for the degassing of cell contents. The pump was also utilised for the removal of undesirable and low volatile compounds in the equilibrium cell. An Erlenmeyer flask was positioned on the line connecting the cell to the vacuum pump. This prevented the passage of anything that could damage of the vacuum pump, through the capture of condensable gases.

A schematic diagram illustrating the layout of the apparatus used is displayed in Figure 5.1. below. The inlet gas line and the cell drain line consisted of 1/8 inch stainless steel tubing. Valve V2 allowed for the degassing of the filling line from the gas cylinder to the equilibrium cell. The cell contents were drained by passing through valve V5.
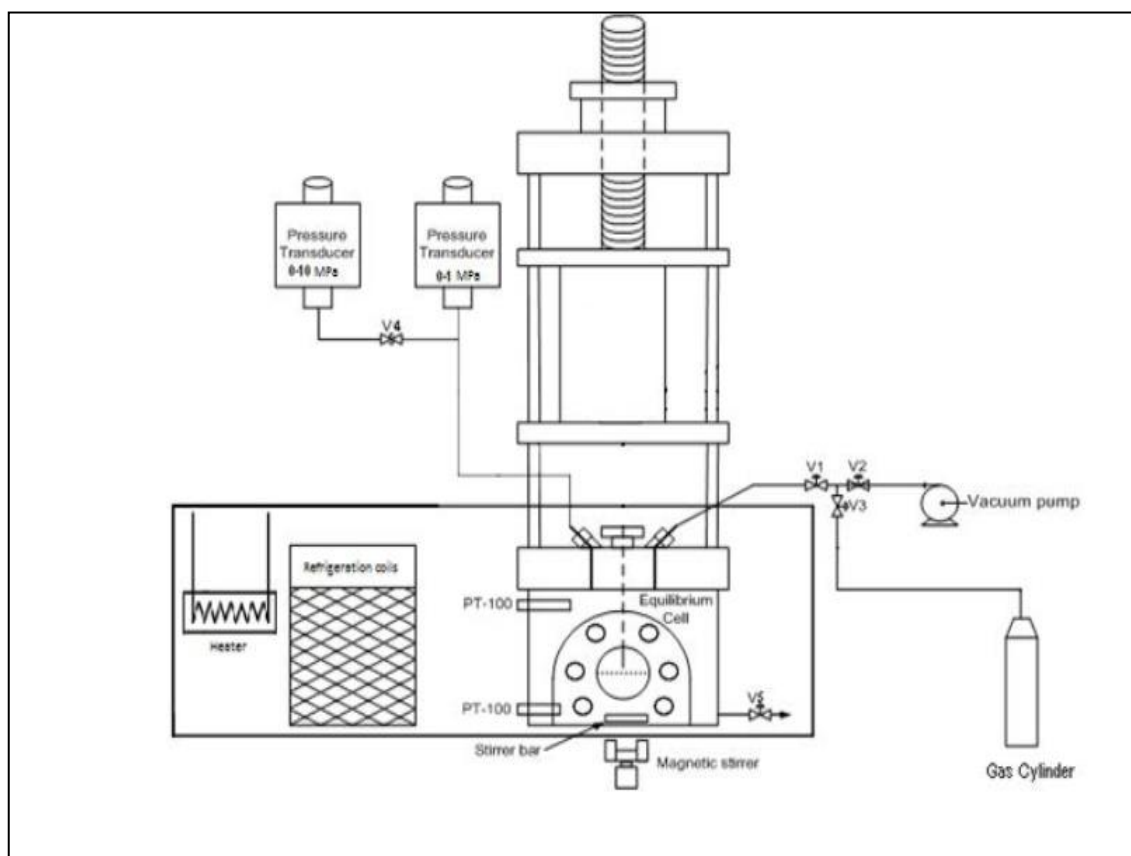
Figure 5-1: Apparatus for H-V-L equilibrium data measurements (Tshibangu, 2010).

Hydrate equilibrium cell

The equilibrium cell consists of a corrosion-resistant 316 stainless steel cylindrical cell with two 14mm thick sapphire windows designed to withstand pressures of up to 20MPa. The sapphire windows present a 22mm diameter viewing from the front and back of the cell. The windows of the cell were enclosed in a gasket material to avoid any friction between the metal and glass. Each window was bolted onto the cell by five mild steel bolts and sealed with 'O' rings. The 60 cm^3 equilibrium cell has an internal diameter of 30 mm and a height of 85 mm (Tshibangu, 2010).

Three holes, each with a diameter of 3mm, were drilled into the equilibrium cell. The first hole is positioned on the top right of the cell and allows for the discharge of fluids into and out of the cell. The second hole is positioned on the top left of the cell and allows for the contact of the cell vapour with the attached pressure transducer. The third cell hole is located at the bottom of the cell, which serves as a drainage hole, allowing for the discharge of liquid out of the equilibrium cell (Tshibangu, 2010). Figure 5-2 provides a schematic representation of the equilibrium cell.
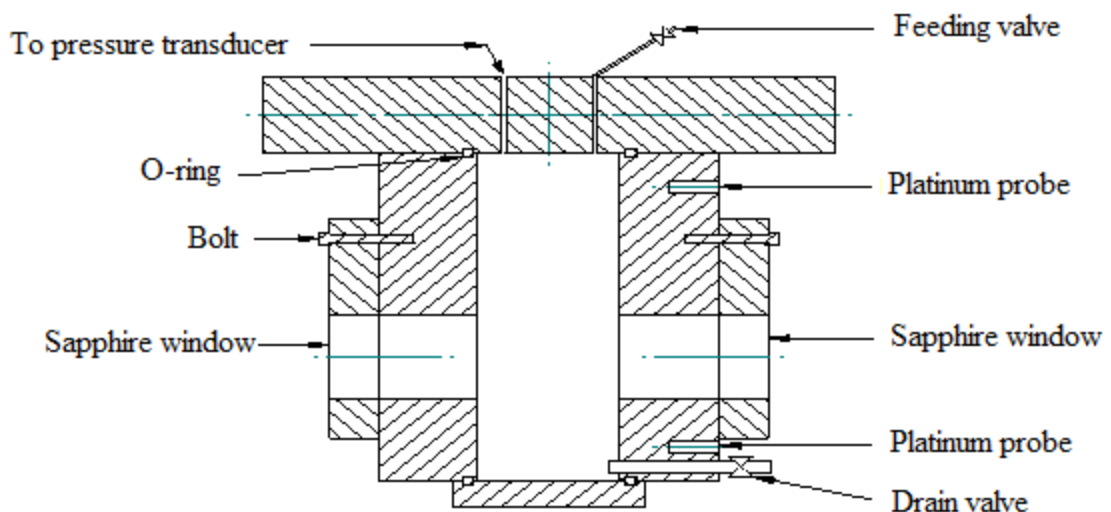
Figure 5-2: Hydrate equilibrium cell (Tshibangu, 2010).

Agitation

The agitation assembly consisted of a Heidolph Model RZR 2021 mechanical stirrer provided by Labotech to provide mechanical motion ranging from 0-800rpm. The mechanical stirrer transmitted motion to a magnet by the use of two sprockets and a roller chain (Refer to Photograph 5.-1). The sprocket sizes were a modification to the original design by Tshibangu (2010). A sprocket wheel of 25 teeth and a 9mm-pitch was directly-attached to the mechanical stirrer and a sprocket of 12 teeth and a 9mm-pitch was directly-attached to the magnet. The large-small positioning of the sprockets resulted in the magnet rotation existing at twice the speed (rpm) than that of the large sprocket (rotated by the mechanical stirrer). This modification increased the capability of the assembly to approximately 1500 rpm.

A 12mm long stirring bar coupled with a rare-earth magnet was positioned inside the equilibrium cell. Rotation of the stirrer bar was induced by the external magnet and sprocket system.

Magnetic stirrer

Mechanical stirrer shaft

Sprockets and roller chain

Stirrer assembly stand
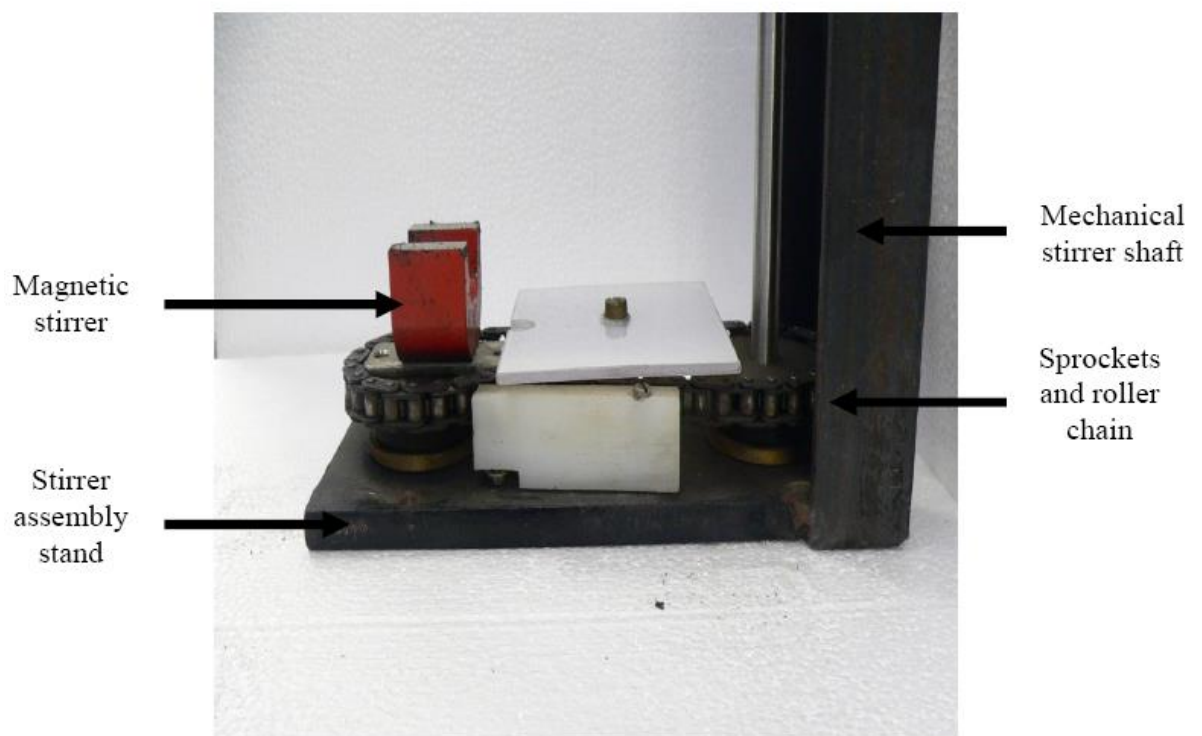
Photograph 5-1: Agitation component of apparatus. Two sprockets are connected by roller chain, which is motioned by a mechanical stirring shaft. (extracted from Tshibangu, 2010).

Sapphire window

Pt-100

Magnet stirrer

Pt-100

Drain valve
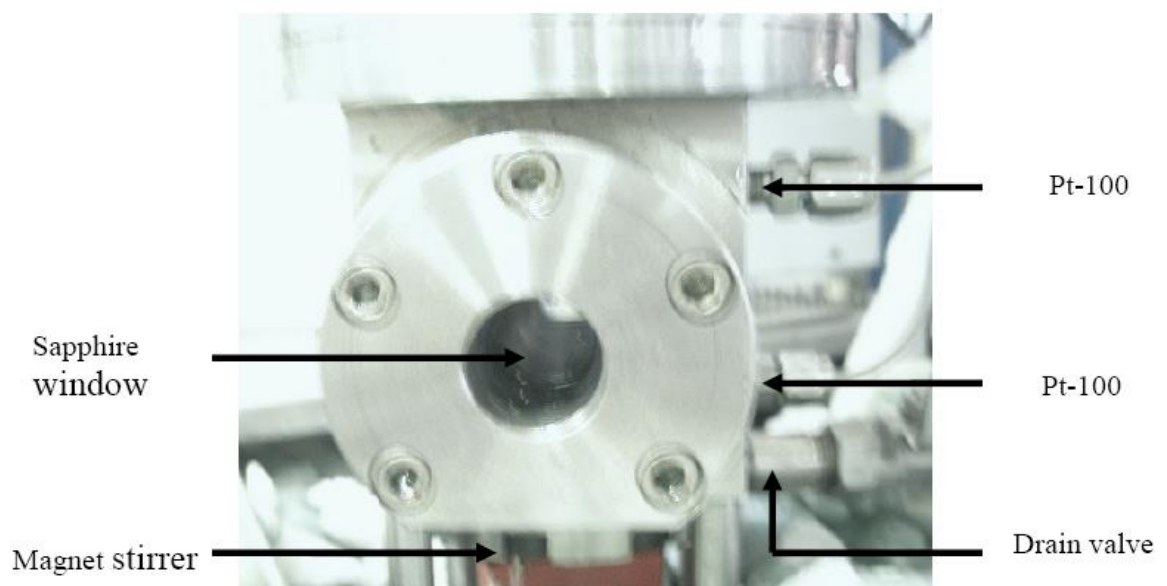
Photograph 5-2: Front view of hydrate equilibrium cell (Tshibangu, 2010).

Liquid bath

In order to maintain accurate temperature measurement of the cell contents, the hydrate equilibrium cell is submerged in a 10cm thick polycarbonate-thermostat bath. The bath is 43 cm in length, 35 cm in width, 26 cm in height and is approximately 30 litres in volume. 30 L of a 80 wt% ethylene glycol and water mixture was used as the thermo-regulating liquid since it has the ability to maintain a liquid state below the freezing point of water. The liquid was supplied by Polychem and has an operating range of 228 K (melting point at atmospheric pressure) – 397 K (boiling point at atmospheric pressure). In order to minimize heat transfer to and from the surrounding atmosphere, polystyrene insulators and aluminium foil were used to cover the liquid surface and bath walls respectively. To provide visibility of the cell contents, through the equilibrium cell sapphire window, a viewing area was created in front of the sapphire window, in the bath frame. The bath viewing area provided visual verification of hydrate formation and dissociation. The viewing area also provided visual confirmation of efficient agitation.

A programmable thermostat (Model 7312 supplied by Polyscience®) was placed in the liquid bath to provide a stable temperature profile. The unit has an operational range of 278.15 K-473.15 K. The programmable thermostat provided rapid adjustment and integration of heat by the use of an integral pump. The integral pump provided circulation of temperature-controlled fluid through the bath.

An immersion cooler supplied by Polyscience® was used to cool the bath contents. The refrigeration system was capable of cooling to a minimum temperature of 173.15 K.

Temperature Sensor

The temperature was measured using two L-shaped platinum resistance thermometers (Pt-100), supplied by WIKA. The Pt-100 probes measure temperature over a range of 73.15 K - 1073.15 K with an accuracy of ±0.06K. Each probe was fixed to the top or bottom of the equilibrium cell and corresponded to the vapour and liquid phase respectively. The bottom temperature

probe was used to report hydrate phase equilibrium measurements since hydrate form at the bottom of the equilibrium cell. Both temperature probes were connected to an Agilent data acquisition to record and present periodic temperature measurements (discussed above).

Pressure Sensor

The equilibrium cell pressure was measured by a P-10 pressure transducer, supplied by WIKA. The transducer has a pressure range of 1-10 MPa. The transducer has an accuracy of 0.05% of the full scale pressure of the instrument as stated by manufacturer. The instrument provides readings in gauge pressure. The transducer was connected to an Agilent data acquisition to record and display periodic pressure measurements of the systems.

The pressure transducer was mounted in a temperature controlled stainless steel block, above the cell, since it is highly sensitive to temperature. A heating cartridge of 7mm diameter and 40mm length was also contained within the stainless steel block. Both the heating cartridge and stainless steel block kept the transducer at a fixed temperature, since any fluctuations in the surrounding atmosphere may influence the sensitivity of the transducer and cause erroneous conditions. The transducer was maintained at 313.15 K, which was the maximum temperature that the equipment were expected to reach.

Data acquisition system

A 3947OA data acquisition switch unit (supplied Agilent Technologies) was connected to a personal computer. The data acquisition system was used to monitor and log pressure and temperature measurements during experimental runs. The Agilent Benchlink Data Logger 3 software presented real-time data of pressure and temperature.

CHAPTER SIX

MATERIALS AND EXPERIMENTAL PROCEDURE

6.1   Materials

Table 6-1: Purities and suppliers of gases used in this study.

Compound	Formula	CAS number	Purity[*] (vol%)	Supplier
Carbon dioxide	CO_2	124-38-9	>99.9%	AFROX Ltd
Ethane	C_2H_6	7727-37-9	>99.9%	AFROX Ltd
Nitrogen	N_2	7727-37-9	>99.9%	AFROX Ltd

[*]As stated by supplier

Table 6-2: Purities and suppliers of tetrabutyl ammonium salts used in this study.

Compound	Formula	CAS number	Purity[*] (vol%)	Supplier
Tetrabutyl ammonium chloride (TBAC)	$C_{16}H_{36}ClN$	22206-57-1	98%	Capital Lab Suppliers
Tetrabutyl ammonium fluoride (TBAF)	$C_{16}H_{36}FN$	37451-68-6	97%	DLD Suppliers

[*]As stated by supplier

Ultrapure water utilised in this study was supplied by the University of KwaZulu-Natal Chemistry Department with a conductivity of 18.3 Ω at 298.15 K. All chemicals were used without additional purification.

6.2 Leak test

Leak testing and detection is undertaken to ensure the apparatus operates without any leaks for accurate phase measurement. The equilibrium cell was pressurised to 0.5MPa at 278.17K. All valves were closed and the system pressure was observed for a 6 hour period at constant temperature. If any pressure fluctuations were observed the leak rate was calculated. A leak detecting fluid (SNOOP$^{®}$) was applied to all fittings and connections. The presence of foam indicated a leak and the corresponding fitting was tightened or replaced. Calibrations commenced once the leak rate per hour was below the uncertainty of the pressure measurement.

6.3 Pressure and temperature sensor calibration

Pressure calibration

The transducer was calibrated against a CPT 6000 standard pressure transducer (supplied by WIKA). The standard transducer has an operating range of 0-25000 kPa and an accuracy of ±1.44 kPa. Both transducers were connected to the equilibrium cell and pressure measurements were taken at specific stabilized pressures, for a range of 0-5000 kPa. Multiple measurements were recorded for repeatability and for the assessment of hysteresis. A constant temperature was maintained throughout the calibration procedure. The equilibrium cell was controlled at 290.15 K and the pressure transducer was housed at 313.15 K. The actual pressure (measured by the standard pressure transducer) was plotted against the display pressure (measured by the P10 pressure transducer) and a linear response was observed (Figure 6-1). The uncertainty of the calibration correlation was estimated to be ±0.87 kPa.
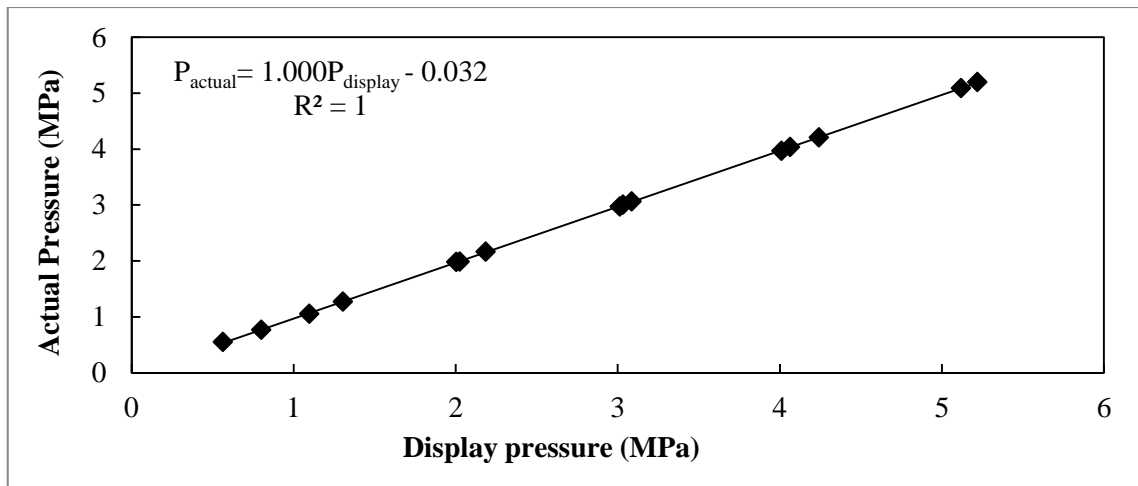
Figure 6-1: Pressure transducer calibration for the P-10 high pressure transducer (pressure range of 0-25 MPa).
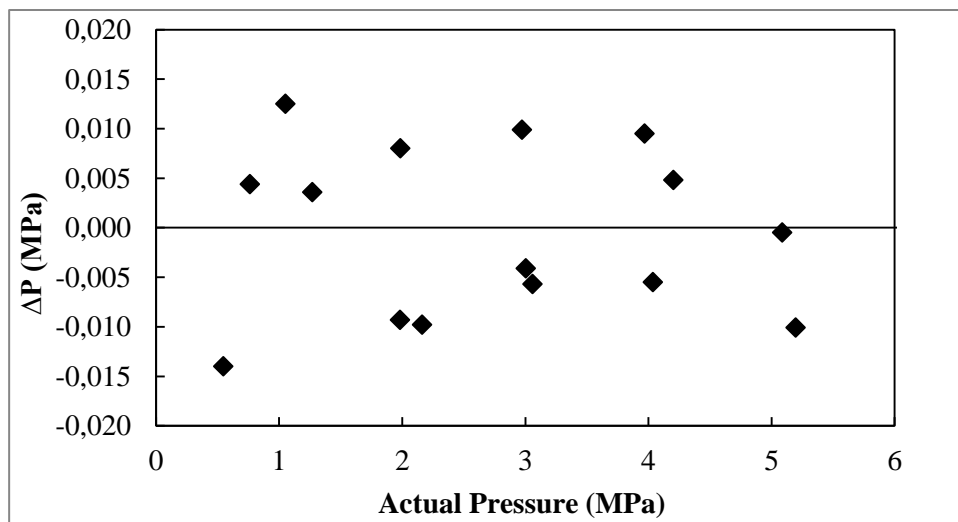
Figure 6-2: Deviation in P10 pressure transducer from standard pressure transducer.

Temperature calibration

The Pt-100 temperature probes were calibrated against a standard 100Ω platinum resistance using a processor calibrator CTH 6500, which is supplied by WIKA and has an accuracy of 0.06 K. All probes were immersed in a silicon oil bath at approximately equal depths. The liquid bath was fixed to a specific temperature and maintained for 45 minutes to allow ensure uniform temperature within the bath. The probes were calibrated over a range of 263.15 K – 293.15 K. Temperature measurements were recorded by all three probes. Multiple measurements were taken to test repeatability and the effects of hysteresis. The actual temperature (measured by the CTH 6500) was plotted against the display temperature (measured by the Pt-100 probes) and a linear relationship was observed (Figure 6-3 and Figure 6-5). The uncertainty of the bottom probe and top probe calibration correlation was estimated to be 0.03 K and 0.05 K respectively.

$$T_{actual} = 0.999 T_{display} - 0.8823$$
$$R^2 = 1$$
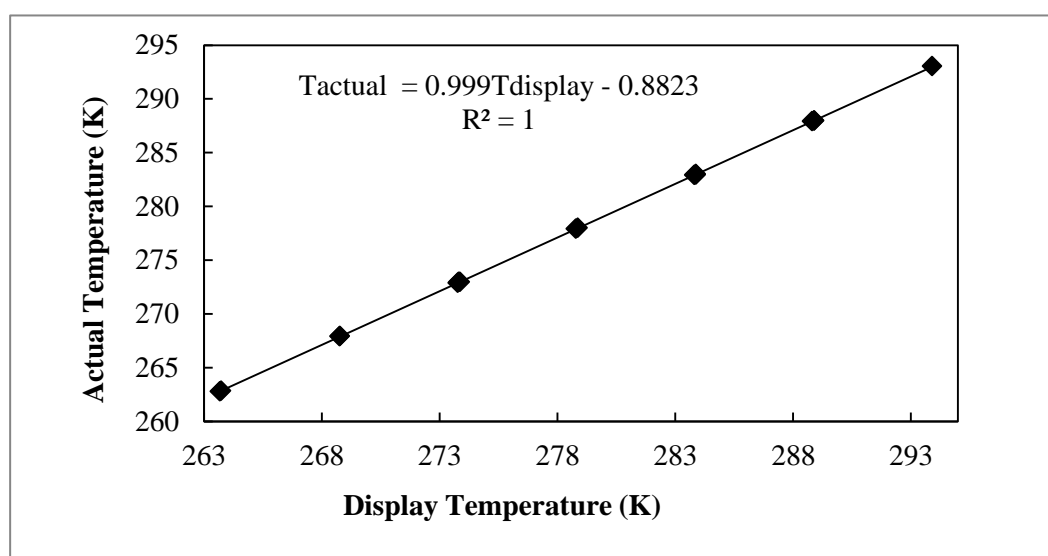
Figure 6-3: Plot of the temperature sensor (Top probe) calibration for the high pressure static apparatus
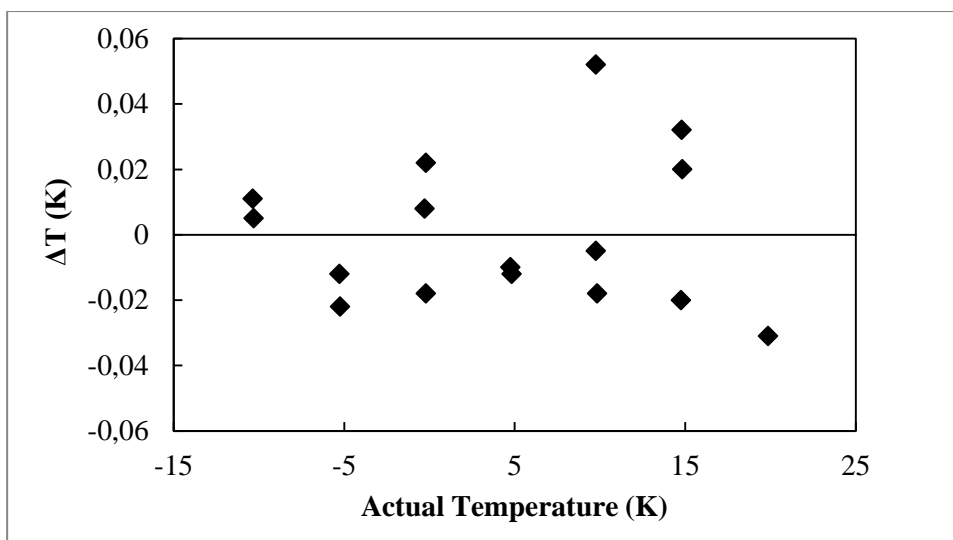
Figure 6-4: Temperature deviation between top probe and CTH 6500

$$T_{actual} = 0.9935T_{display} - 0.4589$$
$$R^2 = 1$$
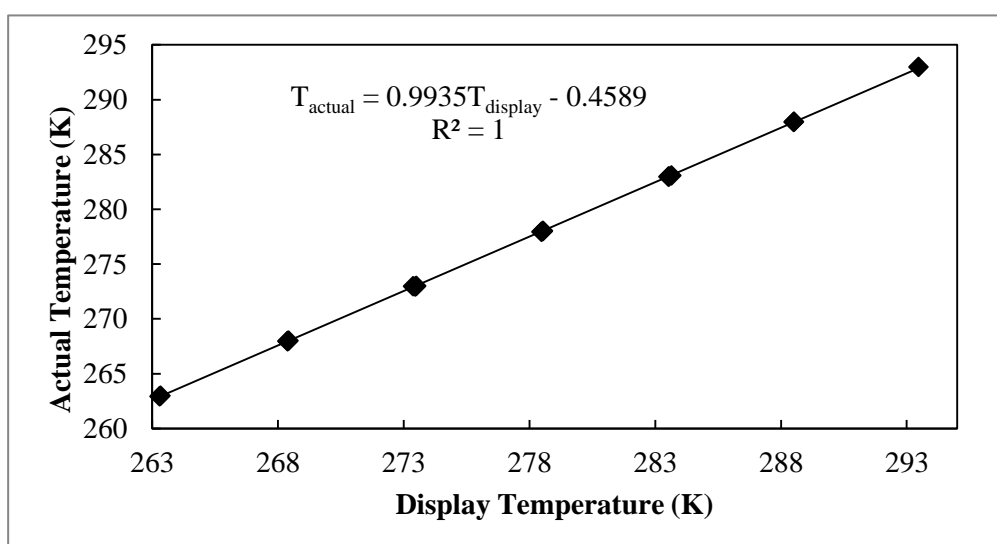
Figure 6-5: Plot of the temperature sensor (Bottom probe) calibration for the high pressure static apparatus.
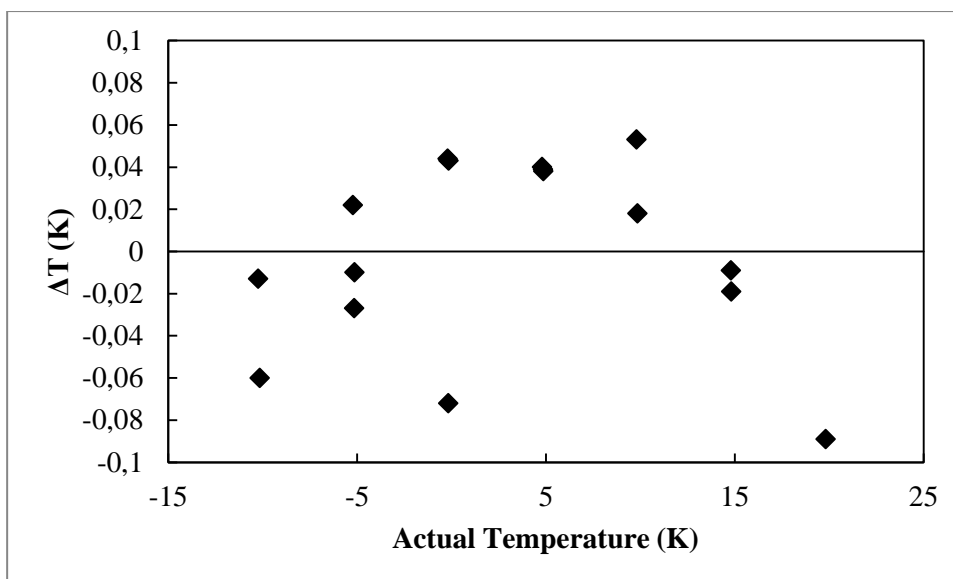
Figure 6-6: Temperature deviation between bottom probe and CTH 6500.

6.4 Vapour pressure measurements

The vapour pressure of carbon dioxide and ethane were measured to verify pressure and temperature calibrations. The temperature of a pressurized equilibrium cell was varied and the resulting system pressure was recorded.

To ensure purity of the gas studied, the line connecting the equilibrium cell to the gas cylinder was evacuated to remove any trapped air or gas present in the line. The equilibrium cell was pressurized with the studied gas and the desired system temperature was set on the programmable thermostat. The system temperature was held for 1 hour or until the system pressure stabilized within 1kPa. The pressure of the cell was captured every 40 seconds and the average data of ten readings was recorded. To eliminate the effects of hysteresis, the vapour pressure readings were repeated from a low system temperature to a high system temperature and vice versa. Vapour pressure measurements for carbon dioxide and ethane were recorded for temperatures ranging from (268.23 – 288.20) K and (262.46 – 288.41) K respectively.

6.5 Hydrate measurements

Cell preparation

The equilibrium cell was cleaned prior to every experimental run with the aim to remove any trace of impurities. Ethanol (a low-volatile compound) was charged into the cell at low agitation for 1 hour and removed. This process was repeated 4 – 6 times. The equilibrium cell was flushed with N_2 at 3 MPa to remove any remaining water droplets or ethanol. This was repeated twice.

The cell was evacuated for 6 hours using a standard vacuum pump. This ensured the absence of air and impurities that could affect experimental results. After the equilibrium cell was flushed three times with the experimental gas, experimental measurements were conducted.

Sample preparation and degassing

The experimental tetrabutyl ammonium salt was weighed on a mass balance with and uncertainty of ±0.001 g. The tetrabutyl ammonium salt was added to 100ml of double-distilled and deionised water from Direct-Q5 Ultrapure Water Systems (Millipore^{TM}). The solution was stirred for 20 minutes to ensure appropriate dissociation of the tetrabutyl ammonium salt and a constant concentration profile throughout the solution. The average uncertainty of the mole fraction was assumed to be less than 0.01 as suggested by Eslamimanesh (2012).

The tetrabutyl ammonium salt solution was degassed prior to experimental procedures in order to eliminate the presence of air. A significant presence of air may hinder the purity of the system gas and hinder the purity of the gas hydrate formed. The solution was degassed in a vacuum distillation unit at room temperature and pressure of 11.325 kPa. Vacuum distillation commenced for 1 hour and slow agitation was maintained.

Density measurements

Density measurements of the tetrabutyl ammonium salts were recorded after degassing of the sample, to verify that no change in liquid property and composition had occured. An Anton Paar vibrating-tube digital densimeter (model DMA 5000) was used to measure the density of the tetrabutyl ammonium salt solutions. The densimeter has an accuracy of $\pm 10^{-5}$ g/cm^3 and ± 0.01 K. Density measurements are based on the oscillation period of the vibrating U-shaped hollow tube (packed with the sample).

A density calibration curve of TBAC and TBAF was generated at 295.15 K and 303.15 K respectively. The TBAF density measurements were performed at 303.15 K due to the high viscosity and difficult fluidity of TBAF solutions at room temperature. The density calibration curve was generated by measuring the density of TBAC and TBAF solutions at various mass fractions (ranging from 0 – 0.3). All solutions were formulated using double-distilled and deionised water from Direct-Q5 Ultrapure Water Systems (Millipore^{TM}) and research grade materials described in Table 6-2.

The samples were charged into the densimeter, using a syringe, to avoid introduction of air bubbles. All density measurements were recorded at thermal equilibrium. The U-shaped hollow tube was cleaned with acetone and dried after each density measurement. All density measurements were performed three times and the average value is reported.
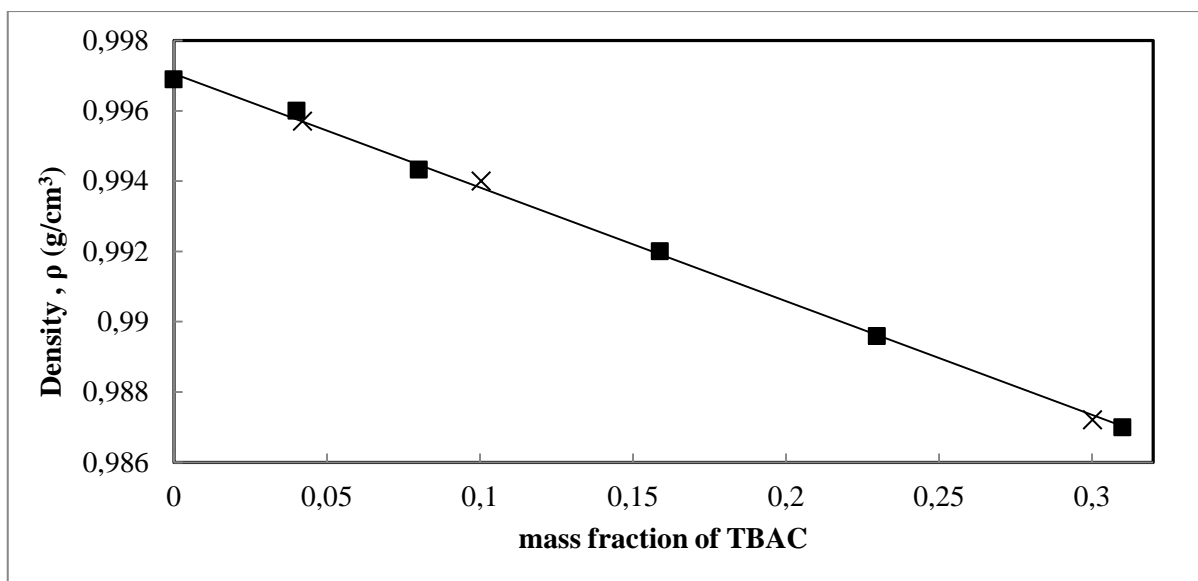
Figure 6-7: Density calibration curve of H_2O + TBAC (Tetrabutyl ammonium chloride) solution at 273.15K. ■, measured density of TBAC solution before degassing; ✖ , measured density after sample degassing.
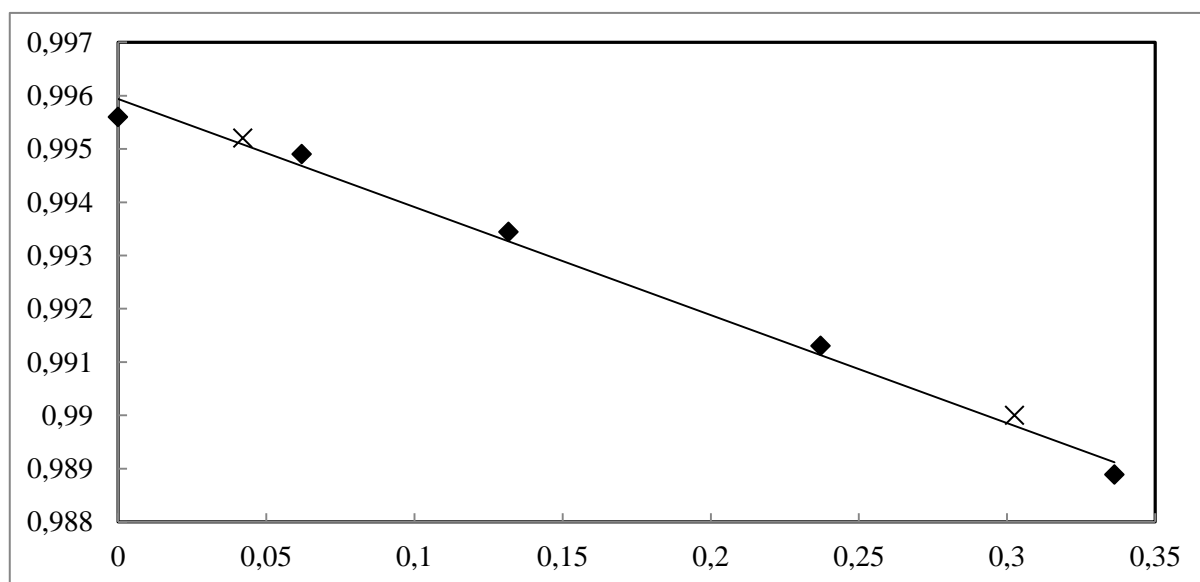
Figure 6-8: Density calibration curve of H_2O + TBAF (Tetrabutyl ammonium fluoride) solution at 273.15K. ■, measured density of TBAF solution before degassing; ✖ , measured density after sample degassing.

H-V-L E equilibrium phase measurements

An isochoric, pressure-search method (as described by Sloan et al (2008) and Sabil (2009)) was used to measure hydrate-vapour-liquid equilibrium phase data. Before starting the experiment, the equilibrium cell and the inlet line was evacuated to remove any presence of air. 21ml of the degassed tetrabutyl ammonium salt solution was drawn into the cell under the vacuum. The initial system temperature was set to 10 K above the expected hydrate formation temperature. CO_2 gas was supplied into the cell, through a pressure-regulating valve, until the desired operative pressure was reached. Once the pressure and temperature were stabilized, the pressure-regulating valve was closed and the agitation system was started at approximately 1300rpm. The equilibrium cell was evacuated and purged with CO_2 4 to 5 times to remove any presence of air before charging the cell with CO_2 to the desired operating pressure.

The programmable thermostat, immersion cooler and liquid bath were used to cool the equilibrium cell to a temperature of 273.65 K, at a constant rate of 1.2 K/h. This temperature was low enough to permit the formation of CO_2 hydrates but high enough to prevent the formation of ice.

The data acquisition system was used to continuously observe and record pressure and temperature measurements throughout the cooling process. During isochoric cooling, a steady decrease of pressure was observed. Hence a corresponding "cooling curve" was generated (Refer to Figure 6-10). Initial formation of hydrates was identified by a sudden drop in pressure (due to the encapsulation of carbon dioxide). Due to the constant cooling rate, initial hydrate formation was noted by an abrupt change in gradient on the cooling curve (Refer to Figure 6-10). Once isochoric cooling was completed, the system was held at 273.65 K for 1 hour to eliminate metastability.

After the completion of CO_2 hydrate formation, the agitation was switched off and the system was heated to dissociate the CO_2 hydrates. Hydrate heating occurred in two stages:

1. Fasting heating to the hydrate formation temperature.
2. Slow heating to the hydrate dissociation temperature at a rate of 1 K/h.

An abrupt increase in pressure during isochoric heating marked the start of the dissociation process. The corresponding pressure-temperature curve (heating curve) generated is presented in Figure 6-9. The data acquisition system was used to continuously observe and record pressure and temperature measurements. The rate of isochoric heating was decreased as the heating curve approached the cooling curve. The complete decomposition of hydrates (equilibrium point) was noted by a decrease in the pressure-temperature gradient (refer to Figure 6-10). Heating was continued for (3-6) K above the dissociation temperature.
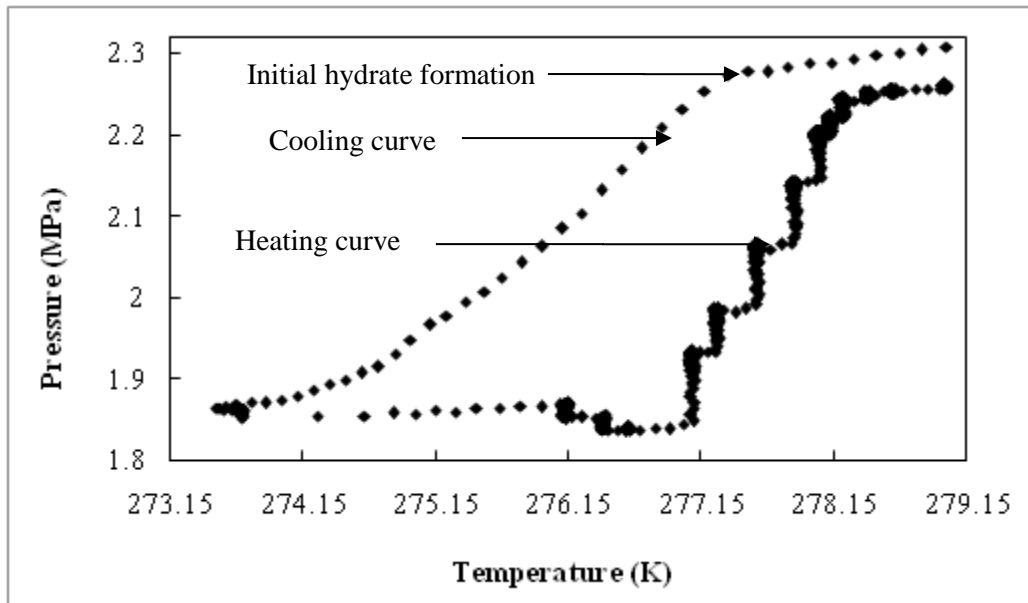
Figure 6-9: Heating and cooling curves for CO_2 + H_2O.
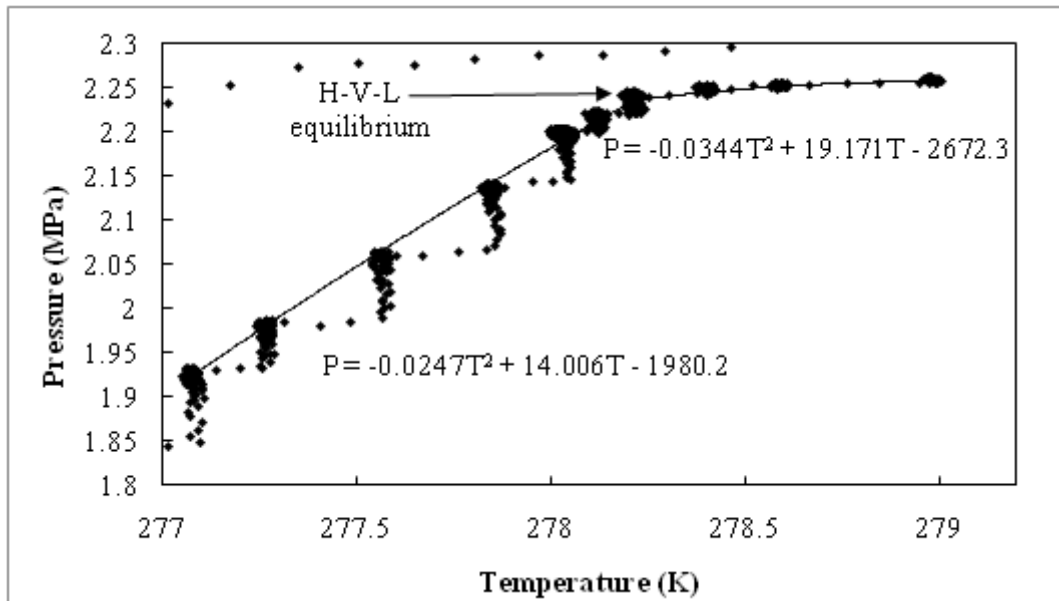
Figure 6-10: Intersection of two polynomials for determination of the hydrate equilibrium point.

To reduce the error in determining the dissociation point, using the graphical method, polynomial curves were fitted to the pressure gradients before and after the hydrate dissociation point (refer to Figure 6-10). The mathematical intersection of the two polynomials was recorded as the hydrate dissociation/ hydrate equilibrium point. Prior to the equilibrium point, a large increase in pressure was observed during heating (refer to the steep polynomial in Figure 6-10). This was due to hydrate decomposition and the release of entrapped CO_2 gas. Subsequent to the hydrate equilibrium point, a minor increase in pressure was observed. This minor increase was due to vapour pressure changes.

Analysis of measurement uncertainty

Uncertainty is a parameter associated with the result of measurement that characterizes the dispersion of the reported value. Uncertainty is attributed to the instrument of measure and may be numerically estimated by statistical methods. The reported measured values are the best estimate of the value and all components of uncertainty contribute to the dispersion (Chirico et al., 2003).

Uncertainty of the measurement values were estimated according to the NIST (National Institute of Standards and Technology) Guidelines (Taylor and Kuyatt, 2004):

$$U_c(x) = \pm\sqrt{\sum_i u_i(x)^2} \qquad (6.1)$$

$U_c(x)$ - combined standard uncertainty

Uncertainty of the pressure measurements include:

1. $U_{correlation}(P)$ = uncertainty of calibration correlation.
2. $U_{instrument}(P)$ = uncertainty of manufacturer's calibration.

Uncertainty of the temperature measurements include:

1. $U_{correlation}(T)$ = uncertainty of calibration correlation.
2. $U_{instrument}(T)$ = uncertainty of manufacturer's calibration.
3. $U_{procedure}(T)$ = uncertainty in graphical estimation of hydrate equilibrium data.

Hence:

$$U_c(T) = \pm\sqrt{U_{correlation}(T)^2 + U_{instrument}(T)^2} \qquad (6.2)$$

$$U_c(T) = \pm\sqrt{U_{correlation}(T)^2 + U_{instrument}(T)^2 + U_{procedure}(T)^2} \quad 6.2.1.3$$

A rectangular distribution was designated for statistical errors:

$$U_{correlation}(x) = \frac{b}{\sqrt{3}} \qquad 6.2.1.4$$

$$U_{insturment}(x) = \frac{b}{\sqrt{3}} \qquad 6.2.1.5$$

Where

b = difference between measured value and true value.

CHAPTER SEVEN
RESULTS AND DISCUSSION

7.1 Experimental Apparatus

Heat gain and heat loss due to the environment may result in the fluctuation of temperature and pressure within the equilibrium cell. This may result in significant uncertainty in the equilibrium data measured. Heat gain from the environment was reduced by the use of insulation around the liquid bath and the use polystyrene material on the liquid surface of the bath. Fouling and accumulated dirt was regularly removed from the liquid bath to maintain the stability of temperature and appropriate heat transfer of the liquid bath. The effects of the fluctuating ambient temperature influences were prevented by the use a heating block on the pressure transducer. The heating block kept the pressure transducer at a fixed temperature of 313.15 K to prevent erroneous pressure readings. To preserve stable system conditions and reduce uncertainty of temperature and pressure fluctuations, fouling and accumulated dirt was regularly removed from liquid bath.

The isochoric pressure-search method (as described in chapter 6.5.) was used for the measurement of hydrate-vapour-liquid equilibrium data. The graphical isochoric method requires the decrease of the system temperature at a constant rate in order to accurately determine the hydrate formation. The use some of ionic liquids, i.e. TBAC and TBAF as promoters, results in the reduction of CO_2 solubility in water. Lower gas solubility results in a lagging gas hydrate formation rate due to the deceleration of the kinetic rate. Hence this study required a lengthened period of time, for the decrease of system temperature at a constant rate, for hydrate formation to occur. A programmable heater was used to decrease the system temperature at constant rate within a specified period of time.

Two platinum resistance thermometer (Pt-100) probes were placed at the top and bottom of the equilibrium cell (Refer to Figure 5.1.1). The temperature measurements of two probes presented an inconsiderable deviation (0.25 K) in comparison to each other. However to present the most precise temperature data, the bottom probe was used for the measurement of temperature at gas hydrate formation since it is positioned closest to the hydrate crystal.

7.2　Vapour pressure measurements

Verification of sensor calibration is important in order to ensure the accurate and precise measurement of future systems. Vapour pressure measurements were performed for two different pure components, carbon dioxide and ethane, to verify pressure and temperature calibrations. The vapour pressure experimental data are shown in Tables 7.1 and 7.2 and are graphically represented in Figures 7-1 and 7-2. The experimentally measured vapour pressure data were compared to the literature data from the NIST (National Institute of Standards and Technology) Source Database and those predicted by the Ambrose (1986) correlation. To eliminate the effects of hysteresis, the vapour pressure readings were repeated from a low system temperature to a high system temperature and vice versa.

The Ambrose (1986) correlation is presented below:

$$\ln(P_{vp}) = a\tau + b\tau^{1.5} + c\tau^{2.5} \qquad (7.1)$$

P_{vp}- Vapour Pressure

a, b, c - component-specific parameters provided in Poling et al. (2001)

$\tau = 1 - \dfrac{T}{Tc}$

Table.7.1: Comparison between the experimental and literature vapour pressure data of carbon dioxide (CO_2).

This Work		NIST	Ambrose (1986)
T_{exp}	P_{exp}	ΔP	ΔP
K	kPa	kPa	kPa
268.23	3052.64	0.63	1.34
271.23	3298.18	5.44	3.26
273.24	3469.89	8.53	6.23
278.23	4021.91	8.58	11.19
283.21	4502.15	4.34	1.44
288.20	5104.32	0.40	2.79

$\Delta P = \left| P_{exp} - P_{literature} \right|$

Table.7.2: Comparison between the experimental and literature vapour pressure data of ethane.

This Work		NIST	Ambrose (1986)
T_{exp}	P_{exp}	ΔP	ΔP
K	kPa	kPa	kPa
262.46	1834.94	4.48	4.08
268.13	2111.31	1.60	1.06
273.13	2386.04	3.03	1.70
278.17	2696.37	1.24	0.86
283.18	3022.01	2.50	0.34
288.41	3408.09	1.52	5.10
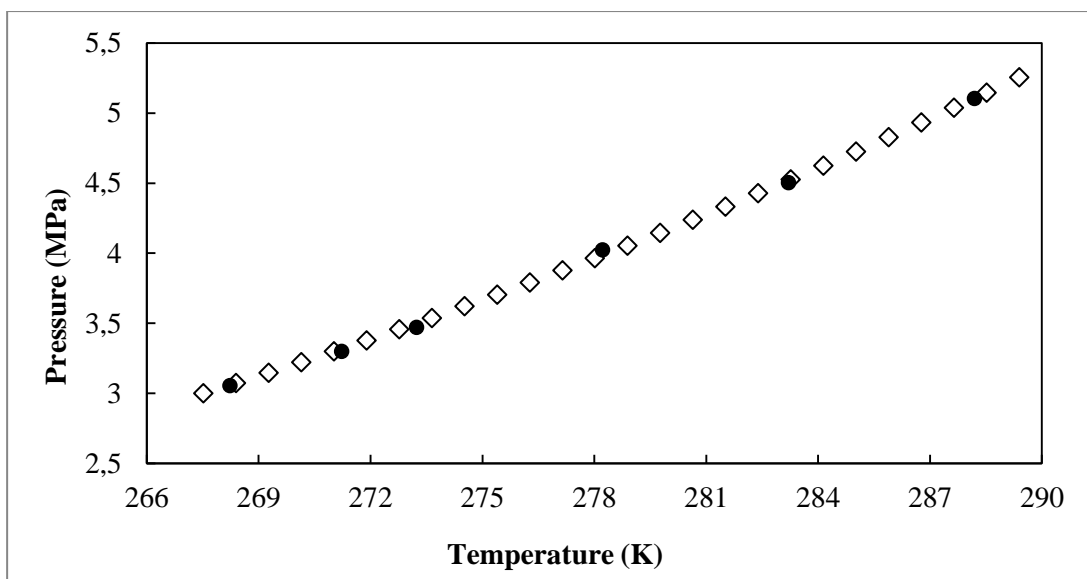
Figure 7-1: Vapour pressure data of carbon dioxide (CO_2). ●, measured; ◇, NIST Source Database
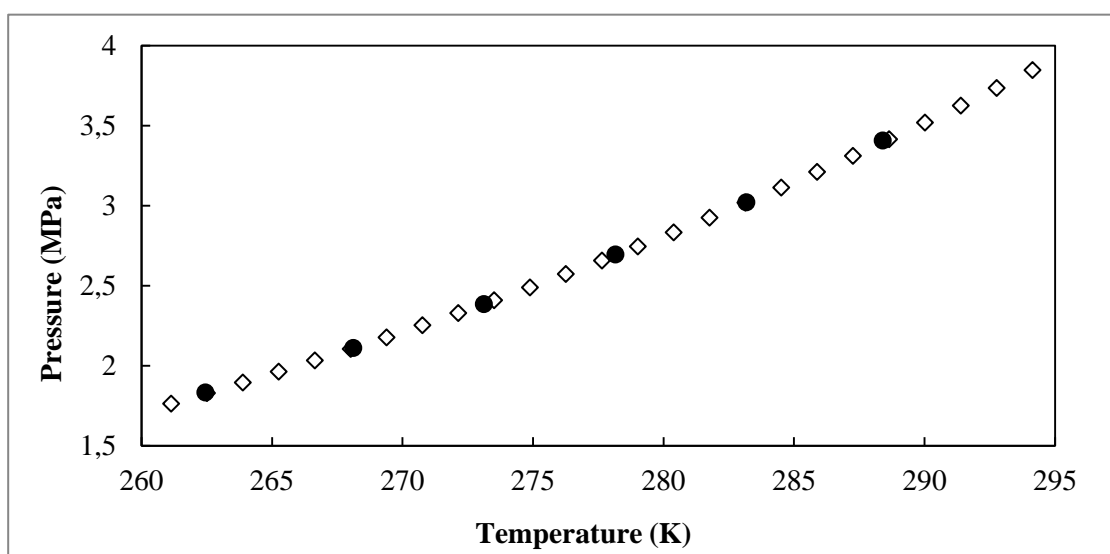
Figure 7-2: Vapour pressure data of ethane. ●, measured; ◇, NIST Source Database

Vapour pressure measurements were performed within the temperature range of the Ambrose (1986) correlation i.e. <305.33 K for ethane due to its relatively low critical temperature. To ensure the purity of the gas, the equilibrium cell was flushed with the gas and evacuated to eliminate the presence of air prior to vapour pressure measurements.

Table 7.1 and Table 7.2 show a comparison between the experimentally-measured and literature vapour pressure data. Good agreement between the literature and experimental data is observed. The maximum deviation of the experimental vapour pressure data from literature was 0.81% for CO_2 and 0.74% for ethane. Gas impurity and contamination, instrument uncertainty and uncertainty in the calibration correlation may account for the modest deviation of the experimental data from literature. Due to the acceptable agreement between the experimentally-measured and literature vapour pressure, the pressure and temperature calibrations were reputed viable. The verification of the calibrations guaranteed that future pressure and temperature measurements were stable and regular. Hence the equipment was suitable for the accurate measurement of temperature and pressure.

7.3 Experimental procedure

To prevent the contamination of the investigated systems, the equilibrium cell was cleaned with ethanol before every experiment. Ethanol was charged into the cell under a low agitation for 1 hour and removed. The cleansing process was performed four to six times for thorough removal of contaminates.   The density of the ethanol was checked after the last two removals to ensure that only pure ethanol was extracted and no contaminates remained. The equilibrium cell was then evacuated for 12 hours at 303.15 K to remove any remaining ethanol. Pressurized nitrogen was used to flush the cell and to further remove traces of residual ethanol.

Leaks are a common calamity in high pressure vessels. A leak test was performed with high pressure nitrogen as described in Chapter 6.2. If a leak was observed by a noticeable pressure drop, a leak detector was employed to locate any present leaks surrounding the equilibrium cell and gas lines.

Prior to hydrate phase equilibria measurements, the equilibrium cell was flushed with CO_2 numerous times to eliminate any presence of air. Hydrate phase equilibrium data were measured for test systems $CO_2 + H_2O$, $CO_2 + H_2O + $ TBAC (4 wt%) and $CO_2 + H_2O + $ TBAF (4 wt%). All measured data were in a good agreement with literature data, verifying that no contaminates, leaks or air were present in the high pressure equipment.

The tetrabutyl ammonium salt solution was degassed (as described in Chapter 6.5) to eliminate the presence of air. The degassing procedure was intended to eliminate and purge off the presence air from the solution. This study investigates the hydrate phase equilibrium conditions of CO_2-forming hydrates and any air present may be encapsulated by the hydrate formed. This could result in inaccurate phase equilibrium data.

The isochoric pressure-search method was also verified by the visual confirmation of hydrates through the sapphire windows. For proper validation, the equilibrium cell was drained and refilled with the same system to measure additional phase data points.

Hydrate phase equilibria data were measured using the isochoric pressure-search method as described in Chapter 6.5. Figure 6-10 provides a graphical representation of the method. The graphical method was verified through visual observation of the hydrate crystal. Approximately 35% (by volume) of the cell was loaded with liquid solution. This liquid phase consisted of either pure water, TBAC solution or TBAF solution. The key parameters of the hydrate formation rate are a) the type of hydrate former/gas composition b) agitation efficiency c) volume of H_2O. The use of a large amount of water used will result in an extended induction time i.e. a substantial amount of time will be needed for the gas hydrate to form. A little amount of water used will result in less gas encapsulation and the resultant pressure drop will be too small to be seen graphically and hydrate formation cannot be observed. Hence an optimum amount of solution was required to provide significant encapsulation of gas at an optimum time. Initially 10% and 15% (by volume) of the equilibrium cell was filled with tetrabutyl ammonium salt solution. However no change in gradient was observed after isochoric cooling. A significant change of gradient was noted when 35% (by cell volume) of tetrabutyl ammonium solution was utilized. The liquid cell volume was maintained below 50% to ensure efficient heat transfer from the cooled cell walls during isochoric cooling.

The degree of subcooling was used as the driving force of hydrate formation. Isochoric cooling started from a temperature above the hydrate formation region. A minimum subcooling driving force of 10 K was employed in each experiment i.e. the system was set to a temperature of at least 10 K above the expected hydrate formation temperature. If hydrate formation was not observed, isochoric cooling was restarted at a higher temperature to increase the subcooling driving force. The initial pressure was set to approximately 20 kPa above the desired equilibrium pressure. To prevent the formation of ice during cooling, the system was cooled to

temperatures not lower than 273.65 K (the measured temperature remained slightly above the freezing point of water).

During the cooling process, a constant decrease in pressure is noted, this is due to the partial dissolution of gas into the liquid phase. A change in gradient (indicating the commencement of hydrate formation) was noticed within a time frame of 0.5 hours, for all systems not containing of a tetrabutyl ammonium salt. However, a change in gradient was noticed within a time frame of 24 hours, for all systems consisting of the tetrabutyl ammonium salt. The cooling rate for the $CO_2 + H_2O$ system was 6.2 K/h and 1.2 K/h for $CO_2 + H_2O$ + TBAC/F systems. All systems investigated were cooled at a constant cooling rate. An inconsistent cooling rate will result in a change in gradient and will hinder the graphical observation of hydrate formation. Once the cooling stage was completed, the temperature was held for 20 minutes to exclude the metastability and complete the hydrate formation.

The rate of hydrate formation strongly depends on the degree of agitation. Robust agitation results in the rapid dispersion of CO_2 throughout the equilibrium cell as well the distortion of gas bubbles to increase system surface area.

In order to attain the most advantageous hydrate formation rate, the effects of the magnetic stirrer speed on the rate of hydrate formation was investigated. A $CO_2 + H_2O$ system at 1.84 MPa was cooled from 283.65 K to 273.65 K at various stirrer speeds ranging from 395.43 rpm to 1530 rpm. The time and temperature at hydrate formation was recorded for each run. The hydrate formation data is graphically represented in Figure 7-3. Several experimental runs were repeated to verify the accuracy of the hydrate formation data. Since rate of hydrate formation is apparatus-dependent, the data represented in Figure 7-3 will change for another unit. The hydrate formation time is reliant on the degree of agitation, surface area of the system and the rate of heat and mass transfer. Hence the hydrate formation point will vary for different equipment designs. Hydrate formation does not occur with stirrer speeds of 395.43 rpm to 876.73 rpm since the agitation cannot provide enough contact area between the liquid phase and the gas phase to enhance crystal growth. The optimum agitation speed of 1272.73 rpm was determined by observing the highest hydrate formation temperature (275.65K) and fastest formation time (30 minutes). A magnetic stirrer speed of 1272.73 rpm was used to measure all hydrate phase equilibria data in this study. Mechanical malfunctioning of the agitation system

and stirrer blockage was indicated by the formation of hydrates at unexpectedly low temperatures. At each experimental run, the visual observation of a vortex verified the presence of mixing.
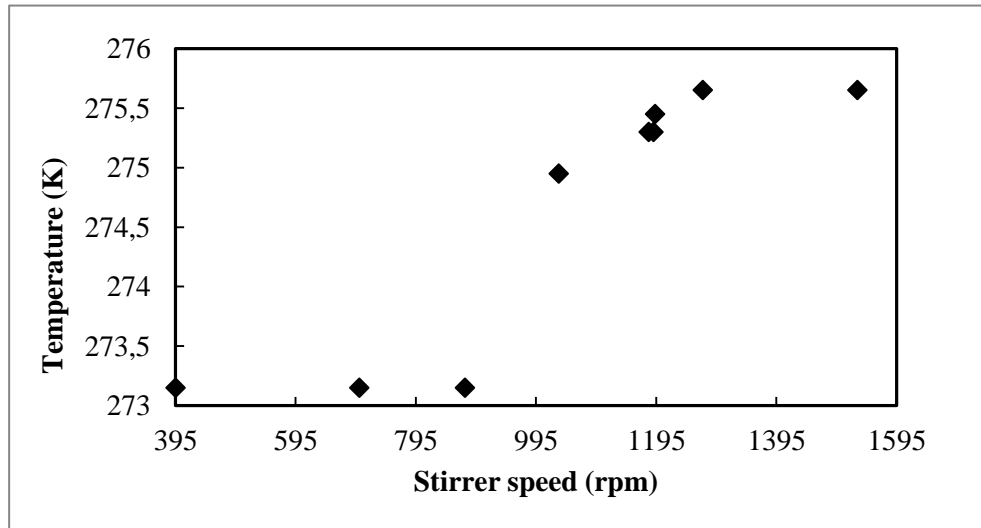
Figure 7-3: Hydrate formation temperature at 1.84 MPa and numerous stirrer speeds. The rate of isochoric cooling remained constant at 97.72 K/h. ◆, hydrate formation; ✖, no hydrate formation.

Once hydrate formation was detected by a noticeable pressure drop and visually confirmed through the sapphire window, the system was heated in two process steps:

1. Rapid heating to the hydrate formation temperature since hydrate dissociation exists at a temperature higher than the formation temperature.
2. Slow heating until the complete decomposition of the hydrate crystal which is noted by either one of the following observations:
   a) The intersection of the dissociation curve with the initial cooling curve.
   b) An insignificant change in pressure with increase in temperature (Refer to Figure 6-10).

Initial heating of the hydrate resulted in a decrease in pressure due to the rate of hydrate formation counteracting the rate of hydrate dissociation. Hydrate dissociation begins when a

sudden increase in pressure results from an increase in temperature, signifying the release of gas from the hydrate crystal. At each heating step, the temperature was held constant for at least 2 hours to eliminate metastability.

7.4 Uncertainties

Double-distilled and deionised water from Direct-Q5 Ultrapure Water Systems (Millipore^{TM}) was used to produce hydrates in all experiments. The ultrapure water was utilized in order to minimize the amount of ions present and diminish any inhibiting effect the ions may have to hydrate formation. The water had an electrical conductivity of 18.3 MΩ at 298.15 K.

As the dissociation (heating) curve approached the initial cooling curve, the rate of heating is decreased to reduce the uncertainty of the graphical method. The heating steps close to the hydrate formation point were repeated to reduce the hysteresis phenomenon.

The verification of experimentally-measured data is imperative to provide some guarantee that the data measured is not a product of chance but a stable and regular observation. The density measurements for all tetrabutyl ammonium salt solutions were performed three times. Vapour pressure data and phase equilibria data were also repeated to verify experimental findings. Since the results are repeatable using the same experimental method, all experimental observations were deemed regular and stable enough to be observed more than once. The calculation of precision errors is presented in Chapter 6.5.

The test systems comprising of $CO_2 + H_2O$, $CO_2 + H_2O$ + TBAC (4 wt%) and $CO_2 + H_2O$ + TBAF (4 wt%) were measured to attempt to validate the accuracy of the experimental apparatus, experimental methodology and analysis. The isochoric pressure-search method was also verified by the visual confirmation of hydrates through the sapphire windows. For proper validation, the equilibrium cell was drained and refilled with the same system to measure additional phase data points. This allowed the corroboration of a well-functioning experimental setup and methodology to measure reliable and accurate new phase data.

Experimental data were measured in an increasing order (of the measured pressure), followed by a decreasing order to reduce the phenomenon of hysteresis. The experimental results section includes:

1. Temperature calibration measurements
2. Pressure calibration measurements
3. Vapour pressure measurements
4. Hydrate dissociation (hydrate equilibrium) measurements

The dissociation steps near the cooling curve were repeated in order to reduce the effects of hysteresis within graphical isochoric-pressure search method.

Table 7.3. summarizes the measurement uncertainties computed in this study. Belandria (2012) measured the $CO_2 + H_2O$ + TBAB systems and calculated the maximum overall uncertainty of ± 50kPa and ± 0.2K. Eslamimanesh (2012) also measured $CO_2 + H_2O$ + TBAB systems and calculated the hydrate phase data uncertainty of ± 50 kPa and ± 0.1 K. The uncertainty in temperature measurements in this study was very close to literature. The pressure uncertainty in this study is much lower than that of literature. The maximum uncertainty in this study is attributed to the accuracy of the pressure transducer. The uncertainty of the hydrate phase equilibrium data (± 0.3 K and ± 1.71 kPa) is represented as errors bars in Chapter 7.5. and has a confidence of 95%.

Table 7.3: Summary of hydrate phase equilibria uncertainties

	T	P
	K	kPa
uncertainty of calibration correlation[a]	±0.05	±0.87
uncertainty of instrument[b]	±0.06	±1.44
uncertainty of repeatability[a]	±0.02	±0.3
uncertainty of procedure[c]	±0.29	-
Total uncertainty of phase data[d]	±0.3	±1.71

[a] Measured

[b] Specified by supplier

[c] The uncertainty of the procedure is the estimated inaccuracy of the graphical isochoric pressure-search method. It was estimated to be the temperature step closest to the cooling curve. ±0.12 K for CO_2 + H_2O system and ±0.29 K for CO_2 + H_2O + TBAC/F systems.

[d] $$u_c = \pm\sqrt{u_{correlation}^2 + u_{instrument}^2 + u_{repeatibility}^2 + u_{procedure}^2}$$

Other uncertainties include the amount of liquid charges into the equilibrium cell. This is assumed to be ±0.5 cm^3. The uncertainty of solution composition is estimated to be ±0.0.0001 g, which is the uncertainty of the mass balance.

7.5 Hydrate Phase Equilibria Measurements

Carbon dioxide (CO_2) is released from industrial plants at atmospheric pressure. This study involves the measurement of CO_2 hydrate phase data at pressures close to atmospheric in order to reduce compression costs during CO_2 capture via gas hydrate crystallization. The hydrate equilibrium pressures were measured below 5MPa. Hydrate phase equilibria data were measured for the systems presented in Table.7.4.

Table 7.4.: Summary of hydrate phase equilibria measured in this study.

System	Pressure Range	Temperature Range	Number of data points
	kPa	K	
$CO_2 + H_2O$	1789 - 4061	276.14 - 282.41	4
$CO_2 + H_2O$ + TBAC (4.21 wt%)	1749 - 2940	283.24 - 284.80	6
$CO_2 + H_2O$ + TBAC (10.05 wt%)	859 - 3584	285.95 – 288.43	5
$CO_2 + H_2O$ + TBAC (30.13 wt%)	1230 - 4520	291.51 – 293.55	5
$CO_2 + H_2O$ + TBAF (4.01 wt%)	680 - 2396	285.80 – 288.31	4
$CO_2 + H_2O$ + TBAF (30.26 wt%)	688 - 1435	301.98 – 304.30	5

7.5.1 Test systems

$CO_2 + H_2O$ system

Table 7.5.: Hydrate phase equilibria data for system $CO_2 + H_2O$. The experimentally-measured phase data in this study have maximum temperature and pressure uncertainties of ±0.14 K and ±1.71 kPa.

This Work		Literature		
T_{exp}	P_{exp}	ΔP^A	ΔP^B	ΔP^C
K	kPa	kPa	kPa	kPa
276.14	1789	20.12	8.87	2.41
278.23	2333	18.41	6.05	3.90
280.21	3063	42.41	29.01	30.86
282.41	4061	52.28	37.75	43.99

$\Delta P = \left| P_{exp} - P_{literature} \right|$

A = Deaton and Frost (1946)

B = Larson (1955)

C = Vlahakis (1972)
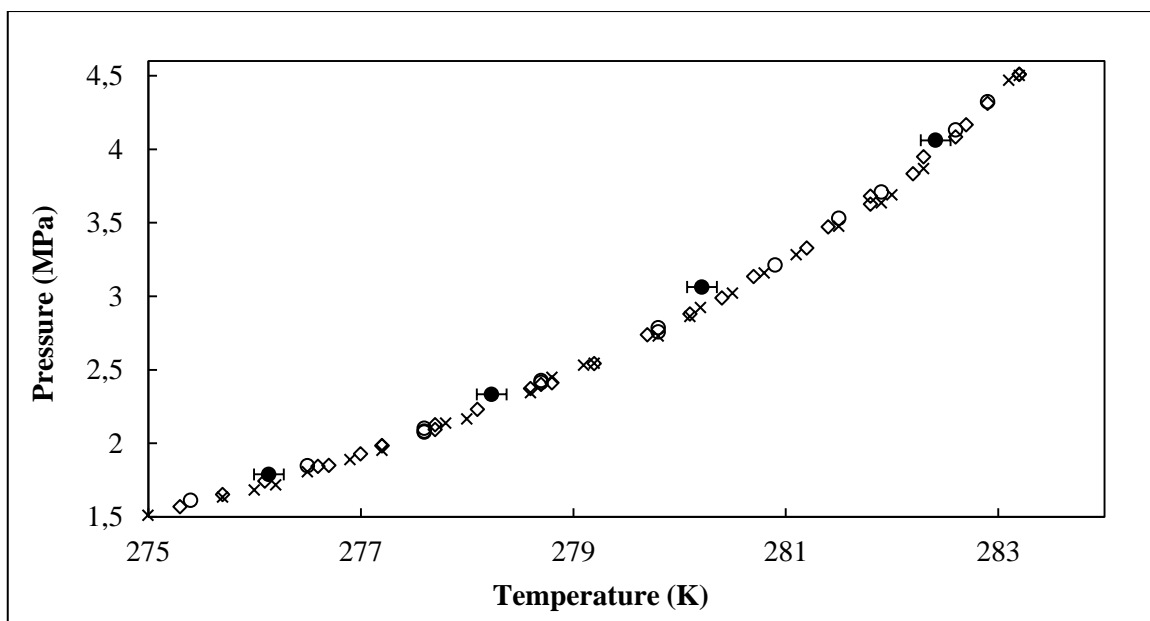
Figure 7-4. Hydrate phase equilibria data for system CO_2+H_2O. The experimentally-measured phase data in this study have a maximum temperature of ±0.14 K and are represented by error bars. ○, Deaton and Frost (1946); ✖ , Larson (1955); ◇, Vlahakis (1972); ●, This study.

The $CO_2 + H_2O$ system was selected due to the ample amount of literature data available. All available literature data were plotted against each other and the literature data with minimum deviation from a common exponential trend fit. This allows for the selection of reliable and accurate literature data. The experimentally-measured phase data were compared to the literature data of Deaton and Frost(1946), Larson(1955) and Vlahakis(1972). The deviation between the experimental phase data and the literature phase data were reported in pressure and shown in Table.7.5.

The deviation from literature is reported in the unit of pressure since the isochoric pressure-search method was used. This method involves the measurement of the hydrate dissociation pressure when the slope of the pressure-temperature diagram changes suddenly (refer to chapter 6.5). Since hydrate dissociation was initiated by the stepwise increase of temperature, the uncertainty of the experimental phase data was illustrated in temperature and represented as an error bar on Figure 7-4. The experimental phase data in Table 7.5 exhibited a good comparison with literature phase data, with a maximum deviation in pressure of 3.14% at 52.28 kPa.

CO_2 + H_2O + TBAC (4 wt%)

Hydrate phase equilibrium data of CO_2 + H_2O + TBAC (tetrabutyl ammonium chloride) and CO_2 + H_2O + TBAF (tetrabutyl ammonium fluoride) were reproduced to validate the use of the isochoric pressure-method in the measurement of systems containing tetrabutyl ammonium salts. Literature on the measurement of hydrate phase equilibrium containing TBAC and TBAF is scarce. Hence the experimental systems were evaluated against one literature data source. The experimental data of systems CO_2 + H_2O + TBAC (4 wt%) and CO_2 + H_2O + TBAF (4 wt%) were compared to literature data of Li et al. (2010). The comparison of Li et al. (2010) against this study is presented in Table 7.6. and Table 7.7 and graphical represented in Figure 7-5 and Figure 7-6.

Table 7.6.: Hydrate phase equilibria data for system CO_2 + H_2O + TBAC (4 wt%). The experimentally-measured phase data in this study have maximum temperature and pressure uncertainties of ±0.30 K and ±1.71 kPa.

| This Work		Li et al. (2010)
T_{exp}	P_{exp}	ΔP
K	kPa	kPa
283.24	1749	30.04
284.10	2293	10.14
281.91	983	1.15
281.25	795	24.34
283.47	1816	17.36
284.80	2940	2.59

$\Delta P = \left| P_{exp} - P_{literature} \right|$

Figure 7-5: Hydrate phase equilibria data for system CO_2 + H_2O + TBAC (4 wt%). The experimentally-measured phase data in this study have a maximum temperature of ±0.29 K and are represented by error bars.△, Li et al. (2010);●, This study (sample 1);□, This study (sample 2).

Hydrate phase equilibrium data was measured for CO_2 + H_2O + TBAC (4 wt%). To appropriately validate the experimental procedure, the phase data was measured using two individual samples of TBAC solution. Four phase data points were measured using the first sample of TBAC solution. The equilibrium cell was drained afterwards and refilled with the second sample of TBAC solution for the measurement of two additional phase data points (Refer to Figure 7-5.). The hydrate equilibrium data from TBAC sample 2 was positioned adequately within the data trend of TBAC sample 2 as shown in Figure 7-5.

CO$_2$ + H$_2$O + TBAF (4 wt%)

Table 7.7: Hydrate phase equilibria data for system CO$_2$ + H$_2$O + TBAF (4 wt%). The experimentally-measured phase data in this study have maximum temperature and pressure uncertainties of ±0.30 K and ±1.71 kPa.

This Work		Li et al. (2010)
T$_{exp}$	P$_{exp}$	ΔP
K	kPa	kPa
285.8	0.68	45
286.71	1.145	23
287.5	1.8	65
288.31	2.396	61

$$\Delta P = \left| P_{exp} - P_{literature} \right|$$

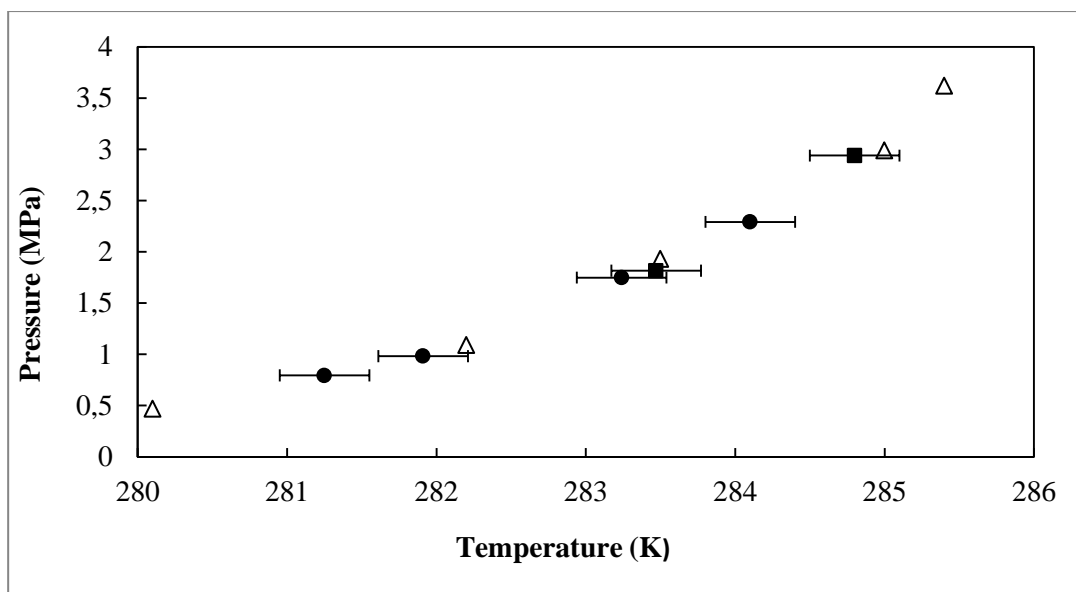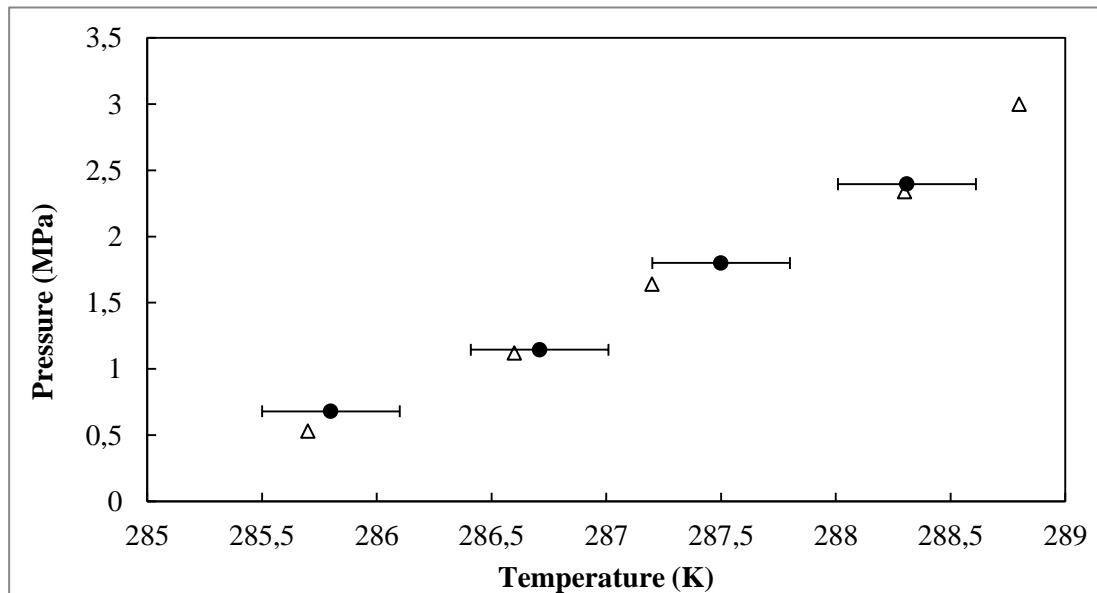**Figure 7-6: Hydrate phase equilibria data for system CO$_2$ + H$_2$O + TBAF (4 wt%). The experimentally-measured phase data in this study have a maximum temperature of ±0.29K and are represented by error bars. △, Li et al. (2010); ●, This study.**

The assessment of the hydrate equilibrium phase data of this study against Li et al. (2010) for the systems $CO_2 + H_2O + TBAC$ (4 wt%) and $CO_2 + H_2O + TBAF$(4 wt%) reveals a maximum deviation of 30.04kPa and 65kPa respectively. Such deviations could be attributed to the distinct scatter in the data of Li et al. (2010). The hydrate equilibrium phase data of Li et al. (2010) was plotted on a log graph and a linear trend line was fitted. A comparison of measured data of Li et al. (2010) and the log trend portrayed a maximum deviation of 52.73 kPa and 179 kPa for $CO_2 + H_2O + TBAC$ (4 wt%) and $CO_2 + H_2O + TBAF$(4 wt%) respectively. Hence the deviation of the experimental data against literature data was well within the deviation of the literature data against its own trend. Figure 7-7 displays the hydrate phase equilibrium data measured by Li et al. (2010) on a log scale.
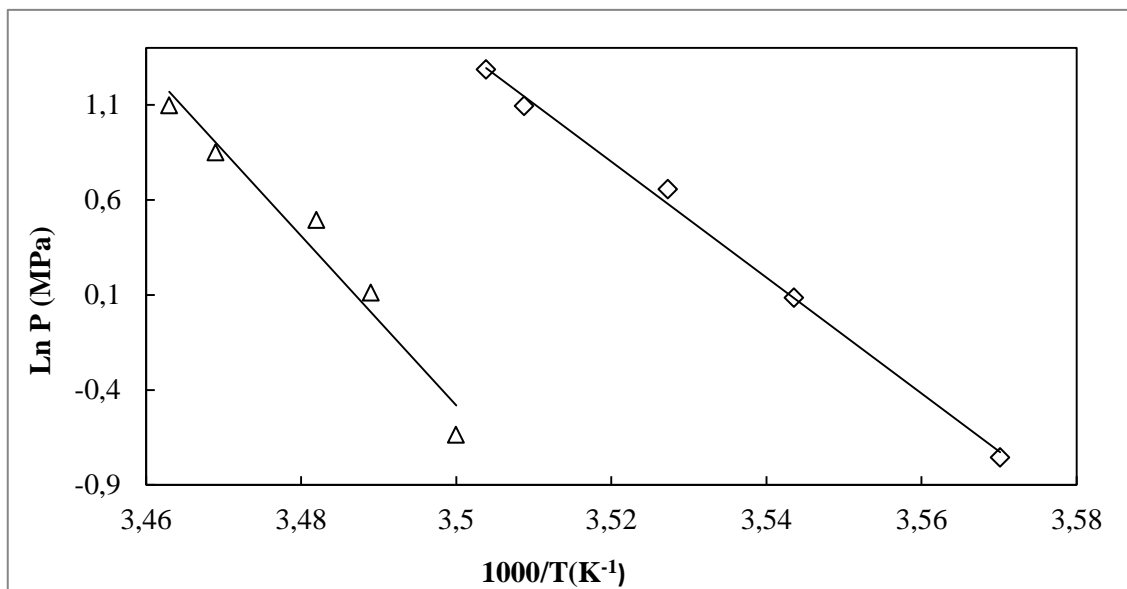
Figure 7-7: Hydrate phase equilibrium data measured by Li et al. (2010). △, $CO_2 + H_2O$ + TBAF (4 wt%); ◇, $CO_2 + H_2O + TBAC$ (4 wt%). The maximum deviation of the phase data from its own trend is 52.73kPa and 179kPa for $CO_2 + H_2O + TBAC$ (4 wt%) and $CO_2 + H_2O + TBAF$ (4 wt%) respectively.

Despite the significant scatter in the hydrate equilibrium data measured by Li et al. (2010), Figure 7-5. and Figure 7-6. illustrate that the data of Li et al. (2010) was positioned acceptably within the region of the error bars of this study.

Deviations between the phase data of this study and Li et al. (2010) could possibly be due to the following:

1. Scatter in the phase data of Li et al. (2010) resulted in an inaccurate trend.
2. Difference in the gas purity
3. Difference in conductivity of H_2O. Li et al. (2010) reported the use of distilled water. Ultrapure water with an electrical conductivity of 18.3 Ω at 298.15 K was used in this study.
4. Li et al. (2010) did not report or consider the reduction of the hysteresis phenomenon during hydrate dissociation.
5. During hydrate dissociation the reduction in the heating rate when approaching the cooling curve is imperative in order to decrease the error of the graphical method. This was not reported or accounted for by Li et al. (2010)

The experimental phase data of CO_2+H_2O compared well to literature. For systems $CO_2 + H_2O+$ TBAC (4 wt%) and $CO_2 + H_2O$ + TBAF (4 wt%), the literature phase data were positioned reasonably within the error bars of the experimental phase data. Hence the modus operandi was validated and future hydrate phase equilibrium data measured would not be a product of apparatus and methodology.

7.5.2 New systems investigated

Hydrate equilibrium for the CO_2 + H_2O system exists at notably high pressures and low temperatures (Refer to Figure 7-4). In order to investigate CO_2 capture via gas hydrate crystallization, a competent promoter needs to be selected to reduce the hydrate equilibrium pressures. Since industrial flue gas is emitted close to atmospheric pressure, the reduction of hydrate equilibrium pressures is necessary for the reduction of compression expenses.

Since flue gas consists of predominately N_2 and CO_2, hydrate equilibrium conditions of $CO_2 +$ H_2O + promoter and N_2 + H_2O + promoter are individually required. Based on the hydrate equilibrium phase equilibrium curve of $CO_2 + H_2O$ compared to $N_2 + H_2O$, the separation of CO_2 can be substantiated. Figure 2-6 demonstrates the difference in hydrate equilibrium curves

between CO_2 + H_2O and N_2 + H_2O, however the effect of a tetrabutyl ammonium salt (promoter) may alter such a curve. Hydrate equilibrium conditions of CO_2 + H_2O + TBAC and CO_2 + H_2O + TBAF were measured in this study. The hydrate equilibrium conditions were measured at different concentrations of the tetrabutyl ammonium salt ranging from 4 wt% to 30 wt%. The promoter concentration range was chosen to estimate optimum parameters that are applicable to a substantial range of promoter concentrations for the Eslamimanesh (2012) predictive model. Hydrate equilibrium conditions were also measured at different promoter concentrations to appropriately analyse the effects of the promoter (tetrabutyl ammonium salt) on hydrate formation. Such effects include the H-V-L equilibrium temperature and the rate of hydrate formation, at various tetrabutyl ammonium salt concentrations.

The hydrate phase equilibrium measurements were undertaken in a pressure range of 0.7 MPa to 5 MPa for the intention of nominal compression costs during CO_2 capture. The measurement of hydrate equilibrium data above 5 MPa resulted in a pressure-temperature curve which resembled the CO_2 vapour pressure curve. The consequent hydrate dissociation process resulted in the intersection of the heating curve and cooling curve at the dew point of CO_2 and not at hydrate equilibrium. Hence hydrate equilibrium measurements in this study were maintained below 5 MPa. The system was cooled to a temperature and pressure that allowed for the formation of CO_2 + TBAC hydrates and CO_2 + TBAF hydrates but not too low as to produce pure TBAC or TBAF hydrates. This prevented the measurement of hydrate equilibrium data near atmospheric pressure.

The CO_2 + H_2O + TBAC system

Hydrate phase equilibrium data for CO_2 + H_2O + TBAC were measured. The mass concentrations of TBAC used were for 4.21 wt%, 10.05 wt% and 30.13 wt%. The experimental data were summarized in Table 7-8 and graphically presented in Figure 7-8. Figure 7-8 clearly illustrates the drastic promoting effects of TBAC. An increase in TBAC concentration resulted in an improved promoting effect of the equilibrium pressure. With reference to a pure CO_2 hydrate, average temperature shifts of approximately 5.67 K, 9.33 K and 14.67 K were noted for 4.21 wt%, 10.05 wt% and 30.13 wt% concentrations of TBAC respectively.

Table 7.8: Hydrate phase equilibria data for system CO_2 + H_2O + TBAC. The experimentally-measured phase data in this study have maximum temperature and pressure uncertainties of ±0.30 K and ±1.71 kPa.

T_{exp}	P_{exp}	TBAC
K	kPa	wt%
281.25	795	
281.91	983	
283.24	1749	4.21
283.47	1816	
284.10	2293	
284.80	2940	
285.95	859	
286.70	1277	
287.35	1877	10.05
287.96	2680	
288.43	3584	
291.51	1230	
292.22	1894	
292.83	2903	30.13
293.07	3290	
293.55	4520	
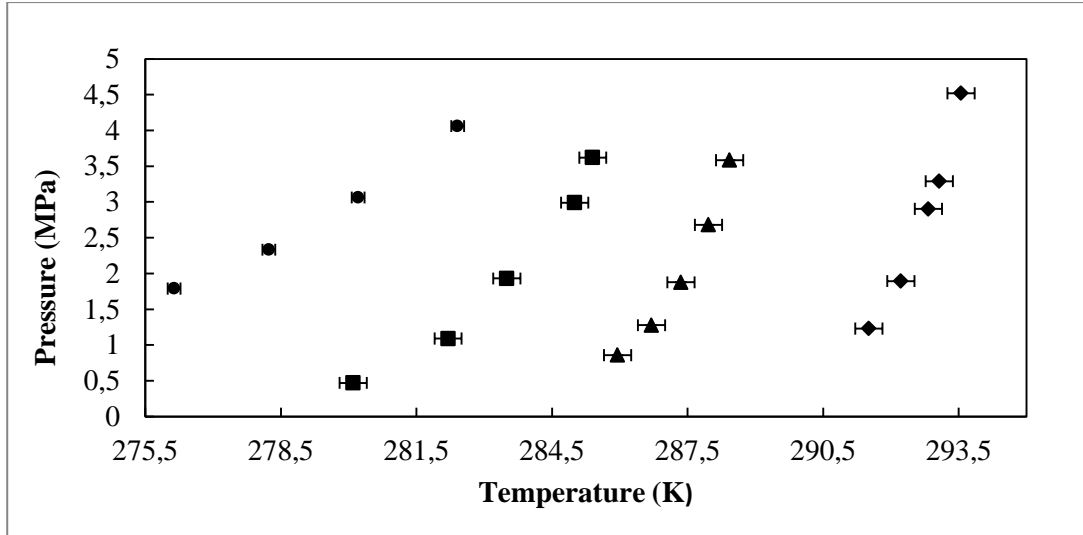
Figure 7-8: Experimental hydrate phase equilibria data for system CO_2 + H_2O + TBAC. ●, 0 wt% TBAC; ■, 4.21 wt%; ▲, 10.05 wt%; ◆, 30.13 wt%.

The CO_2 + H_2O + TBAF system

Hydrate phase equilibrium data were measured for the system CO_2 + H_2O + TBAF. The mass concentrations of TBAF investigated were at 4.01 wt% and 30.26 wt%. The measured equilibrium phase data are summarized in Table 7.9 and compared to the equilibrium phase data of pure CO_2 hydrates summarized in Table 7.5. Figure 7-9 presents a graphical representation of the comparison. Hydrate equilibrium phase data were not measured for a mass concentration of 10 wt% TBAF due to time constraints. Hydrate equilibrium phase data measured by Li et al. (2010) at 8.27 wt% were compared to measured experimental data of this study (Refer to Figure 7-10). An average temperature increase of 11 K, 16 K and 28.5 K was observed at 4.01 wt%, 8.27 wt% and 30.26 wt% mass concentrations of TBAF respectively.

Table 7.9: Hydrate phase equilibria data for system CO_2 + H_2O + TBAF. The experimentally-measured phase data in this study have maximum temperature and pressure uncertainties of ±0.30 K and ±1.71 kPa.

T_{exp}	P_{exp}	TBAF
K	kPa	wt%
285.8	680	
286.71	1145	4.01
287.5	1800	
288.31	2396	
301.98	688	
302.847	922	30.26
306	2439	
305.2	1984	
304.3	1435	
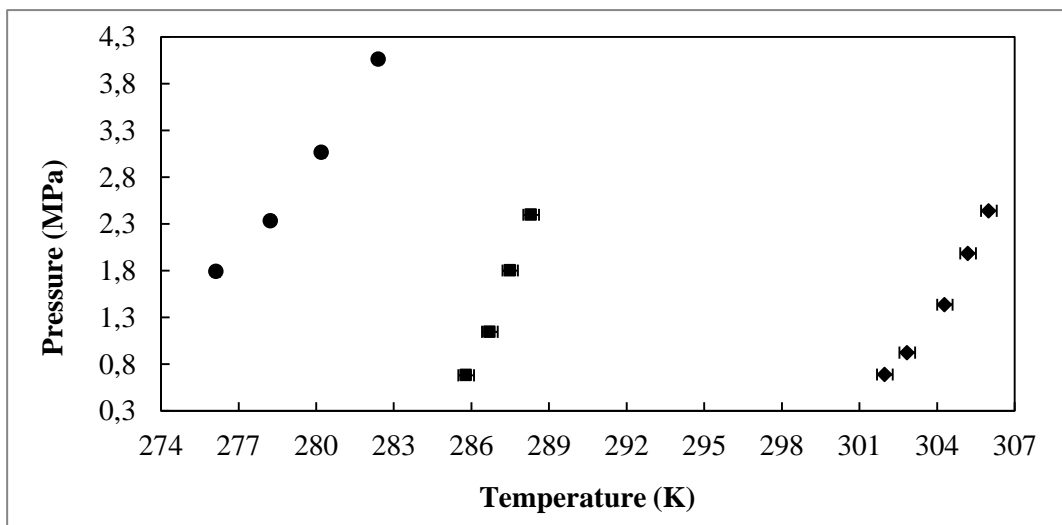
Figure 7-9: Experimental hydrate phase equilibria data for system CO_2 + H_2O + TBAF. ●, 0 wt% TBAF; ■, 4.01 wt%; ◆, 30.26 wt%.
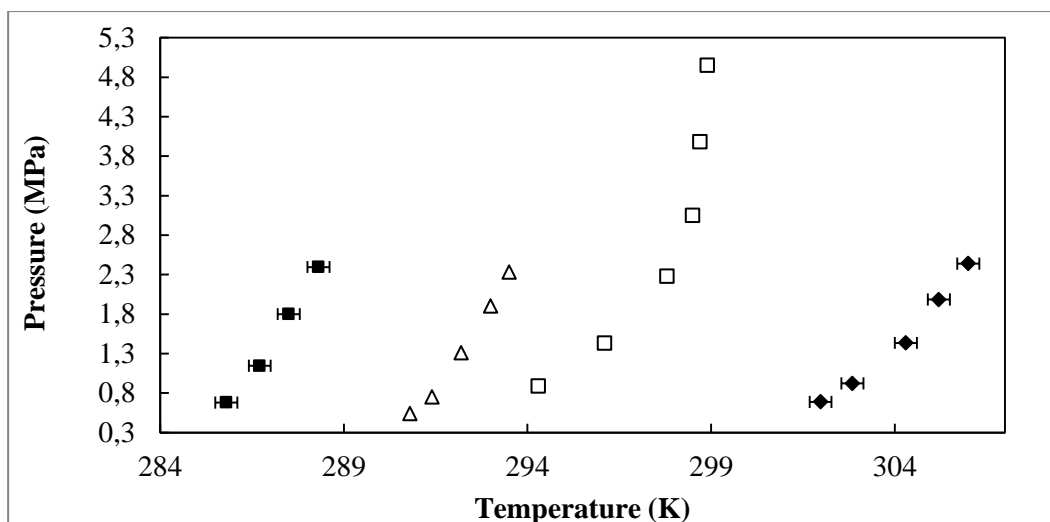
Figure 7-10: Experimental hydrate phase equilibria data for system CO_2 + H_2O + TBAF. ■, This study, 4.01 wt% TBAF; ◆, This study, 30.26 wt% TBAF; △, Li et al. (2010), 8.27 wt% TBAF; □, Mohammadi et al. (2013), 15 wt% TBAF.

The hydrate phase equilibrium data measured for both the CO_2 + H_2O + TBAC and CO_2 + H_2O + TBAF systems demonstrated a highly linear relationship when plotted on a semi–log scale. The deviations of measured data from a linear trend are displayed in Table 7.10 and Table 7.11. For all systems measured, the maximum deviation from a linear trend occurs at the lower pressure region. This is possibly due to a change in semi-clathrate structure. Three crystal structures of TBAC semi-clathrates have been reported: TBAC.24H_2O, TBAC.30H_2O and TBAC.32H_2O (Maniko et al, 2010). TBAF semi-clathrates form two crystal structures: TBAF.28.6H_2O and TBAF.32.2H_2O. Larger deviations occurred at pressures of approximately 1MPa and below. Hence the structural phase transition point of both TBAC and TBAF semi-clathrates may have occurred around this pressure.

Phase equilibrium data for the systems of CO_2 + H_2O + TBAF (>15 wt%) have not been published to date. The phase equilibrium data of the CO_2 + H_2O + TBAF (30.26 wt%) system, measured in this study, was compared to data of lower TBAF concentrations. Figure 7-10 summarizes the phase equilibrium data of CO_2 + H_2O + TBAF (8.27 wt%) and CO_2 + H_2O + TBAF (15 wt%) by Li et al. (2010) and Mohammadi et al. (2013) respectively. The trend of the CO_2 + H_2O + TBAF (30.26 wt%) system is not parallel to the trend of literature data at lower TBAF concentrations (refer to Figure 7-10). The unusual behaviour could possibly be attributed to leakage in the equilibrium cell, an error in the temperature and pressure sensor

recordings, a fast heating rate during the isochoric pressure search method or the high tetrabutyl ammonium salt concentration could have resulted in an inhibited the formation of hydrates. However, the reason currently remains unknown and further experimental study is required to verify the possible sources of error.

Table 7.10: Deviation of the measured CO_2+TBAC hydrate phase equilibrium data from a linear trend.

T_{exp}	P_{exp}	ΔP	TBAC
K	kPa	kPa	wt%
285.95	859	9	
286.7	1277	6	
287.35	1877	15	4.21
287.96	2680	17	
288.43	3584	17	
291.51	1230	8	
292.22	1894	11	
292.83	2903	21	30.13
293.07	3290	24	
293.55	4520	12	

$\Delta P = \left| P_{exp} - P_{literature} \right|$

Table 7.11: Deviation of the measured CO_2 + TBAF hydrate phase equilibrium data from a linear trend.

T_{exp}	P_{exp}	ΔP	TBAF
K	kPa	kPa	wt%
301.98	688	10	
302.85	922	16	
306.00	2439	21	30.26
305.20	1984	40	
304.30	1435	17	

$\Delta P = \left| P_{exp} - P_{literature} \right|$

Figures 7-8 to 7-10 demonstrates the extensive effect of tetrabutyl ammonium salt concentrations on the H-V-L equilibrium line. Four hydrate equilibrium isobars have been calculated from the hydrate equilibrium data of both CO_2 + H_2O + TBAC and CO_2 + H_2O + TBAF. The isobars provide a better representation of the dependency of the hydrate equilibrium temperature on the tetrabutyl ammonium salt concentration. The isobars were calculated by fitting exponential curves to the hydrate equilibrium data (presented in Figure 7-8 and 7-9) at each tetrabutyl ammonium salt concentration. Figure 7-11 and Figure 7-12 provide a graphical representation of the isobars calculated for systems CO_2 + H_2O + TBAC and CO_2 + H_2O + TBAF respectively. From the isobars, it is evident that at a fixed pressure, the temperature at hydrate equilibrium increases significantly when a small amount (~4 wt%) of tetrabutyl ammonium salt is present. The temperature increases steadily until the maximum tetrabutyl ammonium salt concentration (~30 wt%). Further hydrate equilibrium experimental data of tetrabutyl ammonium salt concentrations above 30wt% need to be investigated, to identify the maximum hydrate equilibrium temperature and the maximum salt concentration before the tetrabutyl ammonium salt has an inhibiting effect (decreases the hydrate equilibrium temperature). Excess TBAC and TBAF may form free ions (TBA^+, Cl^- and F^-). The free ions form Coulombic bonds with the dipoles of the water, which inhibit hydrate formation since the water molecules are more attracted to the ions than the hydrate structure (Sabil, 2009).

Figures 7-8 to 7-12 illustrates a trend concerning the tetrabutyl ammonium salt concentration and hydrate equilibrium temperature. As the tetrabutyl ammonium salt concentration increases, the H-V-L equilibrium temperature increases at the same pressure. A comparison of Figure 7-8. and Figure 7-10. demonstrates that the H-V-L equilibrium temperature was higher for CO_2 + H_2O + TBAF than CO_2 + H_2O + TBAC at the same pressure. The H-V-L equilibrium temperature shift (increase in H-V-L temperature) was approximately 1.9 times higher for CO_2 + H_2O + TBAF than CO_2 + H_2O + TBAC at the same pressure.
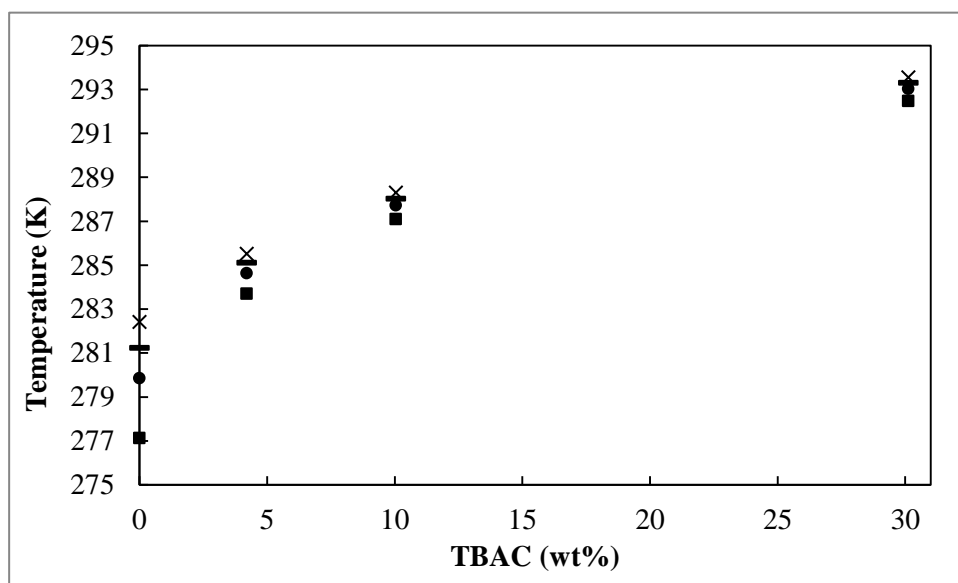
Figure 7-11: Temperature-concentration projection of the H-V-L equilibrium line for system CO_2 + H_2O + TBAC. ✗, 3.5 MPa; ▬, 3 MPa; ●, 2.5 MPa, ■, 1.75 MPa.
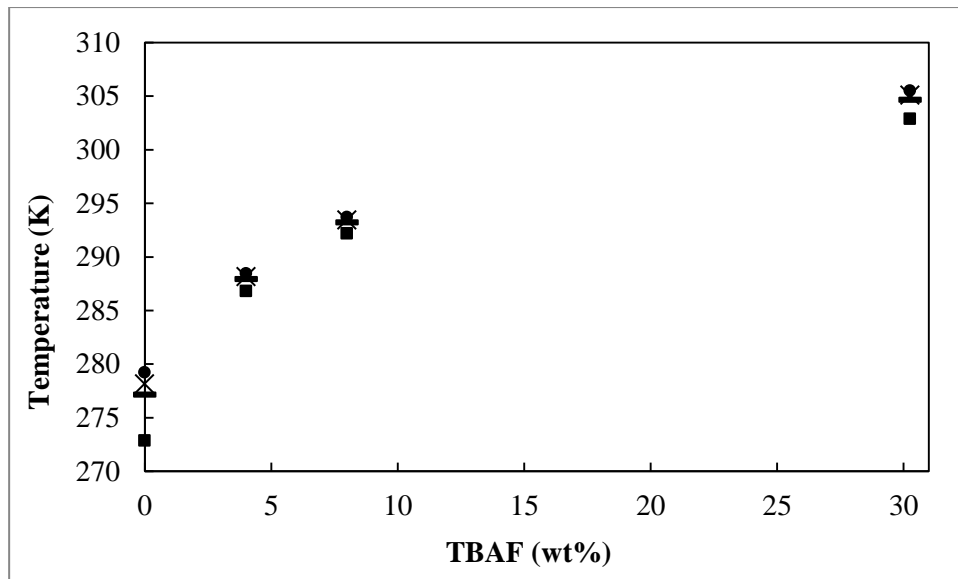
Figure 7-12: Temperature-concentration projection of the H-V-L equilibrium line for the system CO₂ + H₂O + TBAF. ●, 2.3 MPa; ✖, 2 MPa; ▬, 1.75 MPa; ■, 1 MPa.

7.6 Hydrate formation and disassociation rate

Under non-hydrate forming conditions, the solubility of a gas increases with a decrease in temperature. Results of Servio and Englezos (2001) indicate the hydrate formation process alters this pattern. CO_2 solubility in water decreases with decreasing temperature, in the presence of CO_2 hydrates and as the system reaches the hydrate formation region. Complete hydrate formation (beyond metastability) may take a longer duration due to decrease in CO_2 solubility i.e. CO_2 gas is captured at a slow rate. The presence of tetrabutyl ammonium salts further reduces the CO_2 solubility in water and results in a slower hydrate formation rate with increase in tetrabutyl ammonium salt concentration.

7.7   Modelling

Description of models used

The modelling approach used was that of Eslamimanesh (2012). Hydrate literature illustrates that modelling approaches for the prediction of semi-clathrate phase equilibrium data are rare. The model of Eslamimanesh (2012) is the most recent approach for the prediction of semi-clathrate phase equilibrium data and is the simplest approach to predicting semi-clathrate phase equilibrium data of a tetrabutyl ammonium salt. The model of Eslamimanesh (2012) accurately predicted semi-clathrate phase equilibrium conditions of $CO_2 + H_2O$ + TBAB and the promoting effects of TBAB on the H-V-L equilibrium curve (i.e. shifting the H-V-L equilibrium curve to lower pressures and higher temperatures).

The Eslamimanesh (2012) model accounted for the different crystal structures formed by semi-clathrates of tetrabutyl ammonium salts and the altered cavity size present in each new crystal structure (Refer to Table 3.6). Each tetrabutyl ammonium semi-clathrate hydrate structure consists of TBA^+, Cl^-/F^- and water molecules. Secondly, the TBA^+ ions are found within the semi-clathrate structure as guest molecules (in conjunction with CO_2 gas molecules). The TBA^+ are enclosed within large cages (tetrakaidecahedra and pentakaidecahedra cages) and the CO_2 gas are enclosed within small cages (dodecahedral cages) (Eslamimanesh, 2012). The fugacity of the promoter in the liquid phase accounts for the number of TBA^+ occupying cavities (refer to Equation 3.65. The fugacity-based model includes modifications to the Klauder and Slander (2003) model. The modifications introduced Langmuir constants for the tetrakaidecahedra and pentakaidecahedra cages. Eslamimanesh(2012) undertook predictions for the systems of $CO_2 + H_2O$ + TBAF at mass fractions of 0.02-0.35 (TBAF). The predictions illustrated acceptable accuracy to the experimental data with an absolute average relative deviation (AARD%) of 3.1% - 3.2%.

Modelling Methodology

Figure 7-13 illustrates a flow diagram of the modelling approach used to predict hydrate phase equilibrium data for the $CO_2 + H_2O$ + TBAC system. A similar approach was used to predict the hydrate phase equilibrium data of the $CO_2 + H_2O$ + TBAF system.

The fugacity of CO_2 in the vapour phase was calculated using equation (3.5). The fugacity coefficient in solution of component CO_2 in the vapour phase was determined by the Peng and Robinson (1976) equation of state, to offer accurate predictions of VLE for multi-component systems with modest input information required.

The fugacity of TBAC/TBAF in the liquid phase was calculated using equation (3.65). Since thermodynamic data for TBAC and TBAF is limited, the activity coefficient correlation for TBAB was adapted to calculate the activity coefficient correlation for TBAC and TBAF (refer to equation (3.75). Since density correlations for TBAC and TBAF are scarce, the density of TBAC and TBAF was assumed to be equivalent to that to TBAB. . The density (ρ) of the promoter (and consequently the molar volume (V_p^L)) was calculated using the TBAB density correlation recommended by Belandria (2012).

The fugacity of water in the liquid phase was calculated using equation (3.66). The activity coefficient of water in the liquid phase was calculated by means of the Non Random Two Liquid (NRTL) model proposed by Renon and Prausnitz (1968). The NRTL model was used since it is applicable to highly non-ideal models. If electrolytes are present in the aqueous phase, a correction factor is adopted to account for the electrostatic interactions (Englezos, 1992). In this study, weak electrostatic interactions of H_2O-TBAC/F and CO_2-TBAC/F were assumed in order to simplify the modelling correlations.

The fugacity coefficient of water in the hydrate phase was determined using the model of Eslamimanesh (2012), refer to equation (3.61). The model by Parrish and Prausnitz (1972) was used to calculate the Langmuir constants for the dodecahedral cages. However the Langmuir

constants for the tetrakaidecahedra cages and pentakaidechedra cages were calculated using the model of Eslamimanesh (2012).The model accounts for the disorders in the structures of cavities formed by Cl^- and F^- bonds to water molecules and the interactions between large molecules of TBAC/TBAF with each other. TBAC and TBAF form three and two types of crystal structures respectively. Each crystal structure has a specific hydrate number (number of water molecules per molecule of tetrabutyl ammonium salt). The number of hydrate cages per water molecule is dependent on the hydrate number, refer to equation (3.69). Hence the fugacity of water in the hydrate phase is dependent on the hydrate crystal structure formed.

Due to the dependence of the fugacity of water in the hydrate phase to the hydrate structure type, the phase data modelling approach was performed three time for TBAC (for type A, type B and type C) and two times for TBAF (for type A and type B). The deviations of the predicted values to experimental values at each type were evaluated to comprehend which structure formed in the investigated conditions (i.e. pressure-temperature-mass fraction of tetrabutyl ammonium salt).

In order to obtain optimum parameters for equations (3.68), (3.72) and (3.73), the differential evolution (DE) optimization strategy was used. The DE optimization algorithm is considered to be highly efficient in the prediction of thermodynamic model parameters. The most probable optimum parameter was obtained from the minimization of the following objective function (OF), refer to equation (3.81).

Figure 7-13: Flow diagram for the prediction of CO$_2$+H$_2$O+TBAC phase equilibrium data.

Input: T range, Wp, hydrate structure (A,B or C)

Guess: P

Fugacity of CO$_2$ in the vapour phase (Peng-Robinson EOS):
Evaluate: $\hat{\phi}^V_{CO_2}$
Calculate: $\hat{f}^V_{CO_2}$

Fugacity of CO$_2$ in the vapour phase (Peng-Robinson EOS):
Evaluate: γ^p
Calculate: $\hat{f}^L_p$

Fugacity of water in the liquid phase:
Using equation 3.66 and NRTL model calculate: γ_p

Fugacity of water in the hydrate phase:
Evaluate Langmuir constants: C_j^{small}
Using eqution 3.43 calculate: $\hat{f}^\beta_w$

Tol $<1\times10^{-20}$

Calculate optimum parameters:

Figure 7-13: Flow diagram for the prediction of CO$_2$+H$_2$O+TBAC phase equilibrium data.

7.2.1 Modelling Results

The performance of the model for the prediction of CO_2 semi-clathrate phase equilibrium data was examined. The predictive results of the Eslamimanesh (2012) model demonstrated adequate accuracy for the experimental pressure range. The model was used to predict semi-clathrate phase equilibrium data for each crystal structure of TBAC (i.e. type A, type B and type C) and TBAF (i.e. type A and type B). These calculations were undertaken to determine the type of semi-clathrate crystal structure at each experimental condition.

Phase equilibrium data by Li et al. (2010) was used as a test system to verify the prediction accuracy of the Eslamimanesh (2012) model on semi-clathrate hydrates of tetrabutyl ammonium salts. Table 7.12 summarizes the data predicted by Eslamimanesh (2012) for $CO_2 + H_2O$ + TBAC (4.34 wt%) at a pressure range of 470 kPa- 3620 kPa. The prediction data depicts a change in the crystal structure of the TBAC semi-clathrate at 3630 kPa and 285.4 K. The crystal structure at 3630 kPa and 285.4 K is undefined as the model predicted similar phase equilibrium results for type B and type C.

Table 7.13 – 7.16 summarizes the Eslamimanesh (2012) model predictions of semi-clathrate phase equilibrium data for the experimental systems of this study. Semi-clathrate phase equilibrium predictions of $CO_2 + H_2O$ + TBAC (4.21 wt%) suggest crystal type A behaviour for the pressure range (795-2940) kPa. Quantification of the predictions based on Li et al. (2010) i.e. $CO_2 + H_2O$ + TBAC (4.34 wt%) and this study $CO_2 + H_2O$ + TBAC (4.21 wt%) suggest crystal type A behaviour is strongly present for the pressure range of (470-3620) kPa and 4 wt% concentration of TBAC. Large deviations of the predicted type C structure were estimated by the Eslamimanesh (2012) model. This suggests the type C structure of the TBAC semi-clathrate hydrate does not exist at the experimental conditions (temperature, pressure and salt concentration) of this study.

Table 7.12: Hydrate phase equilibria data for test system CO_2 +H_2O + TBAC (4.34 wt%).

Li et al. (2010)		Structure A Predicted	Structure B Predicted	Structure C Predicted
T	**P**	**ΔP**	**ΔP**	**ΔP**
K	**kPa**	**kPa**	**kPa**	**kPa**
280.10	470	10	20	20
282.20	1090	140	140	140
283.50	1930	110	240	240
285	2990	0	0	0
285.40	3620	10	0	0

Table 7.13: Hydrate phase equilibria data for system CO_2 + H_2O + TBAC (4.21 wt%).

This Work		Structure A Predicted	Structure B Predicted	Structure C Predicted
T_{exp}	P_{exp}	**ΔP**	**ΔP**	**ΔP**
K	**kPa**	**kPa**	**kPa**	**kPa**
281.25	795	105	690	690
281.91	983	17	2584	2584
283.24	1749	279	407	407
283.47	1816	36	1780	1780
284.10	2293	133	520	520
284.80	2940	190	3130	3130

Table 7.14: Hydrate phase equilibria data for system CO_2 + H_2O + TBAC (10.0 5wt%).

This Work		Structure A Predicted	Structure B Predicted	Structure C Predicted
T_{exp}	P_{exp}	**ΔP**	**ΔP**	**ΔP**
K	**kPa**	**kPa**	**kPa**	**kPa**
285.95	859	51	51	63
286.70	1277	3	3	163
287.35	1877	153	153	153
287.96	2680	190	190	190
288.43	3584	26	36	36

$\Delta P = \left| P_{exp} - P_{literature} \right|$

Table 7.15: Hydrate phase equilibria data for system CO_2 + H_2O + TBAC (30.13 wt%).

		Structure A	Structure B	Structure C
This Work		Predicted	Predicted	Predicted
T_{exp}	P_{exp}	ΔP	ΔP	ΔP
K	kPa	kPa	kPa	kPa
291.51	1230	280	280	480
292.22	1894	100	304	400
292.83	2903	450	563	563
293.07	3290	300	130	640
293.55	4520	680	230	1090

Table 7.16: Hydrate phase equilibria data for system CO_2 + H_2O + TBAF (4.01 wt%).

		Structure A	Structure B
This Work		Predicted	Predicted
T_{exp}	P_{exp}	ΔP	ΔP
K	kPa	kPa	kPa
285.8	680	130	130
286.71	1145	5	215
287.5	1800	520	380
288.31	2396	626	226

Table 7.17: Hydrate phase equilibria data for system CO_2 + H_2O + TBAF (30.26 wt%).

		Structure A	Structure B
This Work		Predicted	Predicted
T_{exp}	P_{exp}	ΔP	ΔP
K	kPa	kPa	kPa
301.98	688	62	473
302.85	922	542	1748
306	2439	2213	369
305.20	1984	1984	374
304.30	1435	1435	1435

$\Delta P = \left| P_{exp} - P_{literature} \right|$

The TBAF semi-clathrate phase equilibrium data predicted by the Eslamimanesh(2012) model suggested a type A crystal formation at lower pressures and type B crystal formation at higher pressures. The phase equilibrium data (refer to Table 7.16) suggests a structure change from

type A to type B between the pressure and temperature range of (1145-1800) kPa and (286.71-287.5) K respectively.

CHAPTER EIGHT
CONCLUSIONS

Calibrations for the high pressure P10 pressure transducer and the Pt-100 platinum probes were performed. The P10 calibration uncertainty was ±0.87 kPa. The uncertainty of the bottom probe and top probe calibration correlation was estimated to be ±0.03 K and ±0.05 K respectively. The temperature measurements of two probes presented an inconsiderable deviation (0.25 K) in comparison to each other. However to present the most precise temperature data, the bottom probe was used for measurement of temperature at gas hydrate formation since it positioned closest to hydrate crystal. The pressure and temperature sensor calibrations were verified by vapour pressure data measurements of CO_2 and ethane. Due to the acceptable agreement between the experimentally-measured and literature vapour pressure, the pressure and temperature calibrations were reputed viable.

An optimum amount of solution was required to provide significant encapsulation of gas at an optimum time. A significant hydrate formation was noted at 35% (by cell volume) of tetrabutyl ammonium solution.

The use of ionic liquids, i.e. TBAC and TBAF as promoters, resulted in the reduction of CO_2 solubility in water. Lower gas solubility resulted in a slower gas hydrate formation rate due to the deceleration of the kinetic rate. Hence hydrates formed from $CO_2 + H_2O + TBAC$ and $CO_2 + H_2O + TBAF$ had a slower hydrate formation rate than hydrates formed from $CO_2 + H_2O$. This study required the decrease of the system temperature at a lengthy duration in order for hydrate formation to occur.

The measurement of the hydrate equilibrium phase data of this study against Li et al. (2010) for the systems $CO_2 + H_2O + TBAC$ (4 wt%) and $CO_2 + H_2O + TBAF$ (4 wt%) reveals a maximum deviation of 30.04kPa and 65kPa respectively. Such deviations could be attributed to the distinct scatter in the data of Li et al. (2010). The hydrate equilibrium phase data of Li et al. (2010) was plotted on a log graph and a linear trend line was fitted. A comparison of measured data of Li et al. (2010) and the log trend portrayed maximum deviation of 52.73kPa and 179kPa for $CO_2 + H_2O + TBAC$(4 wt%) and $CO_2 + H_2O + TBAF$(4 wt%) respectively. The deviation

of the experimental data against literature data was well within the deviation of the literature data against its own trend.

An increase in TBAC and TBAF concentration resulted in a promoting effect of the equilibrium pressure. With reference to a pure CO_2 hydrate, average temperature shifts of approximately 5.67 K, 9.33 K and 14.67 K were noted for 4.21 wt%, 10.05 wt% and 30.13 wt% concentrations of TBAC. An average temperature increase of 11 K, 16 K and 28.5 K was observed at 4.01wt%, 8.27 wt% and 30.26 wt% mass concentrations of TBAF respectively.

The hydrate phase equilibrium data measured for $CO_2 + H_2O + TBAC$ and $CO_2 + H_2O + TBAF$ demonstrated a highly linear relationship when plotted on a semi–log scale. For all systems measured, the maximum deviation from a linear trend occurs at the lower pressure region. This is possibly due to a change in semi-calthrate structure.

Analysis of the hydrate phase equilibrium data measured for $CO_2 + H_2O + TBAC$ and $CO_2 + H_2O + TBAF$ at a fixed pressure, illustrated a substantial increase the hydrate equilibrium temperature when a small amount (~4 wt%) of tetrabutyl ammonium salt is present. The hydrate equilibrium temperature increases steadily until the maximum tetrabutyl ammonium salt concentration (~30 wt%).

TBAF demonstrated to be a stronger promoter than TBAC. The H-V-L equilibrium temperature was higher for $CO_2 + H_2O + TBAF$ than $CO_2 + H_2O + TBAC$ at the same pressure. The H-V-L equilibrium temperature shift (increase in H-V-L temperature) was approximately 1.9 times higher for $CO_2 + H_2O + TBAF$ than $CO_2 + H_2O + TBAC$ at the same pressure.

The trend of the $CO_2 + H_2O + TBAF$ (30.26 wt%) system was not parallel to the trend of literature data at lower TBAF concentrations. The unusual behaviour could possibly be attributed to various reasons such as a leakage in the equilibrium cell, an error in the temperature and pressure sensor recordings, a fast heating rate during the isochoric pressure search method or the high tetrabutyl ammonium salt concentration inhibited the formation of

hydrates. However, the reason currently remains unknown and further experimental work is required to verify the possible sources of error.

The predicted results of the Eslamimanesh model (2012) demonstrated adequate accuracy at the experimental pressure range. The model was used to predict semi-clathrate phase equilibrium data for each crystal structure of TBAC (i.e. type A, type B and type C) and TBAF (i.e. type A and type B). These calculations were undertaken to comprehend the type of semi-clathrate crystal structure at each experimental condition.

Semi-clathrate phase equilibrium predictions of CO_2 + H_2O + TBAC (4.21 wt%) suggest crystal type A behaviour is strongly present for the pressure range of (470-3620) kPa. Large deviations of the predicted type C structure were estimated by the Eslamimanesh (2012) model. This suggests the type C structure of the TBAC semi-clathrate hydrate does not exist at the experimental conditions (temperature, pressure and salt concentration) of this study. The TBAF semi-clathrate phase equilibrium data predicted by the Eslamimanesh (2012) model suggested a type A crystal formation at lower pressures and type B crystal formation at higher pressures.

CHAPTER NINE
RECOMMENDATIONS

Solubility is a parameter of the hydrate formation rate. The solubility of CO_2 in TBAC and TBAF solutions and solubility measurements in the hydrate formation region is required to broaden the understanding of hydrate formation kinetics and the effects of TBAC and TBAF on the hydrate formation rate.

Further hydrate equilibrium experimental data of tetrabutyl ammonium salt concentrations above 30 wt% need to be investigated; to identify the maximum hydrate equilibrium temperature and the maximum salt concentration before the tetrabutyl ammonium salt has an inhibiting effect (decreases the hydrate equilibrium temperature). Excess TBAC and TBAF may form free ions (TBA^+, Cl^- and F^-). The free ions form Columbic bonds with the dipoles of the water, which inhibit hydrate formation since the water molecules are more attracted to the ions than the hydrate structure. Further hydrate equilibrium experimental data of tetrabutyl ammonium salt concentrations may additionally assist in understanding the change in hydrate crystal structure at different temperatures and pressures.

The phase data trend of the $CO_2 + H_2O +$ TBAF (30.26 wt%) system was not parallel to the trend of literature data at lower TBAF concentrations. Further experimental work is required to verify the possible sources of error or reasoning attributed to the unusual trend of the $CO_2 + H_2O +$ TBAF (30.26 wt%) system.

The determination of the molar composition of the clathrate hydrates in design of the gas hydrate formation processes with the aim of CO_2 capture and sequestration is important. Evaluation of the molar composition information of a CO_2 hydrate facilitates the selection of the optimal operational conditions such as appropriate pressures and temperatures to reach a desired purification of flue gas streams. A mass balance may be applied to determine the molar composition of the hydrate phase.

Hydrate phase equilibrium data of $N_2 + H_2O$ + TBAC at 4.21 wt%, 10.05 wt% and 30.13 wt% and $N_2 + H_2O$ + TBAF at 4.01 wt% and 30.26 wt% may be investigated to substantiate separation of CO_2 in the presence of a tetra-butyl ammonium salt.

.

REFERENCES

Aasberg-Petersen K, Stenby, E, Fredenslund A, 1991, *Prediction of High-pressure Gas Solubilities in Aqueous Mixtures of Electrolytes*. Ind. Eng. Chem. Res.p2180-p2185.

Ambrose D.J, 1986, *Equations for the Correlation and Estimation of Vapour Pressures, J. Chem Thermodyn*. 18, p49.

Ballard L, Sloan E.D, 2004, *TheNext Generation of Hydrate Prediction IV. A Comparison of Available Hydrate Prediction Programs*. Fluid Phase Equilibria 216, p257–p270

Belandria V, Eslamimanesh A, Mohammadi A, Richon D, 2011a, *Gas Hydrate Formation in Carbon Dioxide + Nitrogen + WaterSystem: Compositional Analysis of Equilibrium.* Phases. Ind. Eng. Chem. Res., p4722 – p4730

Belandria V, Eslamimanesh A, Mohammadi A, Richon D, 2011b, *Study of gas Hydrate Formation in Carbon Dioxide + Hydrogen + Water System: Compositional Analysis of Equilibrium.* American Chemical Society, p6455 – p6459

Beltran J.G, Bruusgaard H, Servio P, 2012, *Gas hydrate phase equilibria measurement techniques and phase rule considerations*. J. Chem Thermodynamics 44, p1 – p4.

Benmekki E.H and Mansoori G.A, 1987, *Phase equilibrium calculations of high polar systems*, Fluid Phase Equilibria 32, p139-p149

Beurskens G, Jeffrey G.A, McMullan R.K, 1963, *Polyhedral Clathrate Hydrates .VI.Lattice Type and Ion Distribution in Some New Peralkyl Ammonium, Phosphonium and Sulfonium Salt Hydrates*.Journal of Chemical Physics 39, p3311-3315.

Bishnoi P.R and Natarajan V, 1996, *Formation and decomposition of gas hydrates*, Fluid Phase Equilibria 117, p168-p177

Bridge I, 2011, Eskom gets $806 mln loan for Kusile. Daily News, 30 May

Brown T.D, Taylor C.E, Bernardo M.P, 2010, *Rapid hydrate formation process:W ill they work?*, Energies 3, p1154-p1175

Carol J.J, 2003, *Natural gas hydrates: a guide for engineers*, First Edition, United States of America, Elsevier Science

Changyu S, Wenzhi L, Yang X, 2011, *Progress in hydrate research,* Chinese Journal of Chemical Engineering 19, p151-p162

Chapoy A, Anderson R, Tohidi B, 2007, *Low-Pressure Molecular Hydrogen Storage in Semi-clathrate Hydrates of Quaternary Ammonium Compounds*. Journal of American Chemical Society. Vol 129, p746-p747

Chapoy A, Haghighi H, Burgass R, Tohidi B, 2011, *On the phase behaviour of the (carbon dioxide + water) systems at low temperatures: Experimental and modelling*. J. Chem Thermodynamics, p1 – p6

Cao Z, 2002, *Modelling of Gas Hydrates from First Principles*. Thesis (Phd).Massachusetts Institute of Technology, United States of America.

Chen G.J, Guo T.M, 1996, *Thermodynamic modelling oh hydrates based on new concepts,* Fluid Phase Equilibria, 122, p43-p65

Chen C, Li X, Chen Z, Xia Z, 2014, *Equilibrium hydrate formation conditions of CO_2 + N_2 + SO_2 ternary simulated flue gas in SO_2 and tetra-n-butylammonium bromide containing aqueous solutions,* J. Chem Eng Data, 59, p103-p109

Chirico R.D, Frenkel M, Diky V.V, 2003, *An XML-based approach for storage and exchange of experimental and critically evaluated thermophysical and thermochemical property data*, J. Chem Eng. Data, 48, p1344-p1359

Congressional Research Service, 2010, *Gas Hydrates: Resource and Hazard*

Coquelet, C, 2003, *Etude des Fluides Frigorigènes. Mesureset Modélisations*, Thèse de doctorat, Ecole des Mines de Paris, France.

CSLF, 2008, *Results from G8-IEA Calgary Workshop on Near-Term Opportunities for Carbon Capture and Storage.Carbon Sequestration Leadership Forum*, Calgary: CSLF.

Deaton W.M, Frost E.M, 1946, *Gas Hydrates and Their Relation to the Operation of Natural Gas Pipelines*, U.S Bureau of Mines Monograph 8, p101.

Department of Energy, 2011, *CCS legal and regulatory activity in South Africa*, South Africa: Department of Energy.

Dharmawardhana P.B, Parrish W.R, Sloan E.D, 1980. *Experimental thermodynamic parameters for the prediction of natural gas hydrate dissociation conditions*. Ind. Eng. Chem. Fund.19, p410–p414.

Dorsett L, 1989, *LYX: reapplication of the proven technology*, Dallas SPE Gas Technology Symposium, p239-p246

Duc N.H, Chauvy F, Herri J.M, 2007, *CO_2 capture by hydrate crystallization – A potential solution for gas emission of steelmaking industry*. Energy Conversation and Management 48, p1313-p1322

Englezos P, 1992, *Computation of the Incipient Equilibrium Carbon Dioxide Hydrate Formation Conditions in Aqueous Electrolyte Solutions*, Ind. Eng. Chem. Res., Volume 31, p2232-p2237

Englezos P, 1993, *Clathrate Hydrates.* Ind. Eng. Chem. Res., Volume 32 (No.7), p125-p1274

Eslamimanesh A, Mohammadi A, Richon D, 2011, *Thermodynamic model for predicting phase equilibria of simple clathrate hydrates of refrigerants*. Chemical Engineering Science 66, p5239-p5445

Eslamimanesh A, Mohammadi A, Richon D, Naidoo P, Ramjugernath D, 2011, *Application of gas hydrate formation in separation processes: A review of experimental studies*. J. Chem Thermodynamics 46, p62-p71

Eslamimanesh A, 2012, *Thermodynamic studies on Semi-clathrate Hydrates of TBAB + Gases containing Carbon Dioxide*, Thesis (PhD), MINES ParisTech

Fan S, Li S, Wang J, Lang X, Wang Y, 2009, *Efficient Capture of CO_2 from Simulated Flue Gas by Formation of TBAB or TBAF Semiclathrate Hydrates*. Energy and Fuels, p4202-p4208

Fan S, Li Q, Nie J, Lang X, Wang Y, 2013, *Semiclathrate hydrate phase equilibrium for CO2/CH4 gas mixtures in the presence of tetrabutylammonium halide (Bromide, Chloride or Fluoride)*. J. Chem. Eng Data., 58, p3137-p3141

Feil D, Jeffrey G, 1961, *Polyhedral Clathrate Hydrates II. Structure of Hydrate of Tetra Iso-Amyl Ammonium Fluoride*. J. Chem. Phys 35, p1863-p1873

Ferneyrou G, 1996, *Elucidation of the formation and decomposition of clathrate hydrates of natural gases through gas solubility measurements,* Thesis (MSc), Rice University

Fowler D.L, Loebenstein D.B, Kraus C.A, 1940*, Some Unusual Hydrates of Quaternary Ammonium Salts*. Journal of the American Chemical Society 62, p1140-p1142

Fowler M, 2008, *The Role of Carbon Capture and Storage Technology in Attaining Global Climate Stability Targets: A Literature Review*, Boston: Clean Air Task Force, p1-p21

Gholinezhad J, Chapoy A, Tohidi B, 2011, *Separation and capture of carbon dioxide from CO_2/H_2 syngas mixture using semi-clathrate hydrates*. Chemical Engineering Research and Design 89, p1747-p1751

Hashimoto S, Sugahara T, Moritoki M, 2008, Chemical Engineering Science 63, *Thermodynamic stability of hydrogen + tetra-n-butyl ammonium bromide mixed gas hydrate in non-stiochiometric aqueous solutions*, Chemical Engineering Science 63, p1092-p1097

He T, Susanne E.J, Zitha P.L.J, Golombok M, 2011, *Kinetics of CO_2 and methane hydrate formation: An experimental analysis in the bulk phase*, Fuel 90, p272-p279

Herri J.M, Bouchemoua A, Kwaterski M, 2011, *Gas hydrate equilibria for CO_2-N_2 and CO_2-CH_4 mixtures – Experimental studies and thermodynamic modelling*, Fluid Phase Equilibria, p171-p190

Heuvel M.M, 2004, *Phase behaviour and structural aspects of ternary clathrate hydrate systems and the role of additives*, Thesis (PhD), Technische Universiteit Delft

Holder G.D, Corbin. G, Papadopoulos K.D, 1980, *Thermodynamic and molecular properties of gas hydrates from mixtures containing methane, argon and krypton*. Ind. Eng. Chem. Fundam.19, p282-p286.

Hughes T.J, Marsh K.N, 2011, *Methane Semi-Clathrate Hydrate Phase Equilbria with Tetraisopentylammonium Fluoride.* J. Chem Data 56, p4597-p4603

IEA, 2010, *Carbon Dioxide Capture and Storage Model Regulatory Framework*, France: IEA.

IPCC, 2005, *Carbon dioxide capture and storage, IPCC Special report on Carbon Dioxide Capture and Storage*, Washington DC: ECN

Javanmardi J and Moshfeghian M, 2003, *Energy consumption and economic evaluation of water desalination by hydrate phenomenon*, Applied Thermal Engineering 23, p845-p847

Kamath, V. A, 1984, Study *of Heat Transfer Characteristics during Dissociation of Gas Hydrates in Porous Media,* Ph.D. Dissertation, University of Pittsburgh, United States of America.

Kashciev D and Firoozabadi A, 2002, *Driving force of crystallization of hydrates*, Journal of Crystal Growth, p220-p230

Klauda J.B, Sandler S.I, 2003, *Phase behaviour of clathrate hydrates: a model for single and multiple gas component hydrates*. Chemical Engineering Science 58, p27-p41

Klauda J.B, Sandler S.I, 2000, *A Fugacity Model for Gas Hydrate Phase Equilibria*. Ind. Eng. Res. 39, p3377-p3386

Krichevsky T.R, Kasarnovsky J.S, 1935*, Thermodynamical calculations of solubilities of nitrogen and hydrogen in water at high pressures*, Journal of American Chemical Society 57, p2168-p2172

Lang X, Fan S, Wang Y, 2010, *Intensification of methane and hydrogen storage in clathrate hydrate and future prospect,* Journal of Natural Gas Chemistry, 19, p203-p209

Larson S.D, 1955, *Phase Studies of the Two-Component Carbon Dioxide Water System, Involving the Carbon Dioxide Hydrate*, University of Illinois, Urbana, IL

Lee J, Lee J.D, Linga P, Englezos P, Kim Y.S, Lee M.S, Kim Y.D, 2010a, *Gas Hydrate Formation Process For Pre-Combustion Capture of Carbon Dioxide,* Energy 35, p2729 - p2733

Lee S, Lee Y, Sungmin P, Seo Y, 2010b, *Phase equilibria of semi-clathrate hydrate for nitrogen in the presence of tetra-n-butyl ammonium bromide and fluoride,* J.Chem Eng Data, 55, p5883-p5886

Li S, Fan S, Wang J, Lang X, Liang D, 2009, CO_2 *from binary mixture via forming hydrate with the help of tetra-n-butyl ammonium bromide*. Journal of Natural Gas Chemistry, p15-p20

Li S, Fan S, Wang J, Lang X, Wang Y, 2010, *Semiclathrate Hydrate Phase Equilibria for CO_2 in the Presence of Tetra-n-butyl Ammonium Halide (Bromide, Chloride, or Fluoride)*.J. Chem. Eng. Data.p3212– p3215

Lieberg J, 2011, *Carbon Capture and Storage, The challenges of working towards sustainable solutions,* South Africa: Sasol, p1-p12

Lin W, Delahaye A, Fournaison L, 2008, *Phase equilibrium and dissociation enthalpy for semi-clathrate hydrate of CO2+TBAB.* Fluid Phase Equilibria 264, p220-p227

Lin W, Dalmazzone D, Furst W, 2013, *Thermodynamic studies of CO_2+TBAB+Water system: experimental measurements and correlations.*, J. Chem. Eng. Data, 58, p2233-p2239

Linga P, Kumar R, Englezos P, 2007, *Theclathrate hydrate process for post and pre-combustion capture of carbon dioxide*.Journal of Hazardous Materials, p625-p629

Linga P, Kumar R, Ripmeester J.A, Englezos .P, 2008, *Hydrate Processes for CO₂ Capture and Scale Up using a New Apparatus.*Proceedings of the 6th International Conference on Gas Hydrates, p1- p4

Linga P, 2009, *Separation of Carbon Dioxide from Flue Gas (Post-Combustion Capture) via Gas Hydrate Crystallization*, Thesis (MSc). University British Columbia, Vancouver*.*

Liu N, Gong G, Liu D, Xie Y, 2008, *Effects of Additives on Carbon Dioxide Hydrate Formation.* Proceedings of the 6th International Conference on Gas Hydrates, July 6-10 2008 Vancouver. China: College of Power Engineering.

Ma Q.L, Chen G.J, Guo T.M, 2003, *Modelling of the gas hydrate formation of inhibitor containg systems*, Fluid Phase Equilibria, 205, p291-p302

Maekawa T, 2011, *Equilibrium conditions of clathrate hydrates formed from carbon dioxide and aqueous acetone solutions.* Fluid Phase Equlibria 303, p76-79

Maniko T, Yamamoto T, Nagata K, Sakamoto H, Hashimoto S, Sugahara T, Ohgaki K, 2010, *Thermodynamic stabilities of tetra-n-butyl ammonium chloride + H₂, N₂, CH₄, CO₂ or C₂H₆ semi-clathrate systems*, J. Chem. Eng. Data 55, p839-p841

Meysel P, Oellrich L, Bishnoi P.R, Clarke M.A, 2011, *Experimental investigation of incipient equilibrium conditions for the formation of semi-clathrate hydrates from quaternary mixtures of (CO2 + N2 + TBAB + H2O).* J Chem Thermodynamics 43, p1475-p1479

Mo Y.G, Lee Y.C, Cho B.H, Baek Y.S, 2004, *An analysis of influence on chemical additives in gas hydrate formation.*Journal of Korean Institute of Gas.Volume 8, p23- p24.

Mohammadi A, Mehrdad M, Richon D, Mohammadi A, 2013, *Phase equilibrium measurements for semi-clathrate hydrates of the(CO2 + N2 + tetra-n-butylammonium bromide) aqueous solution system*. J. Chem. Eng. Data 58, p3545-p3550.

Mohammadi A, Eslamimanesh, Belandria V, Richon D, Naidoo P, Ramjugernath D, 2012, *Dissociation data od semi-clathrate hydrates for the systems of tetra-n-butylammonium fluoride (TBAF) + methane + water, TBAF + carbon dioxide + Water and TBAF + nitrogen + water, J. Chem. Thermodynamics*, p57-p61.

Mork M, 2002, *Formation Rate of Natural Gas Hydrate. Reactor Experiments and Models*.Thesis (MSc).Norwegian University of Science and Technology, Norway.

Munck, J, Jorgensen, S.S, Raamussen P, 1988,*Computations of the Formation of Gas Hydrates*. Chem. Eng. Sci. 43 (10), p2661-p2672.

Mühlbauer, A L, (1990), *Measurement and Thermodynamic Interpretation of High-Pressure Vapour-Liquid Equilibrium Data*, PhD thesis, University of Natal, Durban, South Africa

Oellrich L.R, 2004, *Natural Gas Hydrates and their Potential for Future Energy Supply*.XVII National and VI ISHMT/ASME Heat and Mass Transfer Conference, 5-7 January, IGCAR, Kalpakkam, p70 – p78

Ostergaard K.K, Tohidi B, Burgass R.W, 2000, *Improving the accuracy of gas hydrate dissociation point measurements*, Annual N.Y Acad. Sci., 912, p924-p931

Paricaud P, 2011, *Modelling the dissociation conditions of salt hydrates and gas semi-clathrate hydrates: Application to lithium bromide, hydrogen iodide and tetra-n-butyl ammonium bromide + carbon dioxide systems*, J. Phys. Chem B, p288-p299

Parrish W.R, Prausnitz J.M, 1972, *Dissociation Pressures of Gas Hydrates Formed by Gas Mixtures*. Ind. Eng. Chem. Process Des. Develop, Vol 11, No.1, p26-35.

Peng, D Y and Robinson, D B, 1976, *A New Two Constant Equation of State*, Industrial and Engineering Chemistry Fundamentals, Vol. 15, pp. 59-64.

Petticrew C, 2011, *An investigation into the use of fluorinated hydrating agents in the desalination of industrial water,* Thesis (MSc). University of KwaZulu-Natal, South Africa.

Prausnitz, J. M and Chueh, P. L, 1968, *Computer Calculations for High-Pressure Vapour-Liquid Equilibria,* Prentice-Hall, Englewood Cliffs, N. J.

Raal, J D and Mühlbauer, A L, 1994, The *Measurement of High Pressure Vapour-Liquid Equilibria*. Dev. Chem. Eng. Mineral Process, Vol. 2, p69- p105.

Raal, J D and Mühlbauer, A L, 1998, *Phase Equilibria: Measurement and Computation*, Washington: Taylor &Francis

Renon, H and Prausnitz, J M, 1968, *Local Compositions in Thermodynamic Excess Functions for Liquid Mixtures*, American Institute of Chemical Engineers Journal, Vol. 14, p135-p144.

Sabil K.B.M, 2009, Phase Behaviour, Thermodynamics and Kinetics of Clathrate Hydrate Systems of Carbon Dioxide in Presence of Tetrahydrofuran and Electrolytes.Thesis (MSc). University of Science,Malaysia

SANERI, 2010, *SANERI Annual Report*, South Africa: SANERI.

Schroeter J.P, Kobayashi R, Hildebrand M.A, 1983, *Hydrate decomposition conditions in the system hydrogen sulphide-methane-propane*, Industrial and Engineering Chemistry Fundamentals, Vol. 22, p362-p364.

Servio P and Englezos P, 2001, *Effect of temperature and pressure on the solubility of carbon dioxide in water in the presence of gas hydrate*, Fluid Phase Equilibria, 190, p127-p134

Sfaxi I.B.A, Belandria V, Mohammadi A.H, 2012, *Phase Equilibria of CO_2+N_2 and CO_2+CH_4 clathrate hydrates: experimental measurements and thermodynamic modelling*, Chemical Engineering Science 84, p602-p611

Shimada W, Shiro M, Kondo H, 2005, *Tetra-n-butylammonium bromide water*, Acta Crystallogr. 64, p65-p66Shin W, Park S, Ro H, 2012, *Phase equilibrium measurements and the tuning behavior of new sII clathrate hydrates*, J. Chem. Thermodynamics 44, p20–p25

Sloan E.D and Koh C.A, 2008, *Clathrate Hydrates of Natural Gases*, Third Edition, United States of America, CRC Press

Sloan E.D, 2003, *Fundamental principles and applications of natural gas hydrates*. Nature, Volume 426, 353-359

Smith J.M, Van Ness H.C and Abbott M.M, 2005, *Introduction to Chemical Engineering Thermodynamic*, McGraw Hill, 7th Ed.

Soave, G, 1972, *Equilibrium Constants from a Modified Redlich-Kwong Equation of State*, Chemical Engineering Science, Vol. 27, pp. 1197-1203.

Stryjek R and Vera J, 1986, *PRSV:An Improved Peng-Robinson Equation of State for Pure Compiunds and Mixtures*, Can. J. Chem. Eng 64, p323-p333.

Sun Z.G, Liu C.G, Zhou B, Xu L.Z, 2011, *Phase Equilibrium and Latent Heat of Tetra-n butyl ammonium Chloride Semi-Clathrate Hydrate*, J.Chem. Eng. Data, 56, p3416-p3418

Taylor C.E, Kuyatt J.T, 2004, *Advances in the study of gas hydrates*, Kluwer Academic/Plenum Publishers: New York

Tohidi B, Tong J, Chapoy A, Anderson R, Armandi M, 2006, *A method for Gas Storage, Transport and Energy generation*. WO2006/131738 A2.

Tshibangu M, 2010, *High Pressure Vapour-Liquid Equilibrium Data of Fluorochemical Systems for Various Temperatures Using a New Static Apparatus*.Thesis (MSc). University of KwaZulu-Natal, South Africa.

Vlahakis J.G, Chen H.S, Suwandi M.S, Barduhn A.J, 1972, *The Growth Rate of Ice Crystals: Properties of Carbon dioxide Hydrates, A Review of Properties of 51 Gas Hydrates*, Syracuse U. Research and Development Report 830, prepared for US Department of the Interior.

van der Waals, J. H, Platteeuw, J. C, 1959, *Clathrate Solutions*. Adv. Chem. Phys.(2).p1-p57.

Walas, S.M, 1985, *Phase Equilibrium in Engineering*, Butterworth, Boston.

Xie Y, Wei J, Liu D, Shi J, 2010, *Experimental study of a novel cold storage medium-tetrabutyl ammonium chloride hydrate*, 9th IIR Conference on PCMs and Slurries for Refrigeration and Air Conditioning, 29 September – 1 October 2010, Sofia (Bulgaria), IIR Proceedings Series 'Refrigeration Science and Technology', p153-p158

Xu Z and Liang D, 2014, *Equilibrium data of (tert-butylamine+CO$_2$) and (tert-butylamine+N$_2$) clathrate hydrates*, J. Chem. Eng. Data

Yazdizadeh M, Eslamimanesh, Esmaeilzadeh F, 2011, *Thermodynamic modeling of solubilities of various solid compounds in supercritical carbon dioxide: Effects of equations of state and mixing rules*. J. of Supercritical Fluids 55.p861-p875

Zhang C.S, Fan S.S, Liang D.Q, Guo K.H, 2004, *Effect of additives on formation of natural gas hydrate*. Fuel 83, p2115 – p2121

Zhang Y, Debenedetti P.G, Prud'homme R.K, Pethica B.A, 2006, *Accurate prediction of clathrate hydrate phase equilibria below 300K from a simple model*. Journal of Petroleum Science and Engineering 51, p45 – p53